

Highly Efficient MRI Contrast Agents: from Monomers to Nanoparticles

THÈSE N° 4264 (2008)

PRÉSENTÉE LE 18 DÉCEMBRE 2008

À LA FACULTÉ SCIENCES DE BASE

LABORATOIRE DE CHIMIE INORGANIQUE ET BIOINORGANIQUE

PROGRAMME DOCTORAL EN CHIMIE ET GÉNIE CHIMIQUE

ÉCOLE POLYTECHNIQUE FÉDÉRALE DE LAUSANNE

POUR L'OBTENTION DU GRADE DE DOCTEUR ÈS SCIENCES

PAR

Loïck MORIGGI

acceptée sur proposition du jury:

Prof. J.-C. Bünzli, président du jury

Prof. L. Helm, directeur de thèse

Dr E. Jakab Toth, rapporteur

Dr C. Mayer, rapporteur

Prof. K. Severin, rapporteur



ÉCOLE POLYTECHNIQUE
FÉDÉRALE DE LAUSANNE

Suisse
2008

TABLE OF CONTENTS

TABLE OF CONTENTS THESIS	3
ABSTRACT	7
RÉSUMÉ	11
ACKNOWLEDGEMENTS	15
SYMBOLS AND ABBREVIATIONS	17

CHAPTER I.

INTRODUCTION	21
---------------------	-----------

TABLE OF CONTENTS CHAPTER I	23
I.1 MAGNETIC RESONANCE IMAGING : OVERVIEW	25
I.1.1 MAGNETIC RESONANCE IMAGING (MRI)	25
I.1.2 Gd(III)-COMPLEXES AS MRI CONTRAST AGENTS	29
I.1.3 THERMODYNAMIC STABILITIES	30
I.1.4 PARAMAGNETIC RELAXATION ENHANCEMENT (PRE) THEORY	30
I.1.5 NANOPARTICLES	36
I.2 SCOPE OF THE THESIS	37
I.3 REFERENCES	40

CHAPTER II.

PHYSICOCHEMICAL PROPERTIES OF THE HIGH FIELD MRI RELEVANT [GD(DTTA-ME)(H₂O)₂]⁻ - COMPLEX	43
--	-----------

TABLE OF CONTENTS CHAPTER II	45
II.1 INTRODUCTION	47
II.2 EXPERIMENTAL SECTION	49
II.2.1 SYNTHESIS OF H ₄ DTTA-ME	49
II.2.2 PROTONATION AND STABILITY CONSTANTS BY POTENTIOMETRIC MEASUREMENTS	50
II.2.3 DEUTERATION CONSTANTS BY ¹ H-NMR MEASUREMENTS	50

II.2.4	CONDITIONAL RELATIVE STABILITY CONSTANT $K_{L1/L2}^*$ OF $[\text{Gd}(\text{DTTA-ME})(\text{H}_2\text{O})_2]^-$ RELATIVE TO $[\text{Gd}(\text{DTPA-BMA})(\text{H}_2\text{O})]$	51
II.2.5	TRANSMETALATION OF $[\text{Gd}(\text{DTTA-ME})(\text{H}_2\text{O})_2]^-$ WITH Zn^{2+}	51
II.2.6	SEARCH FOR TERNARY ADDUCT FORMATION BETWEEN $[\text{Gd}(\text{DTTA-ME})(\text{H}_2\text{O})_2]^-$ AND L- LACTATE	52
II.3	RESULTS AND DISCUSSION	53
II.3.1	POTENTIOMETRY	53
II.3.2	^1H NMR IN D_2O	58
II.3.3	STABILITY CONSTANTS BY POTENTIOMETRY	61
II.3.4	CONDITIONAL RELATIVE STABILITY CONSTANT $K_{L1/L2}^*$ OF $[\text{Gd}(\text{DTTA-ME})(\text{H}_2\text{O})_2]^-$ RELATIVE TO $[\text{Gd}(\text{DTPA-BMA})(\text{H}_2\text{O})]$	62
II.3.5	TRANSMETALATION OF $[\text{Gd}(\text{DTTA-ME})(\text{H}_2\text{O})_2]^-$ WITH Zn^{2+}	66
II.3.6	SEARCH FOR ADDUCT FORMATION BETWEEN $[\text{Gd}(\text{DTTA-ME})(\text{H}_2\text{O})_2]^-$ AND L-LACTATE	68
II.4	CONCLUSION	71
II.5	ACKNOWLEDGEMENTS	73
II.6	REFERENCES	74

CHAPTER III.

**RUTHENIUM-BASED METALLOSTAR: SYNTHESIS, SENSITIZED
LUMINESCENCE AND ^1H RELAXIVITY**

TABLE OF CONTENTS CHAPTER III	79
III.1 INTRODUCTION	81
III.2 EXPERIMENTAL SECTION	84
III.2.1 SYNTHESIS AND CHARACTERIZATION	84
III.2.2 ^1H NMR SPECTROSCOPY	85
III.2.3 ^1H RELAXIVITY	85
III.2.4 OPTICAL SPECTROSCOPY	85
III.3 RESULTS AND DISCUSSION	87
III.3.1 THE RU(II) BASED METALLOSTAR - A SYNTHETIC CHALLENGE	87
III.3.2 OPTICAL CHARACTERIZATION OF THE TRIS-(2,2'-BIPYRIDYL)RUTHENIUM(II) UNIT	88
III.3.3 SENSITIZED EU LUMINESCENCE	91
III.3.4 ^1H RELAXIVITY OF $\{\text{Ru}[\text{Gd}_2\text{BPY-DTTA}_2(\text{H}_2\text{O})_4]_3\}^{4-}$	94
III.4 CONCLUSION	99

III.5 ACKNOWLEDGEMENTS	100
III.6 REFERENCES	101

CHAPTER IV.

DTTA THIOL DERIVATIVES COATED TO GOLD NANOPARTICLES (DTNP)	103
---	------------

TABLE OF CONTENTS CHAPTER IV	105
IV.1 INTRODUCTION	107
IV.2 EXPERIMENTAL SECTION	111
IV.2.1 SYNTHESIS OF LANTHANIDE FUNCTIONALIZED GOLD NANOPARTICLES (LN-DTNP)	111
IV.2.2 TRANSMISSION ELECTRON MICROSCOPY (TEM, STEM/EDX)	114
IV.2.3 DYNAMIC LIGHT SCATTERING (DLS)	114
IV.2.4 INDUCTIVELY COUPLED PLASMA-MASS SPECTROMETRY (ICP-MS)	114
IV.2.5 BULK MAGNETIC SUSCEPTIBILITY	116
IV.2.6 ¹ H RELAXIVITY	116
IV.2.7 MOLECULAR MODELING	117
IV.3 RESULTS AND DISCUSSION	118
IV.3.1 PARTICLES SIZE DISTRIBUTIONS.	118
IV.3.2 DTNP STRUCTURAL DESCRIPTION	121
IV.3.3 MOLECULAR MODELING	123
IV.3.4 STEM/EDX	125
IV.3.5 ICP/MS	127
IV.3.6 MAGNETIC PROPERTIES	127
IV.3.7 ¹ H RELAXIVITY	131
IV.4 CONCLUSION	137
IV.5 ACKNOWLEDGEMENTS	138
IV.6 REFERENCES	139

CHAPTER V.

CONCLUSIONS AND PERSPECTIVES	141
V.1 CONCLUSIONS	143
V.2 PERSPECTIVES	147
V.3 REFERENCES	150

CHAPTER VI.

APPENDIX	153
TABLE OF CONTENTS OF CHAPTER VI	155
VI.1 APPENDIX TO CHAPTER II:	157
VI.1.1 PROTONATION AND STABILITY CONSTANTS BY POTENTIOMETRIC MEASUREMENTS	157
VI.1.2 ¹ H-NMR IN D ₂ O	159
VI.1.3 CONDITIONAL RELATIVE STABILITY CONSTANT $K_{L1/L2}^*$ OF [Gd(DTTA-ME)(H ₂ O) ₂] ⁻ RELATIVE TO [Gd(DTPA-BMA)(H ₂ O)]	160
VI.1.4 TRANSMETALLATION OF [Gd(DTTA-ME)(H ₂ O) ₂] ⁻ WITH ZN ²⁺	165
VI.1.5 SEARCH FOR ADDUCT FORMATION BETWEEN [Gd(DTTA-ME)(H ₂ O) ₂] ⁻ AND L-LACTATE	166
VI.2 APPENDIX TO CHAPTER III: EXPERIMENTAL DATA	167
VI.2.1 SUIVI THEORIQUE PAR RMN DE LA FORMATION DE RU ^{II} [Y ₂ BIPY(DTTA) ₂] ₃ ·NA ₄	175
VI.2.2 SUIVI PRATIQUE PAR RMN DE LA FORMATION DE RU ^{II} [Y ₂ BIPY(DTTA) ₂] ₃ ·NA ₄	176
VI.2.3 {RU[Gd ₂ BPY-DTTA ₂ (H ₂ O) ₄] ₃ } ⁴⁺ AND {FE[Gd ₂ BPY-DTTA ₂ (H ₂ O) ₄] ₃ } ⁴⁺ RELAXIVITIES (NMRDs)	180
VI.3 APPENDIX TO CHAPTER IV	181
VI.3.1 GD-DTNP(1), GD-DTNP(2) ANB GD-DTNP(3) RELAXIVITIES (NMRD)	181
 CURRICULUM VITAE	 183
PUBLICATIONS	185
PRESENTATIONS	187

ABSTRACT

Since contrast agents are used in magnetic resonance imaging (MRI), numerous efforts have been done to increase their relaxivity (parameter allowing to quantify contrast agent efficiency). Few years ago, the Merbach group developed the chelating agent DTTA ($H_4DTTA = \text{diethylenetriaminetetraacetic acid} = N,N'$ -[iminobis(ethane-2,1-diyl)]bis[*N*-(carboxymethyl)glycine]), which contains when complexed with gadolinium(III) in aqueous solution two inner-sphere coordination sites for water molecules. This chelate unit complexed with gadolinium(III) presents also a relatively fast inner-sphere water exchange rate which is favorable for the relaxivity.

Three types of compounds have been studied in this thesis, all of them containing the DTTA chelate unit. The first is considered to be the monomer and allows studying the stability of the chelate unit. The second is a close derivative to the metallostar compound $\{Fe[Gd_2bpy-DTTA_2(H_2O)_4]_3\}^{4+}$, when the iron(II) central ion is replaced by a ruthenium(II) ion. The third is represented by the DTTA thiol derivative coated to gold nanoparticles.

The first part of this thesis, chapter II, is thus the study of the physicochemical properties of the DTTA chelating moiety. For this purpose, the methylated derivative $H_4DTTA-Me$ (N,N' -[(methylimino)bis(ethane-2,1-diyl)]bis[*N*-(carboxymethyl)glycine]) was synthesized. Protonation and deprotonation constants of the ligand were determined in an aqueous solution by potentiometry and 1H NMR pH titration and compared to various DTTA derivatives. Stability constants were measured for the chelates formed with Gd^{3+} ($\log K_{GdL} = 18.60 \pm 0.10$) and Zn^{2+} ($\log K_{ZnL} = 17.69 \pm 0.10$). A novel approach of determining in a direct way the relative conditional stability constant of two paramagnetic complexes by 1H NMR relaxometry is presented and was used for the Gd^{3+} complexes $[Gd(DTTA-Me)(H_2O)_2]^-$ (L_1) and $[Gd(DTPA-BMA)(H_2O)]$ (L_2) [$K_{L1/L2}^*$ (at pH 8.3, 25°C) = 6.4 ± 0.3]. The transmetalation reaction of the Gd^{3+} complex with Zn^{2+} in phosphate buffer solution (pH 7.0) was measured to be twice as fast for $[Gd(DTTA-Me)(H_2O)_2]^-$ in comparison to that for $[Gd(DTPA-BMA)(H_2O)]$. This can be rationalized by the higher affinity of Zn^{2+} toward $DTTA-Me^{4-}$ if compared to $DTPA-BMA^{3-}$. The formation of a ternary complex with L-lactate, which is

common for DO3A-based heptadentate complexes, has not been observed for $[\text{Gd}(\text{DTTA-Me})(\text{H}_2\text{O})_2]^-$ as monitored by ^1H NMR relaxometric titrations. From the results, it was concluded that the heptadentate DTTA-Me^{4-} behaves similarly to the commercial octadentate DTPA-BMA^{3-} with respect to stability. Considering recent suspicions against $[\text{Gd}(\text{DTPA-BMA})(\text{H}_2\text{O})]$ for being involved in Nephrogenic Systemic Fibrosis (NSF) disease, DTTA-type chelates will not be admitted as contrast agents in clinical MRI. However, their use *in vitro* and in animal studies is absolutely conceivable, mainly at high magnetic fields, where the increase of inner-sphere-coordination water actually seems to be the only promising way to increase the relaxivity markedly.

The second part of this thesis, chapter III, presents the synthesis in aqueous solution and the magnetic and optical properties of the Ru(II)-based metallostars $\text{Na}_4\{\text{Ru}[\text{Ln}_2\text{bpy-DTTA}_2(\text{H}_2\text{O})_4]_3\}$ ($\text{Ln} = \text{Y}, \text{Gd}, \text{and Eu}$). The synthesis and the purification of the new, highly stable heptametallic entities have been optimized for the diamagnetic Y^{3+} complex and followed by ^1H NMR. The europium(III) ruthenium-based metallostar $\{\text{Ru}[\text{Eu}_2\text{bpy-DTTA}_2(\text{H}_2\text{O})_4]_3\}^{4-}$ displays sensitized $^5\text{D}_0 \rightarrow ^7\text{F}_J$ luminescence upon excitation of the tris-(2,2'-bipyridyl)ruthenium(II) unit in both the ultraviolet around 293 nm, as well as in the visible around 450 nm ($^1\text{MLCT}$ state). NMRD profiles at two temperatures (25°C and 37°C) were measured on the $\{\text{Ru}[\text{Gd}_2\text{bpy-DTTA}_2(\text{H}_2\text{O})_4]_3\}^{4-}$. NMRD profiles of the ruthenium-based $\{\text{Ru}[\text{Gd}_2\text{bpy-DTTA}_2(\text{H}_2\text{O})_4]_3\}^{4-}$ and iron-based $\{\text{Fe}[\text{Gd}_2\text{bpy-DTTA}_2(\text{H}_2\text{O})_4]_3\}^{4-}$ metallostars were fitted with SBM theory coupled to the model-free Lipary-Szabo method for internal motion as well as with the modified Florence approach. Comparison of both fitting methods shows that the Florence approach is able to fit NMRD profiles up to 100 MHz, fails however at higher frequencies because it does not account for internal motion. Overall, the results detailed point to the heptametallic self-assembled edifices being potential relaxivity and luminescence bimodal bioprobes.

The third part of this thesis, chapter IV, is devoted to nano objects. We developed small, water-dispersible, stable nanoparticles covalently linked to Ln-DTTA derivative complexes (with $\text{Ln} = \text{Gd}$ and Y) on the surface. Characterizations of these DTTA thiol capped gold nanoparticles (Gd-DtNP) using TEM images, dynamic light scattering technique and STEM with EDX analysis indicate 1.5-15.5 nm particle diameters, coated by Ln-Dt complexes on the surface. Molecular modeling shows a rough distance in the range of 1.3 nm between the lanthanide(III) ion and gold core surface and the structure that possess Ln-DtNP offers to

lanthanide(III) a tightly bonding on the surface of particles. Accurate Au, Gd and Y concentrations have been determined by ICP-MS technique. Bulk magnetic susceptibility of samples with different gadolinium concentration has been established following the Evans method and no significant magnetic contribution can be attributed to the gold core. NMRD profiles of Gd-DtNP at 25°C show very high relaxivities and present broad relaxivity humps indicating very large systems with slow rotational motion. The modified Florence approach allows fitting well the experimental NMRD profil of Gd-DtNP, and the fitted electronic relaxation parameters are in good coherence with what was expected from the Ru-based metallostar values. Our Gd-DtNP systems are very rigid nano-object.

Key words: MRI, gadolinium(III), relaxivity, synthesis, DTTA, DTTA-Me, Metallostar, ruthenium(II), gold, nanoparticle, contrast agent.

RÉSUMÉ

Depuis l'utilisation d'agents de contraste en imagerie par résonance magnétique (IRM), de nombreux efforts sont dirigés vers l'augmentation de la relaxivité (paramètre qui permet de quantifier l'efficacité d'un agent de contraste). Il y a maintenant quelques années, le groupe Merbach a mis au point l'agent chélatant DTTA (H_4DTTA = acide diéthylène triaminetetra acétique = N,N' -[iminobis(ethane-2,1-diyl)]bis[N -(carboxyméthyl)glycine]) qui laisse, lorsqu'il est complexé au gadolinium(III) en milieu aqueux, deux sites de coordination en première sphère pour des molécules d'eau. Cette unité chélatante a de plus une vitesse d'échange d'eau en première sphère assez rapide, ce qui est favorable à la relaxivité.

Trois types de composés ont été étudiés dans cette thèse, tous trois contenant l'unité chélatante DTTA. Le premier, le plus petit, est considéré comme le monomère et permet d'étudier la stabilité de l'unité chélatante. Le deuxième est un dérivé du composé métallostar $\{Fe[Gd_2bpy-DTTA_2(H_2O)_4]_3\}^{4+}$, ou le fer central a été remplacé par un ion ruthénium(II). Le troisième est représenté par des nanoparticules d'or contenant à la surface des dérivés thiolés de cette unité chélatante.

La première partie de la thèse, le chapitre II, est donc l'étude des propriétés physico-chimiques de l'unité chélatante DTTA, et ceci à l'aide du dérivé méthylé synthétisé $H_4DTTA-Me$ (N,N' -[(méthylimino)bis(ethane-2,1-diyl)]bis[N -(carboxyméthyl)glycine]). Les constantes de protonation et de deutération du ligand ont été déterminées en solution aqueuse par potentiométrie et par titration pH en utilisant la RMN du proton. Ces constantes ont été comparées à d'autres dérivés DTTA. Les constantes de stabilité ont été mesurées pour des complexes formés avec l'ion gadolinium(III) ($\log K_{GdL} = 18.60 \pm 0.10$) et le ion zinc(II) ($\log K_{ZnL} = 17.69 \pm 0.10$). Une nouvelle approche est présentée pour la détermination de manière directe d'une constante conditionnelle de stabilité relative de deux complexes paramagnétiques par RMN du proton et a été utilisée pour les complexes $[Gd(DTTA-Me)(H_2O)_2]^-$ (L_1) et $[Gd(DTPA-BMA)(H_2O)]$ (L_2) [$K_{L1/L2}^*$ (à pH 8.3, 25°C) = 6.4 ± 0.3]. La réaction de transmétallation pour le complexe de $[Gd(DTTA-Me)(H_2O)_2]^-$ avec du Zn^{2+} dans une solution tamponnée phosphate (pH 7.0) a été mesurée et s'est révélée deux fois plus

rapide que pour le complexe de $[\text{Gd}(\text{DTPA-BMA})(\text{H}_2\text{O})]$. Ceci peut être rationalisé par une plus grande affinité du zinc(II) pour le ligand DTTA-Me^{4-} en comparaison au ligand DTPA-BMA^{3-} . La formation du complexe ternaire avec un L-lactate, observé par titration relaxométrique en RMN du proton n'a pas été observée pour le complexe $[\text{Gd}(\text{DTTA-Me})(\text{H}_2\text{O})_2]^-$, mais est courante pour les complexes heptadentés basés sur le DO3A. Ces résultats indiquent que la stabilité du ligand heptadenté DTTA-Me^{4-} est similaire à l'octadenté commercial DTPA-BMA^{3-} . En considérant les récentes suspensions sur le $[\text{Gd}(\text{DTPA-BMA})(\text{H}_2\text{O})]$ quant à son implication dans la maladie de fibrose systémique néphrogénique, les chélates du type DTTA ne seront pas admis comme agents de contraste en IRM clinique. Toutefois, l'utilisation du complexe $[\text{Gd}(\text{DTTA-Me})(\text{H}_2\text{O})_2]^-$ comme agent de contraste en condition *in vitro* et animale est tout à fait concevable, principalement à haut champs, où l'augmentation du nombre de molécules d'eau en première sphère de coordination du gadolinium(III) semble être la meilleure voie pour augmenter la relaxivité.

La deuxième partie de la thèse, le chapitre III, présente la synthèse en solution aqueuse du composé ruthénium(II) du Metallostar $\text{Na}_4\{\text{Ru}[\text{Ln}_2\text{bpy-DTTA}_2(\text{H}_2\text{O})_4]_3\}$ ($\text{Ln} = \text{Y}, \text{Gd}, \text{et Eu}$), ainsi que ces propriétés magnétiques et optiques. La synthèse et la purification de cette nouvelle entité heptamétallique ont été optimisées sur le complexe yttrium(III) et suivi par RMN du proton. Le complexe europium(III) $\{\text{Ru}[\text{Eu}_2\text{bpy-DTTA}_2(\text{H}_2\text{O})_4]_3\}^{4-}$ présente une transition de type ${}^5\text{D}_0 \rightarrow {}^7\text{F}_1$ après excitation de l'unité tris-(2,2'-bipyridyl)ruthenium(II) luminescent aux deux longueurs d'onde suivantes : dans l'ultraviolet autour de 293 nm, et dans le visible autour de 450 nm (état ${}^1\text{MLCT}$). Les profils NMRD ont été effectués sur le complexe $\{\text{Ru}[\text{Gd}_2\text{bpy-DTTA}_2(\text{H}_2\text{O})_4]_3\}^{4-}$ à deux températures (25°C et 37°C). Les fits des profils NMRD des Metallostars du ruthénium(II) $\{\text{Ru}[\text{Gd}_2\text{bpy-DTTA}_2(\text{H}_2\text{O})_4]_3\}^{4-}$ et du fer(II) $\{\text{Fe}[\text{Gd}_2\text{bpy-DTTA}_2(\text{H}_2\text{O})_4]_3\}^{4-}$ ont été effectués à l'aide de la théorie de Solomon-Bloembergen-Morgan (S-B-M) couplée au model développé par Lipary-Szabo, et de l'approche modifiée de Florence. La comparaison des deux méthodes de fit indique que l'approche modifiée de Florence est la seule capable de fitter les profils NMRD correctement jusqu'à 100 MHz, mais échoue par contre à des champs plus élevés car elle ne prend pas en compte les mouvements internes. Parmi tous les résultats présentés dans le chapitre III, nous avons réussi à démontrer que le ruthénium(II) Metallostar est un objet heptamétallique auto-assemblé ayant un potentiel comme agent bimodal (magnétique et luminescent).

La troisième partie de la thèse, le chapitre IV, se concentre sur des objets nanoparticulaires. Nous avons développé de petites nanoparticules, stables et solubles en solution aqueuse, liées de manière covalente à des complexes contenant l'unité chélatante $[\text{Ln}(\text{DTTA})(\text{H}_2\text{O})_2]^-$ avec $\text{Ln}=\text{Gd}$ et Y . La caractérisation de ces nanoparticules entourées de DTTA thiolés (Ln-DtNP) a été effectuée en utilisant des images TEM, la technique de diffusion dynamique de la lumière (DLS) et le STEM avec analyse EDX, et indique des diamètres de 1.5-15.5 nm et la présence des complexes Ln-Dt à la surface des nanoparticules. La modélisation moléculaire indique une distance d'environ 1.3 nm entre les centres lanthanides et la surface des nanoparticules et que la structure des nano-objets Ln-DtNP offre aux centres lanthanide(III) un environnement de grande promiscuité. Grâce à la technique de l'ICP-MS (induced coupled plasma–mass spectrometry), les concentrations d'or, de gadolinium et d'yttrium ont été établies avec précision. La susceptibilité magnétique du bulk de solutions de Gd-DtNP de différentes concentrations a été établi à l'aide de la méthode d'Evans. Nous n'avons pas observé de contribution magnétique significative provenant des corps d'or. Les profils NMRD à 25°C indiquent de très grandes relaxivités, jusqu'à haut champs (< 200 MHz) et indiquent une large bosse à moyen-haut champs, montrant la présence de très grands systèmes ayant un mouvement rotationnel lent. L'approche modifiée de Florence permet de fitter correctement les points expérimentaux du profil NMRD du composé $\text{Gd-DtNP}(1)$. Les paramètres électroniques de fit sont cohérents avec ceux obtenus pour les Metallostars. Nos systèmes Gd-DtNP sont de très rigides nano-objets.

Mots clés: IRM, gadolinium(III), relaxivité, synthèse, DTTA, DTTA-Me, Metallostar, ruthénium(II), or, nanoparticule, agent de contraste.

ACKNOWLEDGEMENTS

After four years, and a physico-chemical study of the ligand DTTA-Me, a demanding synthesis of the Ru-based metallostar, numerous ^1H NMR measurements on my samples and on samples coming from collaborations, a nice overview on dendrimeric structures and on the Gd-loaded nanotubes subject, an interesting dynamic molecular study, an exciting project on gold nanoparticles, I want to express here my grateful reconnaissance to important persons which helped me doing this work.

First, I would like to express my deep gratitude to Prof. André E. Merbach. He offered me a strong inorganic chemical education, with stringent clarity. My complete first chapter is dedicated to him. On behalf on this physico-chemical work, I would like to express my gratitude to Dr. Caroline Cannizzo, Florent Beryère and Cora Prestinari for their huge contributions.

Dr. Angélique Sour, Dr. Caroline Cannizzo, Dr. Khaja Nazeeruddin and Dr. Céline Fellay are strongly acknowledged for their helps for the synthesis of the Ru-based metallostar. This synthesis, demanding first to synthesis the well known compound $\text{Ru}^{\text{II}}(\text{H}_2\text{O})_6\text{TOs}_2$, has been terribly instructive and hopefully successful. Dr. Annina Aebisher, Dr. Steve Comby and Prof. J.-C. Bünzli performed a beautiful luminescence study and Dr. Alain Borel and Prof. Lothar Helm shared with me their strong knowledges on relaxation mechanisms. My second chapter is completely dedicated to them.

Dr. Cédric Mayer and Dr. Caroline Cannizzo are strongly thanked for having developed a passionating subject using gold nanoparticles as support for gadolinium chelate. Dr. Alexei Ulianov from the Institute of Mineralogy and Geochemistry (IMG) (University of Lausanne) is sincerely acknowledged for having offered me the possibility of doing ICP-MS in perfect conditions and for having given me precious informations. Dr. Marco Cantoni and Anas Mouti from the interdisciplinary center for electron microscopy (EPFL-SB-CIME) are acknowledged for the time they took to make images of my samples and for their advices. I would like to thanks also Hugues Jaccard for his help for numerous things. I acknowledge

strongly finally Prof. Lothar Helm and Prof. André Merbach for their very enthusiastic support. My third chapter is completely dedicated to all of them.

I would like also to thanks Thierry Cretton for having doing a very good work in a demanding study of the DTTA-Me by Molecular Dynamic simulation. With the compulsory help of Dr. Alain Borel and Dr. Fabrice Yerly, we succeed to reach our objective in times, and allowed helping first year master students to complete their semester projects.

Dr. Zoltán Jászberényi, Dr. Eva Toth, Dr. Joao Bruno Livramento, Dr. Jérôme Costa, Dr. Sabrina Laus, Dr. Pascal Grundler, Dr. Fabrice Riblet, Dr. Edina Balogh, Dr. Gabriella Bodizs are acknowledge for their initiation to the Merbach Group techniques during the first year of my thesis.

Martial Rey, Gladys Pache, Giovanni Petrucci, Yves Morier, Dr. Luc Patiny, Annelise Carrupt, Patrick Favre, Dr. Euro Solari, Donald Zbinden are strongly thanks for their numerous helps. Maria Szuman is also deeply acknowledged for her efficiency and her kindness.

I want to thank also strongly Prof. Lothar Helm for having accepted me as his PhD student. He applied the “open-door” office policy, enabling easy access for questions and discussions. His strong feeling for physical concepts was compulsory for achieving my thesis. Moreover, he contributed significantly to improve the manuscript presented in this thesis.

Finally, I want to acknowledge deeply Mumu, my parents, Anne and Ulysses, my brother, Cédrick, my sister, Annouck, my grandparents, Evelyne and Jean-Daniel, all my friends and the rest of my family, for what they are and what they do for me.

SYMBOLS AND ABBREVIATIONS

Chemical formulas

AIBN	azobisisobutyronitrile
BEATA ⁴⁻	<i>N,N</i> -bis(2-aminoethyl)aniline- <i>N',N',N'',N''</i> -tetraacetate
BEBTA ⁴⁻	[(benzylimino)bis(ethylenitrilo)]tetraacetate
bpy	bipyridine
DO3A ³⁻	1,4,7,10-tetraazacyclododecane- <i>N,N',N''</i> -triacetate
DOTA ⁴⁻	1,4,7,10-tetraazacyclododecane- <i>N,N',N'',N'''</i> -tetraacetate
DTPA ⁵⁻	diethylenetriamine- <i>N,N,N',N'',N'''</i> -pentaacetate
DTPA-BMA ³⁻	1,7-bis[<i>N</i> -methylcarbonylmethyl]-1,4,7-triazaheptane-1,4,7-triacetate
DTTA ⁴⁻	diethylenetriamine- <i>N,N,N',N''</i> -tetraacetate
DTTA-Me ⁴⁻	<i>N,N'</i> -[(methylimino)bis(ethane-2,1-diyl)]bis[<i>N</i> -(carboxymethyl)glycine]
DTTA-prop ⁵⁻	diethylenetriamine- <i>N,N,N',N''</i> -tetraacetic- <i>N'</i> -propionic acetate
DPTPA ⁵⁻	dipropylenetriamine- <i>N,N,N',N'',N'''</i> -pentaacetate
EDTA ⁴⁻	1,2-ethylenediamine- <i>N,N,N',N''</i> -tetraacetate
EGTA ⁴⁻	ethylenebis(oxyethylenitrilo)tetracetate
EPTPA ⁵⁻	ethylenepropylenetriamine- <i>N,N,N',N'',N'''</i> -pentaacetate
EPTPA-bz-NO ₂ ⁵⁻	(<i>p</i> -nitrobenzyl) ethylenepropylenetriamine- <i>N,N,N',N'',N'''</i> -pentaacetate
HEPES	2-[4-(2-hydroxyethyl)-1-piperazinyl]ethanesulfonic acid)
HSA	human serum albumin
mX(DTTA) ₂ ⁸⁻	bis(diethylenetriamine- <i>N,N,N',N''</i> -tetraacetate)- <i>m</i> -xylene
PAAHC	polyallylamine hydrochloride
PAMAM	poly(amidoamine)
PAN	polyacrylonitril
PBS	phosphate buffered saline
PVP	poly- <i>N</i> -vinyl-2-pyrrolidone
pX(DTTA) ₂ ⁸⁻	bis(diethylenetriamine- <i>N,N,N',N''</i> -tetraacetate)- <i>p</i> -xylene
SDBS	sodium dodecylbenzenesulphonate
TETA ⁴⁻	1,4,8,11-tetraazacyclotetradecane-1,4,8,11-tetraacetate
terpy	2,2':6',2''-terpyridine
tpy-DTTA ⁴⁻	4'-(diethylenetriamino- <i>N',N',N'',N'''</i> -tetraacetate)-2,2':6',2''-terpyridine
TTAHA	<i>N</i> -tris(2-aminoethyl)amine- <i>N',N',N'',N''',N''''</i> -hexaacetate

Experimental techniques

DLS	Dynamic Light Scattering
EPR	Electron Paramagnetic Resonance
ESI-MS	ElectroSpray Ionization – Mass Spectrometry
ICP-MS	Inductive Coupled Plasma – Mass Spectrometry
MRI	Magnetic Resonance Imaging
MRT	Magnetic Resonance Tomography
NMR	Nuclear Magnetic Resonance

NMRD	Nuclear Magnetic Relaxation Dispersion
STEM	Scanning Transmission Electron Microscopy
TEM	Transmission Electron Microscopy
UV-Vis	Ultra-Violet-Visible
XAFS	X-ray Absorption Fine Structure

Symbols

\hbar	Planck's constant divided by 2π
A/ \hbar	hyperfine or scalar coupling constant
a_{GdH}	distance of closest approach of bulk water protons to the Gd^{III} centre
B	magnetic field
C_{OS}	outer sphere constant
CO	cuboctahedron
D_{diff}^{298}	constant for intermolecular translational diffusion
D_{H}	hydrodynamic diameter
D_{GdH}	diffusion coefficient
DtNP	DTTA thiol capped gold nanoparticles
E_{DGdH}	activation energy for the diffusion
E_{R}	activation energy for the rotational correlation time
E_{v}	activation energy for the modulation of the ZFS
fcc	Face-centered cubic
g_{L}	isotropic Landé factor
h	Planck's constant
I	nuclear spin
k_{B}	Boltzmann constant
k_{ex}	water exchange rate
K_{i}	thermodynamic protonation constant
K_{i}^{D}	thermodynamic deuteration constant
$K_{\text{L1/L2}}^*$	conditional relative stability constant
K_{ML}	thermodynamic stability constant
K_{ML}^*	conditional stability constant
LD_{50}	lethal dose of a substance which leads, given in a single dosis, to the death of 50% of a population
N_{A}	Avogadro's number
NSF	nephrogenic systemic fibrosis
P	pressure
P_{m}	mole fraction of bound water
p_{O_2}	oxygen partial pressure
q	hydration number
R	perfect gas constant
$R_{1(2)}$	longitudinal (transverse) relaxation rate
$r_{1(2)}$	longitudinal (transverse) proton relaxivity
r_{GdH}	effective Gd^{III} electron spin-water protons distance
r_{GdO}	mean gadolinium(III)-oxygen distance
S	electron spin
S^2	degree of spatial restriction of the local motion

SPIO	superparamagnetic iron oxide
T	temperature
$T_{1(e)}$	(electronic) longitudinal relaxation time
$T_{1(2)m}$	longitudinal (transverse) relaxation time of a bound water molecule
$T_{2(e)}$	(electronic) transverse relaxation time
TO	truncated octahedron
ZFS	zero field splitting
Δ^2	trace of square of the ZFS tensor
ΔH^\ddagger	activation enthalpy for the water exchange
ΔH_{pp}	peak-to-peak EPR linewidth
Δ_s^2	static ZFS parameter
Δ_t^2	transient ZFS parameter
Δ_x	^1H -NMR shift observed between two proton NMR signals
χ	quadrupolar coupling constant
γ_I	nuclear gyromagnetic ratio
γ_S	electronic gyromagnetic ratio
η	- asymmetry parameter (quadrupolar relaxation) - viscosity (Debye-Stokes equation)
μ_0	vacuum permeability
μ_B	Bohr magneton
μ_{eff}	effective magnetic moment
ν	frequency
τ_g	correlation time of the slow global motion
τ_l	correlation time of the rapid local motion
τ_m	mean residence time of a bound water molecule
τ_{RH}	rotational correlation time for the $\text{Gd}^{\text{III}}\text{-H}_{\text{water}}$ vector
τ_{RO}	rotational correlation time for the $\text{Gd}^{\text{III}}\text{-O}_{\text{water}}$ vector
τ_v	correlation time for the modulation of the ZFS
ω	angular frequency
ω_I	proton resonance frequency
ω_m	chemical shift difference between bound and bulk water
ω_S	Larmor frequency of the S spin

CHAPTER I.

INTRODUCTION

TABLE OF CONTENTS CHAPTER I

<u>I.1</u>	<u>MAGNETIC RESONANCE IMAGING : OVERVIEW</u>	<u>25</u>
I.1.1	MAGNETIC RESONANCE IMAGING (MRI)	25
I.1.2	Gd(III)-COMPLEXES AS MRI CONTRAST AGENTS	29
I.1.3	THERMODYNAMIC STABILITIES	30
I.1.4	PARAMAGNETIC RELAXATION ENHANCEMENT (PRE) THEORY	30
I.1.4.1	MECHANISMS INDUCED BY PARAMAGNETIC SPECIES	31
I.1.4.2	RELAXIVITY R_1	32
I.1.4.3	^1H NMR DISPERSION (NMRD) FIT	35
I.1.5	NANOPARTICLES	36
<u>I.2</u>	<u>SCOPE OF THE THESIS</u>	<u>37</u>
<u>I.3</u>	<u>REFERENCES</u>	<u>40</u>

I.1 MAGNETIC RESONANCE IMAGING : OVERVIEW

I.1.1 Magnetic Resonance Imaging (MRI)

Magnetic resonance imaging (MRI) is known as a harmless and non-invasive diagnostic imaging technique, allowing images of biological tissues having substantial populations of atomic nuclei that are susceptible to nuclear magnetic resonance (NMR). Magnetic resonance imaging is also known as magnetic resonance tomography (MRT).

Magnetic resonance imaging has proven to be a useful technology both for the detection and diagnosis of human disease as well as for research into the understanding of basic animal physiology. MRI is well suited to the visualization of soft tissues and is primarily used for diagnosing disease pathologies and internal injuries.

In general, magnetic resonance imaging is a technique of applying a gradient magnetic field and a radio frequency (RF) wave to a subject in a static magnetic field, producing an image based on magnetic resonance signals emitted from protons in a region examined. (Figure I.1-1) MRI systems include a super conducting magnet capable of producing a strong, homogenous magnetic field; a radio frequency (RF) transmitter and receiver system; a gradient coil system, all three surrounding the patient; and a computer receiving the signals from the receiver coil and processing the signals into images.

MRI utilizes hydrogen nuclear (proton) spins of the water molecules in the human body, which are polarized by the strong static homogenous magnetic field generated by the magnet. The reason is that the human body is primarily water and fat. Water and fat have many hydrogen atoms that make the human body approximately 63% hydrogen atoms. Moreover, given that hydrogen nuclei have 99.985% natural abundance and are very sensitive in NMR, magnetic resonance imaging thus images the NMR signal of the hydrogen nuclei.

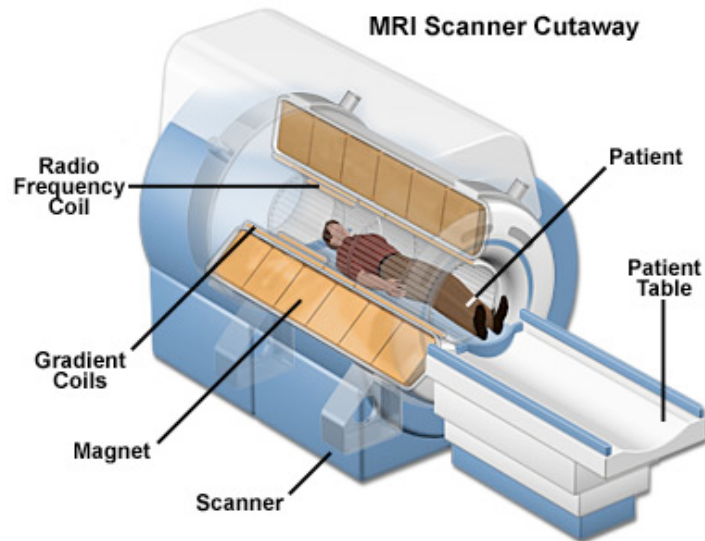


Figure I.1-1: MRI scanner. Superconducting magnet surrounded by liquid helium lines up the water protons inside the body and the radio transceiver causes the water protons to flip on their axes.¹

More precisely, when the high frequency magnetic field is applied to the subject placed in the homogeneous static magnetic field, it excites proton nuclear spins within the patient's tissues. The excited proton spins rotate at a rate dependent upon the static magnetic field. As they flip, they emit radio frequency signals, referred as magnetic resonance signals. MRI detects these nuclear magnetic resonance (NMR) signals given off by protons after excitation. The detected signals are functions of the tissue and the strength of the magnetic field. By applying magnetic field gradients (Figure I.1-2) so that the magnitude of the magnetic field varies with location within the patient's body, the magnetic resonance phenomenon can be limited to only a particular region, or slice, of the patient's body, so that all of the detected magnetic resonance signals come from that slice.

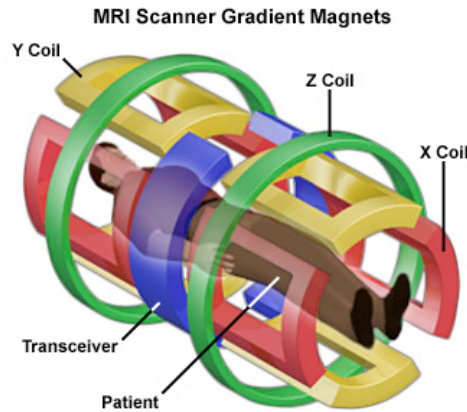


Figure I.1-2: MRI Scanner gradient magnets, modifying the magnetic field at very particular points (voxel). Work in conjunction with the radio frequency (RF) pulses to produce the scanner's picture by encoding the spatial distribution of the water protons.¹

The signal intensity of a volume element, a voxel, composing the slice depends not only on the quantity of protons present in this voxel but also on the ability the protons have to return to the equilibrium state after being excited with the radio frequency pulse, that means their relaxation properties. The return of excited nuclei from the high-energy state to the low energy or ground state is associated with loss of energy to the surrounding nuclei. Macroscopically, relaxation can be characterized by the longitudinal return of the magnetization to its ground state in the direction of the main magnetic field. In this thesis, we will be focused in so-called T_1 -contrast agent. The T_1 longitudinal relaxation time is the time for the magnetization to return to 63% of its original value. Spins are considered completely relaxed after 3-5 T_1 times. T_1 relaxation is fastest when the motion of the nucleus (rotations or "tumbling rate" and translations) matches the Larmor frequency. As a result, T_1 relaxation is dependent on the main magnetic field strength that specifies the Larmor frequency. Higher magnetic fields are often associated with longer T_1 times.

Different tissues have different T_1 values. For example, fluids have long T_1 (1500-2000 ms), and water based tissues are in the 400-1200 ms range, while fat based tissues are in the shorter 100-150 ms range. The contrast of the image is provided by the intensity differences between the voxels. The 2D image is composed of pixels which intensities are proportional to the signal intensity of the corresponding voxel. Images of soft tissues in the body like muscles, spinal cord or brain (Figure I.1-3 and I.1-4), are normal outcomes of an MRI examination.

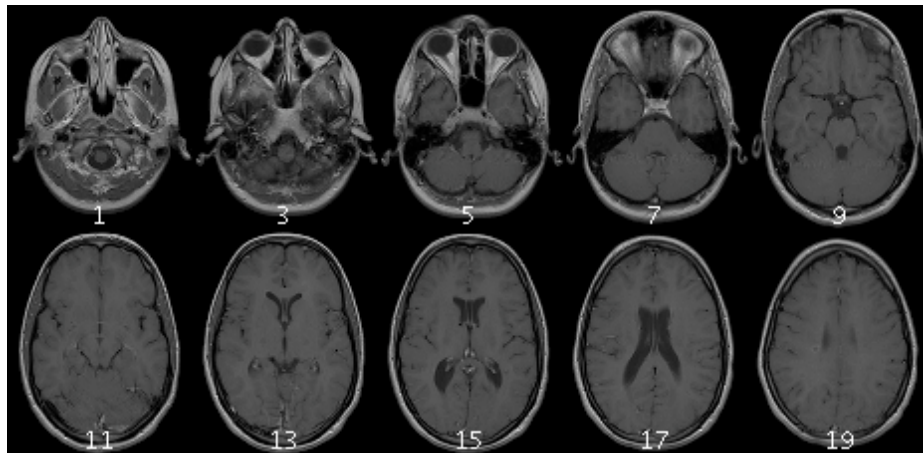


Figure I.1-3: T₁-weighted MRI images of the brain and skull – Transverse sections.²

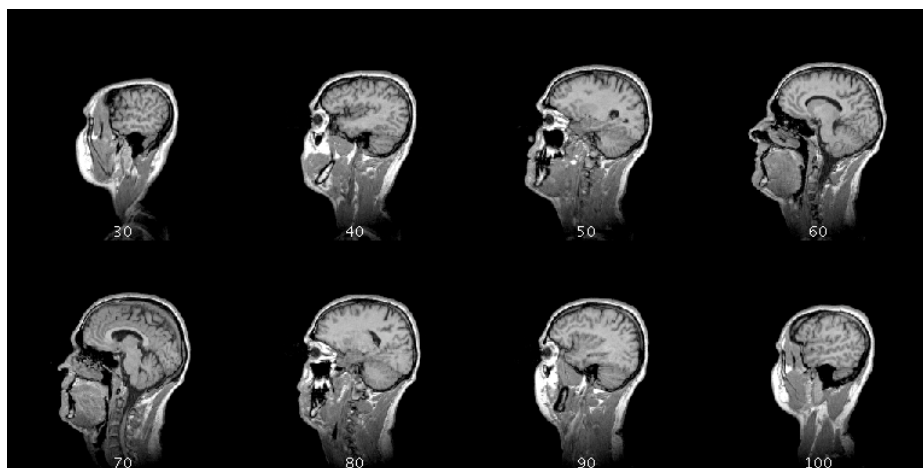


Figure I.1-4: T₁-weighted MRI images of the brain and skull – Sagittal sections.²

The duration of a MRI examination may be painful and the contrast between the tissues and in particular between healthy and diseased tissues might be not sufficient to ensure the early detection of a tumor. Thus, in many cases, the successful use of MRI would not have been possible without a class of pharmacological products, called contrast agents. The role of the contrast agent is to accelerate the relaxation of the surrounding protons, allowing reducing the examination time and improving the contrast of the image.

I.1.2 Gd(III)-complexes as MRI contrast agents

The effectiveness of an MRI contrast agent is usually measured in terms of relaxivity; the paramagnetic enhancement of the longitudinal relaxation rate of water protons in presence of 1 mM paramagnetic ion concentration. Agents based on Mn^{2+} , Mn^{3+} , Fe^{3+} and Cu^{2+} paramagnetic ions have been studied, but Gadolinium (III) complexes are far the most widely used contrast media in clinical practice.³ This choice is explained by the fact that the lanthanide Gd^{3+} ion has seven unpaired electrons, which make it the most paramagnetic metal ion, and has also a relatively slow electronic relaxation, optimizing the relaxation enhancement of surrounding protons.

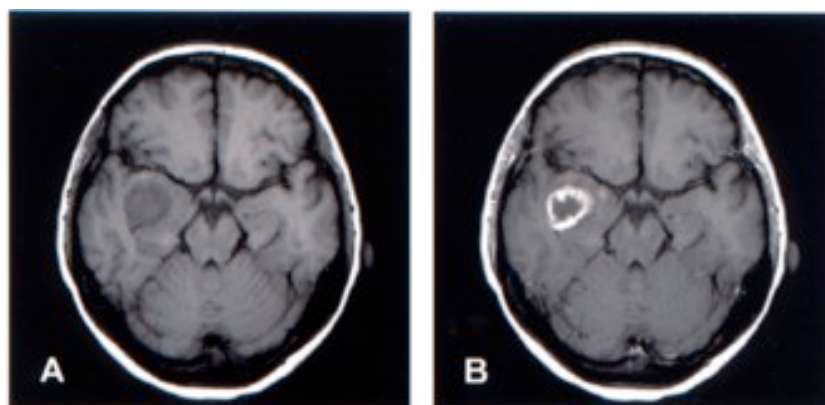


Figure I.1-5: MR images of a human brain before (A) and after (B) injection of a Gd^{3+} contrast agent.

The free gadolinium (III) ion cannot be injected however into living organisms as it induces toxicity in many ways. Gadolinium (III) can form hydroxo complexes and precipitate at physiological pH. It can also replace other metal ions in enzymes, or may interfere in Ca^{2+} regulated signal transmission processes due to its similar size to calcium(II). (LD50 values for free Gadolinium (III) are in the range of 0.1-2 mmol/kg)

The requirement of being non-toxic imposes Gadolinium (III) ions to be complexed, and given that lanthanide complexes are predominantly of ionic nature, stable complex can be achieved only with multidentate ligands as poly(aminocarboxylates). Thermodynamic stability and kinetic inertness of these complexes become thus the most important criteria for safe *in vivo* applications.

I.1.3 Thermodynamic stabilities

The thermodynamic stability constants K_{ML} of a Gd^{3+} complex, which is related to its safety as MRI contrast agent, are most often determined by pH-potentiometric titration. Given the protonation constants of the ligand are necessary for calculation of the complex stability constant, the ligand is titrated in the presence and absence of metal ions. Potentiometric titration technique works well when equilibrium is reached rapidly which is usually the case for linear ligands. For macrocyclic compounds, such as DOTA, complex formation is very slow and other technique as batch method^{4, 5} is used instead of direct titration. The protonation order of the donors groups of the ligands and protonation constants K_i can be calculated as well according to 1H NMR titration curve.

In vivo toxicity and complex stability correlation is an important question in contrast agent field. Endogenously, Gd^{3+} complex, free ligand and free metal can each participate in many side reactions. For instance, Gd^{3+} complexes can interact with endogenous metal ions following transmetallation process, inducing replacement of endogenous metal by Gd^{3+} in metabolic process. Conditional stability constants K_{ML}^* at physiological pH, which are correlated to the selectivity of a given ligand for Gd^{3+} over endogenous metals, are thus widely used to compare the behavior of different complexes. Based on simple model, Laurent and al.⁶ studied the physicochemical properties of clinical low molecular weight gadolinium contrast agents under identical experimental conditions, in three different media (pure water, zinc(II)-containing aqueous solutions and HSA-containing solutions). Osmolality, viscosity and stability versus transmetallation by zinc(II) ions were carried out for more comprehensive description. Terreno et al.⁷ describe also a multinuclear NMRD relaxometry study of ternary adducts formed between heptadentate Gd^{3+} chelates and L-lactate. Several models have been proposed in the literature also to simulate coordination equilibria in the blood plasma.⁸⁻¹⁰

I.1.4 Paramagnetic relaxation enhancement (PRE) theory

Randomly fluctuating magnetic fields cause relaxation of excited proton spins. The longitudinal T_1 relaxation time representing the spin-lattice relaxation is the time for the NMR signal to recover 63% of its initial value. The name spin-lattice relaxation refers to the fact that the spins give the energy they obtained from the radio-frequency pulse back to the

surrounding lattice in order to restore their equilibrium state before being flipped into the magnetic transverse plane and thus characterizes the rate at which the longitudinal M_z component of the magnetization vector recovers.

$$M_z(t) = M_0 \left(1 - e^{-t/T_1} \right) \quad \text{I.1-1}$$

The important source of randomly fluctuating fields comes from the unpaired electrons of the paramagnetic metal center. The paramagnetism of a compound can affect nuclear spins by inducing chemical shifts and by increasing the nuclear relaxation rates. Depending on the paramagnetic substance, it can be used as an effective shift or relaxation reagent. For instance, Tm(III) and Dy(III) complexes have been applied as ^{23}Na shift reagents¹¹ and Gd(III) complexes are used as contrast agent in MRI.³

Relaxation and chemical shift mechanisms induced by paramagnetic species

In general terms, a paramagnetic species can induce a nuclear spin relaxation and a chemical shift in nuclear resonance frequencies via three general mechanisms: the diamagnetic, the bulk susceptibility and the hyperfine mechanisms.

Diamagnetic shifts are generally related to the induced shifts in nuclei of a ligand during complex formation with a metal ion. The diamagnetic shift is that which would have been observed if the metal contained no unpaired electrons. The diamagnetic contributions in comparison with the paramagnetic contributions are usually small and may often be neglected.

The second mechanism, the bulk magnetic susceptibility, originates from the partial alignment of the magnetic moments of the paramagnetic species by the magnetic field. Because of this partial alignment, the bulk magnetic susceptibility of an entire sample is affected. The use of an inert molecule allows the determination of the influence of a paramagnetic compound on the chemical shifts considering only the bulk magnetic susceptibility.¹² To this chemical shift mechanism corresponds the Curie relaxation mechanism.¹³

The third chemical shift mechanism is the hyperfine one. There are two components of the hyperfine shift, the contact (or scalar) contribution and the dipolar (or pseudo-contact) contribution. Both of the hyperfine mechanisms require an interaction either through bond

(contact) or through space (dipolar) between the paramagnetic center and the atom, which bears the nuclear spin. To these two main chemical shift mechanisms correspond the scalar and dipolar relaxation mechanisms.

Relaxivity r_1

The paramagnetic relaxation enhancement (PRE) of a contrast agent is characterized by the relaxivity r_1 , which represents the enhancement of the free water proton longitudinal relaxation rate $R_1^{para} = 1/T_{1,para}$ per mM of paramagnetic element.

$$R_1^{obs} = \frac{1}{T_1} = R_1^{dia} + R_1^{para} = \frac{1}{T_{1,d}} + r_1 [Gd^{3+}] \quad \text{I.1-2}$$

The enhancement is due to the modulation of through-space dipole-dipole interactions between the unpaired electron spin of the paramagnetic ion and hydrogen nuclei. For convenience, the relaxivity r_1 can be separated into an inner sphere (water molecule(s) directly coordinated to the Gd(III) centre) and an outer sphere (bulk water diffusing close around the paramagnetic compound) contribution. The inner-sphere relaxivity is due to interaction between protons of the water molecule bound in the first coordination sphere of the Gadolinium (III) complex and the unpaired electron spin of the paramagnetic ion. The outer-sphere relaxivity is more a consequence of through-space interaction with protons outside the first coordination shell. From the inner sphere water contribution, the enhancement of the longitudinal relaxation rates of the hydrogen bulk water nuclei due to the exchange with the inner sphere water is given by equ. I.1-3:

$$R_1^{IS} = \left(\frac{1}{T_1} \right)^{IS} = P_m \cdot \frac{1}{T_{1m} + \tau_m} \quad \text{I.1-3}$$

The inner sphere contribution is directly proportional to the mole fraction of bound water, P_m , which is itself directly proportional to the concentration of the Gd^{3+} center and the number of water molecules coordinated to the paramagnetic ion, q . The inner sphere contribution is also inversely proportional to the sum of the mean of residence lifetime of the coordinated water molecules τ_m ($\tau_m = 1/k_{ex}$, where k_{ex} is the exchange rate constant) and their longitudinal relaxation time T_{1m} . T_{1m} is governed mainly by field dependent dipolar relaxation mechanism but also slightly by the scalar relaxation mechanism. However, since the protons of the

coordinated water are relatively far from the paramagnetic centre, the scalar relaxation mechanism represents only a negligible contribution to the overall relaxation mechanism of the first sphere coordinated water molecule. In considering only the dipolar contribution and ignoring the scalar contribution to longitudinal proton relaxation, the longitudinal relaxation time of the coordinated water T_{1m} is described (Solomon, Bloembergen theory¹⁴) as:

$$\frac{1}{T_{1m}} = \frac{2}{5} \left(\frac{\mu_0}{4\pi} \right)^2 \frac{\hbar^2 \gamma_I^2 \gamma_S^2}{r_{GdH}^6} S(S+1) \cdot [3J(\omega_I; \tau_{d1H}) + 7J(\omega_S; \tau_{d2H})] \quad \text{I.1-4}$$

where r_{GdH} is the effective distance between the gadolinium electron spin and the water protons (fixed to 3.1 Å), γ_I is the nuclear gyromagnetic ratio of the proton ($\gamma_I = 2.765 \times 10^8 \text{ rad s}^{-1} \text{ T}^{-1}$), γ_S is the electronic gyromagnetic ratio ($\gamma_S = 1.76 \times 10^{11} \text{ rad s}^{-1} \text{ T}^{-1}$), ω_I is the proton resonance frequency and $J(\omega_i; \tau_{diH})$ are the spectral density functions depending on τ_{diH} , which is the global correlation time described as:

$$\frac{1}{\tau_{diH}} = \frac{1}{\tau_m} + \frac{1}{\tau_R} + \frac{1}{T_{ie}} \text{ for } i = 1, 2 \quad \text{I.1-5}$$

τ_m , as described before, is the mean of residence lifetime of the coordinated waters ($\tau_m = 1/k_{ex}$, where k_{ex} is the exchange rate), τ_R is the rotational correlation time of the $\text{Gd}^{3+} - \text{H}_{\text{water}}$ vector of the complex and T_{ie} (τ_S) are the Gd^{3+} longitudinal and transverse electronic relaxation time.

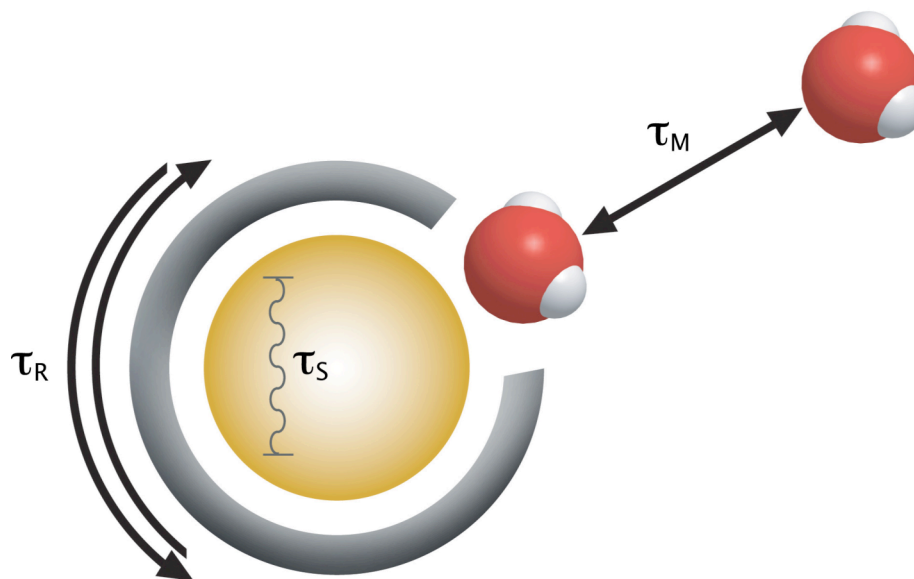


Figure I.1-6: Relaxivity of a T_1 contrast agent: influence of various parameters.¹⁵

The kinetic behavior of particles is in general described by correlation functions. Spectral density functions $J(\omega; \tau_{diH})$ are obtained from these correlation functions by Fourier transform. Assuming exponential behavior for the correlation functions leads a Lorentzian function for the spectral density functions. For instance, in considering high molecular weight molecules, the spectral density function when the tumbling is not fast enough compared to the resonance frequency (non-extreme narrowing condition) is expressed by:

$$J(\omega; \tau_{diH}) = \left(\frac{\tau_{diH}}{1 + \omega^2 \tau_{diH}^2} \right) \quad i = 1, 2 \quad \text{I.1-6}$$

In the so-called extreme narrowing conditions ($\omega^2 \tau^2 \ll 1$), the spectral density function is simplified as:

$$J_n(\omega; \tau_{diH}) = \tau_{diH} \quad \text{I.1-7}$$

Rotation is often assumed to be isotropic, however for large flexible molecules with slow rotation this may not be valid. Anisotropic rotation or internal motion within a molecule reduces the correlation time from that predicted by an isotropic model based on molecular weight. Lipari and Szabo^{16, 17} propose to distinguish two statistically independent motions, a local motion with a correlation time τ_l and a global motion with a correlation time τ_g . The

general order parameter F (called usually S^2) describes the degree of spatial restriction of the local motion. If the local motion is isotropic, $F=0$; if the rotational dynamics is only governed by the global motion, $F=1$.

$$R_{1M} = \frac{2}{15} \left(\frac{\mu_0}{4\pi} \right)^2 \frac{\gamma_I^2 g_e^2 \mu_B^2 S(S+1)}{r_{GdH}^6} \left[\underbrace{\frac{7F\tau_{d2g}}{1 + \omega_S^2 \tau_{d2g}^2} + \frac{3F\tau_{d1g}}{1 + \omega_I^2 \tau_{d1g}^2}}_{\text{global motion}} + \underbrace{\frac{7(1-F)\tau_{d2l}}{1 + \omega_S^2 \tau_{d2l}^2} + \frac{3(1-F)\tau_{d1l}}{1 + \omega_S^2 \tau_{d1l}^2}}_{\text{local motion}} \right]$$

$$\text{With } \frac{1}{\tau_{dig}} = \frac{1}{\tau_m} + \frac{1}{\tau_g} + \frac{1}{T_{1e}} \quad ; \quad \frac{1}{\tau_{dil}} = \frac{1}{\tau_{dig}} + \frac{1}{\tau_l} \quad ; \quad i = 1, 2 \quad \mathbf{I.1-8}$$

¹H NMR dispersion (NMRD) fit

The variation of relaxivity r_1 as a function of the external magnetic field is called nuclear magnetic relaxation dispersion (NMRD). For years, fits of ¹H NMRD profiles were performed with the electronic relaxation part treated following the Solomon-Bloembergen-Morgan (SBM) theory^{14, 18, 19} together with the Lipari-Szabo model-free approach^{16, 17} for internal rotation consideration (SBM-LS). In this approach the electron spin relaxation rates, $1/T_{1e}$, are due to the time dependent transient zero-field-splitting (ZFS) and no static ZFS is considered. It can be seen from numerous publications²⁰⁻²⁴ that SBM theory is not accurately able to reproduce the flat dispersion at Larmor frequencies between 0.5 and 8 MHz.

A new approach, the "modified Florence method"²⁵ has been developed by Bertini et al.²⁶ and Kruk et al.²⁷. This approach assumes a slow reorientation of the paramagnetic complex, a lack of correlation between the rotation and translation of the complex and the electron spin dynamics and includes a transient and a static ZFS.²⁷ The electron spin relaxation uses the pseudorotation model for the modulation of the transient ZFS and is described by a Redfield formulation. It has been shown that the "modified Florence method" is well-suited for fitting experimental NMRD profiles for slowly-rotating complexes of Gd³⁺.²⁵ In general, NMRD profiles are well fitted up to 100 MHz. At higher frequencies the modified Florence approach can underestimate the relaxivities because it assumes rigid molecules and neglects internal motion. The Lipari-Szabo model-free approach^{16, 17} is not yet implemented in the modified Florence approach.

I.1.5 Nanoparticles

Magnetic resonance imaging has proven to be an enormously useful technology both for the detection and diagnosis of human disease as well as for research into the understanding of basic animal physiology. MRI is well suited to the visualization of soft tissues and is primarily used for diagnosing disease pathologies and internal injuries, but its non-ability to detect the very small tumors is explained by a lack of sensitivity that is inherent to the MRI process, which detects the difference between malignant and normal tissue.

Due to their physical properties and ability to function at the cellular and molecular level of biological interactions, nanoparticles are being actively investigated as next generation of magnetic resonance imaging contrast agents²⁸ and as carriers for targeted drug delivery²⁹, with a wide range of applications in the detection, diagnosis, and treatment of illnesses, such as cancer³⁰ and cardiovascular disease.³¹

The ability of nanoparticles to enhance proton relaxation of specific tissues and serve as magnetic resonance imaging contrast agents have been actively investigated mainly as T₂-contrast agents in the form of superparamagnetic iron oxides (SPIO) for over two decades, with applications such as liver/spleen imaging (i.e., Endorem[®] and Feridex IV[®]).³²⁻³⁶

A significant challenge associated with the application of these nanoparticles systems is their behavior *in vivo*. The efficacy of these systems is often compromised due to recognition and clearance by the reticuloendothelial system and by their non-ability of overcoming biological barriers. To increase the effectiveness of these nano-objects, several techniques are under study, including reducing the size or incorporating novel cores, coating materials and functional ligands to improve the detection and specific delivery of these nanoparticles.

I.2 SCOPE OF THE THESIS

Since contrast agents are used in magnetic resonance imaging (MRI), numerous efforts have been undertaken to increase their relaxivity (parameter allowing to quantify contrast agent efficiency). Few years ago, Merbach group developed the chelating agent DTTA ($H_4DTTA =$ diethylenetriaminetetraacetic acid = N,N' -[iminobis(ethane-2,1-diyl)]bis[N -(carboxymethyl)glycine]), which contains when complexed with gadolinium(III) in aqueous solution two inner-sphere coordination sites for water molecules. This chelate unit complexed with gadolinium(III) presents also a relatively fast inner-sphere water exchange rate which is favorable for the relaxivity.

Three compounds will be studied in this thesis, all of them containing the DTTA chelate unit.

The first, the smallest, is the methylated derivative $H_4DTTA-Me$ (N,N' -[(methylimino)bis(ethane-2,1-diyl)]bis[N -(carboxymethyl)glycine]). This compound, considered as the monomer, will allow studying the physicochemical properties of the DTTA chelating moiety.

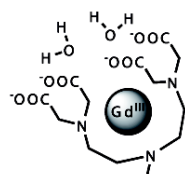


Figure I.2-1: $[Gd(DTTA-Me)(H_2O)_2]^-$

The second compound will be the Ru(II)-based metallostar $\text{Na}_4\{\text{Ru}[\text{Ln}_2\text{bpy-DTTA}_2(\text{H}_2\text{O})_4]_3\}$ ($\text{Ln} = \text{Y}, \text{Gd}, \text{and Eu}$), a close derivative to the metallostar compound $\text{Na}_4\{\text{Fe}[\text{Gd}_2\text{bpy-DTTA}_2(\text{H}_2\text{O})_4]_3\}^{4-}$. The challenge will be to synthesise this heptametallic self-assembled edifice and demonstrate whether it acts as potential bimodal (magnetic and luminescent) bioprobe.

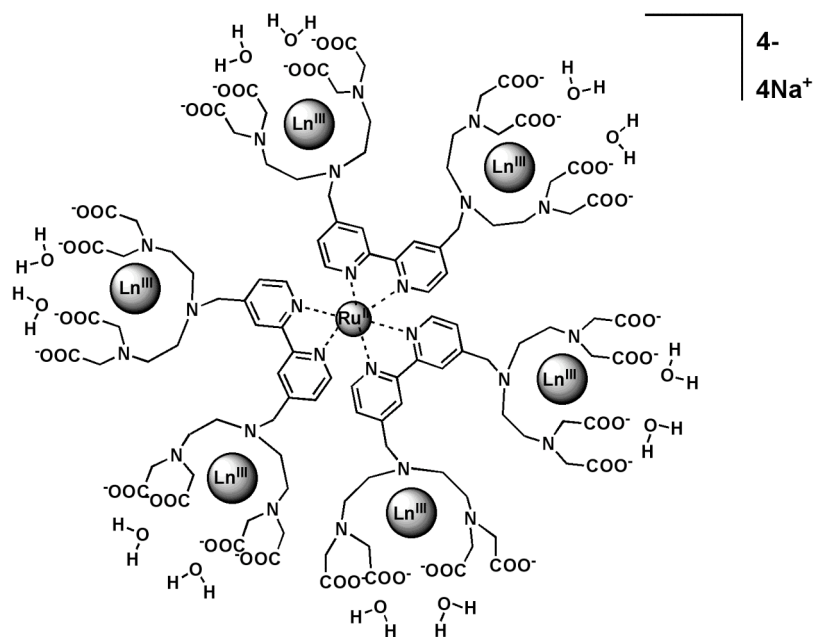


Figure I.2-2: $\{\text{Ru}[\text{Ln}_2\text{bpy-DTTA}_2(\text{H}_2\text{O})_4]_3\}^{4-}$

The third compound is represented by Gd-DTTA chelate units derivated with thiol function and linked to gold nanoparticles. The interesting rigidity of this system will probably show a high relaxivity due to a long rotational correlation time. Several publications report magnetic behaviour of small transition metal nanoparticles. We will try to establish if there is any contribution to the paramagnetic relaxation enhancement observed.

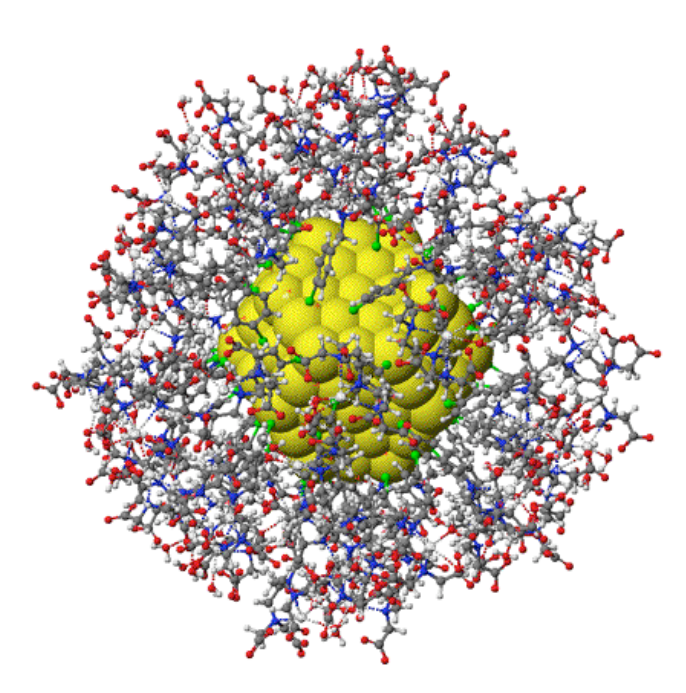


Figure I.2-3: Gold nanoparticle coated with Gd-DTTA thiol derivatives.

I.3 REFERENCES

1. *National High Magnetic Field Laboratory*, <http://www.magnet.fsu.edu/education/tutorials/magnetacademy/mri>.
2. *National Institute of Mental Health*, <http://rsb.info.nih.gov/ij/images/>.
3. A. E. Merbach and É. Tóth, in *The Chemistry of Contrast Agents in Medical Magnetic Resonance Imaging*, John Wiley & Sons, Chichester, 2001.
4. E. T. Clarke and A. E. Martell, *Inorg. Chim. Acta*, 1991, **190**, 37-46.
5. É. Tóth and E. Brücher, *Inorg. Chim. Acta*, 1994, **221**, 165-167.
6. S. Laurent, L. V. Elst and R. N. Muller, *Contrast Media Mol. Imaging*, 2006, **1**, 128-137.
7. E. Terreno, M. Botta, P. Boniforte, C. Bracco, L. Milone, B. Mondino, F. Uggeri and S. Aime, *Chem. Eur. J.*, 2005, **11**, 5531-5537.
8. P. M. May, P. W. Linder and D. R. Williams, *J. Chem. Soc., Dalton Trans.*, 1977, 588-595.
9. W. Cacheris, S. C. Quay and S. M. Rocklage, *Magnetic Resonance Imaging*, 1990, **8**, 467-481.
10. G. E. Jackson, S. Wynchank and M. Woudenberg, *Magnetic Resonance in Medicine*, 1990, **16**, 57-66.
11. J. Peters, J. Huskens and D. J. Raber, *Prog. Nucl. Magn. Reson. Spectrosc.*, 1996, **28**, 283-350.
12. D. F. Evans, *Journal of the Chemical Society*, 1959, 2003-2005.
13. I. Bertini, C. Luchinat and G. Parigi, *Solution NMR of Paramagnetic Molecules Applications to Metallobiomolecules and Models*, Current Methods in Inorganic Chemistry, 2001.
14. I. Solomon and N. Bloembergen, *J. Chem. Phys.*, 1956, **25**, 261-266.
15. V. Jacques and J. F. Desreux, *Top. Curr. Chem.*, 2002.
16. G. Lipari and A. Szabo, *J. Am. Chem. Soc.*, 1982, **104**, 4546-4559.
17. G. Lipari and A. Szabo, *J. Am. Chem. Soc.*, 1982, **104**, 4559-4570.
18. N. Bloembergen, *J. Chem. Phys.*, 1957, **27**, 572-573.
19. N. Bloembergen and L. O. Morgan, *J. Chem. Phys.*, 1961, **34**, 842-850.
20. S. Laus, A. Sour, R. Ruloff, É. Tóth and A. E. Merbach, *Chem. Eur. J.*, 2005, **11**, 3064-3076.
21. J. Costa, R. Ruloff, L. Burai, L. Helm and A. E. Merbach, *J. Am. Chem. Soc.*, 2005, **127**, 5147-5157.
22. J. Costa, E. Tóth, L. Helm and A. E. Merbach, *Inorg. Chem.*, 2005, **44**, 4747-4755.

23. P. Lebduková, A. Sour, L. Helm, E. Tóth, J. Kotek, I. Luke and A. Merbach, *J. Chem. Soc., Dalton Trans.*, 2006, 3399-3406.
24. J. B. Livramento, L. Helm, A. Sour, C. O'Neil, A. E. Merbach and E. Toth, *J. Chem. Soc., Dalton Trans.*, 2008, 1195-1202.
25. J. Kowalewski, D. Kruk and G. Parigi, *Adv. Inorg. Chem.*, 2006, **57**, 41-104.
26. I. Bertini, J. Kowalewski, C. Luchinat, T. Nilsson and G. Parigi, *J. Chem. Phys.*, 1999, **111**, 5795-5807.
27. D. Kruk, T. Nilsson and J. Kowalewski, *Phys. Chem. Chem. Phys.*, 2001, **3**, 4907-4917.
28. C. Sun, J. S. H. Lee and M. Zhang, *Adv. Drug Delivery Rev.*, 2008, **60**, 1252-1265.
29. J. Dobson, *Drug Dev. Res.*, 2006, **67**, 55-60.
30. M. Ferrari, *Nat. Rev. Cancer*, 2005, **5**, 161-171.
31. S. A. Wickline, A. M. Neubauer, P. M. Winter, S. D. Caruthers and G. M. Lanza, *Journal of Magnetic Resonance Imaging*, 2007, **25**, 667-680.
32. R. Weissleder, A. Bogdanov, E. A. Neuwelt and M. Papisov, *Adv. Drug Delivery Rev.*, 1995, **16**, 321-334.
33. Y. X. J. Wang, S. M. Hussain and G. P. Krestin, *European Radiology*, 2001, **11**, 2319-2331.
34. J. W. M. Bulte and D. L. Kraitchman, *NMR in Biomedicine*, 2004, **17**, 484-499.
35. K. C. Briley-Saebo, V. Mani, F. Hyafil, J. C. Cornily and Z. A. Fayad, *Magnetic Resonance in Medicine*, 2008, **59**, 721-730.
36. D. E. Sosnovik, M. Nahrendorf and R. Weissleder, *Basic Research in Cardiology*, 2008, **103**, 122-130.

CHAPTER II.

PHYSICOCHEMICAL

PROPERTIES OF THE HIGH FIELD MRI

RELEVANT $[\text{Gd}(\text{DTTA-ME})(\text{H}_2\text{O})_2]^-$

COMPLEX

TABLE OF CONTENTS CHAPTER II

II.1	INTRODUCTION	47
II.2	EXPERIMENTAL SECTION	49
II.2.1	SYNTHESIS OF $\text{H}_4\text{DTTA-ME}$	49
II.2.2	PROTONATION AND STABILITY CONSTANTS BY POTENTIOMETRIC MEASUREMENTS	50
II.2.3	DEUTERATION CONSTANTS BY $^1\text{H-NMR}$ MEASUREMENTS	50
II.2.4	CONDITIONAL RELATIVE STABILITY CONSTANT $K_{L1/L2}^*$ OF $[\text{Gd}(\text{DTTA-ME})(\text{H}_2\text{O})_2]^-$ RELATIVE TO $[\text{Gd}(\text{DTPA-BMA})(\text{H}_2\text{O})]$	51
II.2.5	TRANSMETALATION OF $[\text{Gd}(\text{DTTA-ME})(\text{H}_2\text{O})_2]^-$ WITH Zn^{2+}	51
II.2.6	SEARCH FOR TERNARY ADDUCT FORMATION BETWEEN $[\text{Gd}(\text{DTTA-ME})(\text{H}_2\text{O})_2]^-$ AND L- LACTATE	52
II.3	RESULTS AND DISCUSSION	53
II.3.1	POTENTIOMETRY	53
II.3.2	^1H NMR IN D_2O	58
II.3.3	STABILITY CONSTANTS BY POTENTIOMETRY	61
II.3.4	CONDITIONAL RELATIVE STABILITY CONSTANT $K_{L1/L2}^*$ OF $[\text{Gd}(\text{DTTA-ME})(\text{H}_2\text{O})_2]^-$ RELATIVE TO $[\text{Gd}(\text{DTPA-BMA})(\text{H}_2\text{O})]$	62
II.3.5	TRANSMETALATION OF $[\text{Gd}(\text{DTTA-ME})(\text{H}_2\text{O})_2]^-$ WITH Zn^{2+}	66
II.3.6	SEARCH FOR ADDUCT FORMATION BETWEEN $[\text{Gd}(\text{DTTA-ME})(\text{H}_2\text{O})_2]^-$ AND L-LACTATE	68
II.4	CONCLUSION	71
II.5	ACKNOWLEDGEMENTS	73
II.6	REFERENCES	74

II.1 INTRODUCTION

The use of paramagnetic gadolinium chelates as contrast agents for medical magnetic resonance imaging (MRI) has increased considerably during the last two decades. A great effort has been spent in the same time period to develop new compounds giving better contrast.¹⁻³ The parameters that can be tuned in order to obtain more efficient agents, meaning to increase water proton relaxivity, are the rotational tumbling time of the complex, the exchange rate of water molecules from the first coordination sphere of Gd^{3+} and the number of water molecules in the first sphere. A stringent condition for all new chelating ligands is that the complex formed with the gadolinium ion is thermodynamically stable and kinetically inert and therefore all commercial MRI contrast agents have only one water molecule in the first coordination sphere. The safety of gadolinium based contrast agents became an important issue since it has become the leading suspect for Nephrogenic Systemic Fibrosis (NSF), a disease with high morbidity and mortality.⁴⁻⁷ Besides the application in medical diagnostics, MRI contrast agents are also used in medical research and pharmacological studies. These studies in general performed *in vitro* or in animals, depend on the development of new agents delivering good contrast at high magnetic fields. Restrictions concerning high complex stability are however often less severe than in case of clinical use.

A common approach achieving high relaxivity is to load a rigid macromolecule like a dendrimer with many chelate units binding Gd^{3+} .⁸⁻¹¹ Relaxivities up to $\sim 30 \text{ mM}^{-1}\text{s}^{-1}$ (at 20 MHz) have been achieved in this way. The relaxivity values are, however, strongly magnetic-field-dependent and at fields of 3T and above, relaxivity drops rapidly even below those of small commercial contrast agents. In contrast to that field-dependent boost in efficiency, raising the number of inner-sphere water molecules leads to an increase in relaxivity, which is proportional to the number of water molecules and independent of the magnetic field. Therefore, several research groups devoted their efforts to the synthesis of chelates allowing the presence of more than one water molecule in the first coordination sphere of the metal.¹²⁻¹⁵

Because the stability of the chelate complexes is a major concern, macrocyclic ligands based on the DO3A unit have often been chosen.¹⁶⁻²⁰ Gadolinium complexes of these ligands are thermodynamically and kinetically relatively stable²¹ and have two inner-sphere water molecules. However, it has been found that these compounds can form ternary complexes

with anionic metabolites present in serum.^{18, 20, 22} Bidentate anions like lactate or carbonate bind directly to the paramagnetic center and replace the two inner-sphere water molecules. As a consequence, the relaxivity drops by about 60%, leading, on one hand, to a loss in efficiency as a contrast agent, but allowing, on the other hand, eventually monitoring in the presence of such anions.

Our group recently developed small to medium sized molecules binding two to six Gd^{3+} ions with heptadentate acyclic DTTA chelating groups (H_4DTTA = diethylenetriaminetetraacetic acid = N,N' -[iminobis(ethane-2,1-diyl)]bis[N -(carboxymethyl)glycine]).²³⁻²⁷ In these complexes, each Gd^{3+} binds two water molecules that exchange relatively rapidly with the bulk, leading to moderately high relaxivities. Interestingly, relaxivities at magnetic fields of 3 T and above are still relatively high, leading to better contrast than of commercial contrast agents.²⁵ Measurements of stability constants on complexes with DTTA^{4-} showed that complex stability constants, K_{ML} , vary strongly depending on the group bound to the central nitrogen.²⁶

In this chapter, we present a study of complexes with DTTA-Me^{4-} ($\text{H}_4\text{DTTA-Me}$ = N,N' -[(methylimino)bis(ethane-2,1-diyl)]bis[N -(carboxymethyl)glycine]) which mimics the DTTA chelating unit linked by a methylene group to organic backbones. Already in 1957, Schwarzenbach et al. presented protonation constants, K_i , and complex stability constants, K_{ML} , for some divalent ion complexes of the DTTA-Me^{4-} ligand.²⁸ Here we report the protonation and stability constants of DTTA-Me^{4-} and its Gd^{3+} ($\text{Na}[\text{Gd}(\text{DTTA-Me})(\text{H}_2\text{O})_2]^-$ = sodium{[N,N' -[(methylimino- κN)bis(ethane-2,1-diyl)]bis[N -(carboxy- κO)methyl]glycinato- $\kappa\text{N},-\kappa\text{O}$]](4-)}gadolinite(1-)) and Zn^{2+} complexes, respectively, determined by potentiometry and ^1H NMR pH titrations. NMR relaxometry is used to determine the conditional relative stability constant, $K_{L1/L2}^*$, of $[\text{Gd}(\text{DTTA-Me})(\text{H}_2\text{O})_2]^-$ with respect to the commercial contrast agent Omniscan[®] [$(\text{Gd}(\text{DTPA-BMA})(\text{H}_2\text{O}))$], to measure transmetalation towards endogenous Zn^{2+} ions and to assess a possible formation of ternary complexes with the bidentate ligand L-lactate.

II.2 EXPERIMENTAL SECTION

II.2.1 Synthesis of H₄DTTA-Me

All commercial reagents were used as received unless otherwise noted.

***N,N'*-[(methylimino)bis(ethane-2,1-diyl)]bis[*N*-(carboxymethyl)glycine]tetrakis(1,1-dimethylethyl) ester**

N-methyl-2-2' diaminodiethylamine (1.0 g) was dissolved in 24 ml dry DMF in the presence of 4.1 equivalents of K₂CO₃ (4.84 g). A total of 4.1 equiv of *tert*-butyl bromoacetate (6.8 g) was added dropwise. The solution was stirred overnight at room temperature under argon atmosphere. The solvent was evaporated, and water and dichloromethane (60 mL and 40 mL, respectively) were added to the residue. The crude product was extracted three times with dichloromethane (40 mL). The combined organic phases were dried with sodium sulphate, filtered and evaporated. The product was purified by silica gel chromatography (eluant 1:3 ethyl acetate / hexane), and 1.3 g of *N,N'*-[(methylimino)bis(ethane-2,1-diyl)]bis[*N*-(carboxymethyl)glycine]tetrakis(1,1-dimethylethyl) ester (yellow oil) were obtained (yield 27 %). ¹H NMR, 400 MHz, CDCl₃, δ in ppm : 1.45 (s, 36 H); 2.24 (s, 3 H); 2.52 (m, 4 H); 2.83 (m, 4 H); 3.45 (s, 8 H). MS (ESI): m/z: 574 [MH]⁺.

***N,N'*-[(methylimino)bis(ethane-2,1-diyl)]bis[*N*-(carboxymethyl)glycine]**

The intermediate *N,N'*-[(methylimino)bis(ethane-2,1-diyl)]bis[*N*-(carboxymethyl)glycine] tetrakis(1,1-dimethylethyl) ester was deprotected by stirring overnight in 150 mL of boiling 6 M HCl. After evaporation, the crude product was washed three times in water by dissolution and evaporation and then purified by ion-exchange chromatography on Bio-Rad AG 50W-8X resin eluted with a gradient of HCl (1-5 M) and then aqueous NH₃. The pure fractions were evaporated and washed three times with water; the resulting white solid *N,N'*-[(methylimino)bis(ethane-2,1-diyl)]bis[*N*-(carboxymethyl)glycine] was dried under vacuum (yield 50 %). ¹H NMR (400 MHz, D₂O, δ in ppm at pH ~ 2): 2.98 (s, 3 H); 3.45 (m, 4 H);

3.50 (m, 4 H); 3.88 (s, 8 H). MS (ESI): m/z : 350 $[\text{MH}]^+$. Elem anal. Calcd for $\text{H}_4\text{DTTA-Me}(\text{HCl})_3(\text{H}_2\text{O})_4$: C, 29.41; H, 6.21; N, 7.91. Found: C, 29.56; H, 5.85; N, 7.65.

II.2.2 Protonation and Stability Constants by Potentiometric Measurements

Stock solutions of GdCl_3 (97.7 mM) and ZnCl_2 (89.5 mM) were prepared with double-distilled water, and standardized by titration with $\text{Na}_2\text{H}_2\text{EDTA}$ solution in urotropine buffer at pH 5.8 using xylenol orange as the indicator. A stock solution of the ligand $\text{H}_4\text{DTTA-Me}$ (13.4 mM) was prepared and titrated with $\text{Na}_2\text{H}_2\text{EDTA}$ solution in a urotropin buffer at pH 5.8 using xylenol orange as the indicator in the presence of an excess of Gd^{3+} . The concentration of the ligand solution was confirmed by potentiometry on the basis of titration curves obtained in the absence and in the presence of a 50-fold excess of CaCl_2 .

The protonation constants of the ligand DTTA-Me^{4-} and the stability constants of its complexes with Gd^{3+} and Zn^{2+} ($C_L = 3$ mM, $C_M = 3$ mM; $I = 0.1$ M KCl, titrated with 50 mM KOH) were determined by pH potentiometric titrations. The titrations were carried out using 3 mL sample volumes in a thermostatted glass-jacketed vessel ($25 \pm 0.2^\circ\text{C}$) with a magnetic stirrer (under a dinitrogen atmosphere to avoid the effects of CO_2) and dosed with a Metrohm Dosimat 665 automatic burette. A combined glass electrode (C14/02-SC, reference electrode Ag/AgCl in 3 M KCl, Moeller Scientific Glass Instruments, Switzerland) connected to a Metrohm 692 pH/ion meter was used to measure the pH. The hydrogen ion concentration was calculated from the measured pH values by using a correction term, obtained as the difference between the measured and calculated pH values in a titration of HCl (0.1 M) with standardized KOH, as suggested by Irving et al.²⁹ The potentiometric data (about 160 points collected over the pH range 2-12) were refined with the *Hyperquad 2000* program.^{30,31}

II.2.3 Deuteration Constants by $^1\text{H-NMR}$ Measurements

An aqueous stock solution of $\text{H}_4\text{DTTA-Me}$ (3 mM) was prepared in D_2O (99.8%), with $I = 0.1$ M NaCl. DCl or NaOD solutions were added to 5 mL of this solution, placed into a glass-jacketed vessel ($25 \pm 0.2^\circ\text{C}$) with a magnetic stirrer (in an N_2 atmosphere to avoid the effects of CO_2). The pH was measured as described above. For NMR titration ~ 400 μL of the solution were placed into a 5 mm NMR tube and ^1H NMR spectra were recorded on a Bruker

Avance-400 (25 ± 0.2 °C, measured by a substitution technique³²). After the NMR measurement, the solution was poured back to the thermostatted vessel. The chemical shifts were recorded using *tert*-butyl alcohol as an internal standard (1.24 ppm). The chemical shift data (about 40 points collected over the pD range 2-12) were refined with the Visualiseur/Optimiseur programs running on a Matlab platform.³³

II.2.4 Conditional Relative Stability Constant $K_{L1/L2}^*$ of $[\text{Gd}(\text{DTTA-Me})(\text{H}_2\text{O})_2]^-$ Relative to $[\text{Gd}(\text{DTPA-BMA})(\text{H}_2\text{O})]$

The $\text{H}_3\text{DTPA-BMA}$ was synthesized according to a procedure described by Geraldes et al.³⁴ Aqueous solutions of the complexes $[\text{Gd}(\text{DTTA-Me})(\text{H}_2\text{O})_2]^-$ (**sol L₁**) and $[(\text{Gd}(\text{DTPA-BMA})(\text{H}_2\text{O}))]$ (**sol L₂**), each containing a 3-fold excess of ligand, were prepared, and the pH was set to 8.4 (**sol L₁**: 4 mM GdCl_3 and 12 mM $\text{H}_4\text{DTTA-Me}$ and **sol L₂**: 4 mM GdCl_3 and 12 mM $\text{H}_3\text{DTPA-BMA}$). Seven samples ($m = 1 - 7$) containing 1.40 mL of different amounts of **sol L₁** and **sol L₂** (0, 16, 33, 50, 67, 84 and 100 % of **sol L₂**) were prepared in 2 mL flasks. Through the addition of ~0.60 mL (exactly weighted) of water containing NaCl, final concentrations for each sample were $C^{\text{Gd}} = 3$ mM, $C_m^{\text{L}_1} + C_m^{\text{L}_2} = 9$ mM, and $I = 0.1$ M NaCl. Measurements of the water proton longitudinal relaxation rates, $R_1 = 1/T_1$, were performed on a Bruker Minispec mq60 (60 MHz) at 25 ± 0.2 °C (measured by a substitution technique³²). NMR tubes were left 15 min inside the thermostated probe before measurement. Relaxivities and pHs of the samples were checked two weeks later to confirm that systems had reached the equilibrium.

II.2.5 Transmetallation of $[\text{Gd}(\text{DTTA-Me})(\text{H}_2\text{O})_2]^-$ with Zn^{2+}

Transmetalation reactions with Zn^{2+} were studied as described by Laurent et al.³⁵ Equimolar amounts of ZnCl_2 were added to $[\text{Gd}(\text{DTTA-Me})(\text{H}_2\text{O})_2]^-$ and to $[(\text{Gd}(\text{DTPA-BMA})(\text{H}_2\text{O}))]$ solutions (2.5 mM each) containing a phosphate buffer (pH 7, $[\text{KH}_2\text{PO}_4] = 26$ mM, $[\text{Na}_2\text{HPO}_4] = 41$ mM). The samples were vigorously stirred and the water proton longitudinal relaxation rates measured on a Bruker Minispec mq60 (60 MHz, 37 °C). The measurements were carried out over 3 days using an automatic measurement routine.

II.2.6 Search for Ternary Adduct Formation between $[\text{Gd}(\text{DTTA-Me})(\text{H}_2\text{O})_2]^-$ and L-Lactate

Formation of ternary adducts can be studied by measuring the water proton relaxivity.²⁰ Solutions of 1 mM $[\text{Gd}(\text{DTTA-Me})(\text{H}_2\text{O})_2]^-$ containing increasing amounts of lactate (0, 0.24, 0.97, 1.49, 1.95, 7.57, 12.2, 20.1, 30.3, 40.1, and 50.0 mM), were prepared at pH 7.0. Measurements of the water proton longitudinal relaxation rates, R_1 , were performed with a Stellar fast-field cycling relaxometer at 10 MHz and 25 ± 0.2 °C (measured by a substitution technique³²).

II.3 RESULTS AND DISCUSSION

II.3.1 Potentiometry

Protonation constants of DTTA-Me⁴⁻ were determined by potentiometry. From literature data on acyclic poly(aminocarboxylate) molecules, four protonation can be expected over the the pH range 2 to 12 for DTTA-Me⁴⁻. The stepwise protonation constants K_i (eq. II.3-1) were obtained by fitting of the potentiometric data (Figure II.3-1).

$$K_i = \frac{[H_i L]}{[H_{i-1} L][H^+]} \text{ with } i > 0 \quad \text{II.3-1}$$

An analysis of the potentiometric data using five protonation constants has been performed because of a significant improvement of the quality of fit. The protonation constant for the first protonation step, K_1 , of DTTA-Me⁴⁻ is similar to that of DTPA⁴⁻ and TTAHA⁶⁻. However, the ligand tpy-DTTA⁴⁻ (Figure II.3-2) has a K_1 , which is about two orders of magnitude lower.^{23, 24} These results suggest that for all of these ligands the first protonation occurs on the central nitrogen. The loss of basicity of the central nitrogen for tpy-DTTA⁴⁻ with respect to DTTA-Me⁴⁻, DTPA⁴⁻, and TTAHA⁶⁻ is a consequence of the direct binding of the terpyridine moiety to the central nitrogen instead of a methylene group. Costa et al.^{23, 24} investigated ligands where two DTTA chelators are linked in para and meta positions to a xylene core via a methylene group. The first protonation constants for pX(DTTA)₂⁸⁻ and mX(DTTA)₂⁸⁻ (Table II.3-1) are intermediate between the values of TTAHA⁶⁻, DTPA⁵⁻, and DTTA-Me⁴⁻, and that of tpy-DTTA⁴⁻. In this case, the methylene group is intercalated between the aromatic ring and the polyaminocarboxylate and quenches partially inductive or mesomeric effects, affecting the protonation constants of the DTTA entities. The decrease from log K_4 to log K_5 is larger for DTTA-Me⁴⁻ than expected by a statistical approach (0.3). The protonation constant log K_6 for DTTA-Me⁴⁻ could not be determined because it occurs below pH 2.

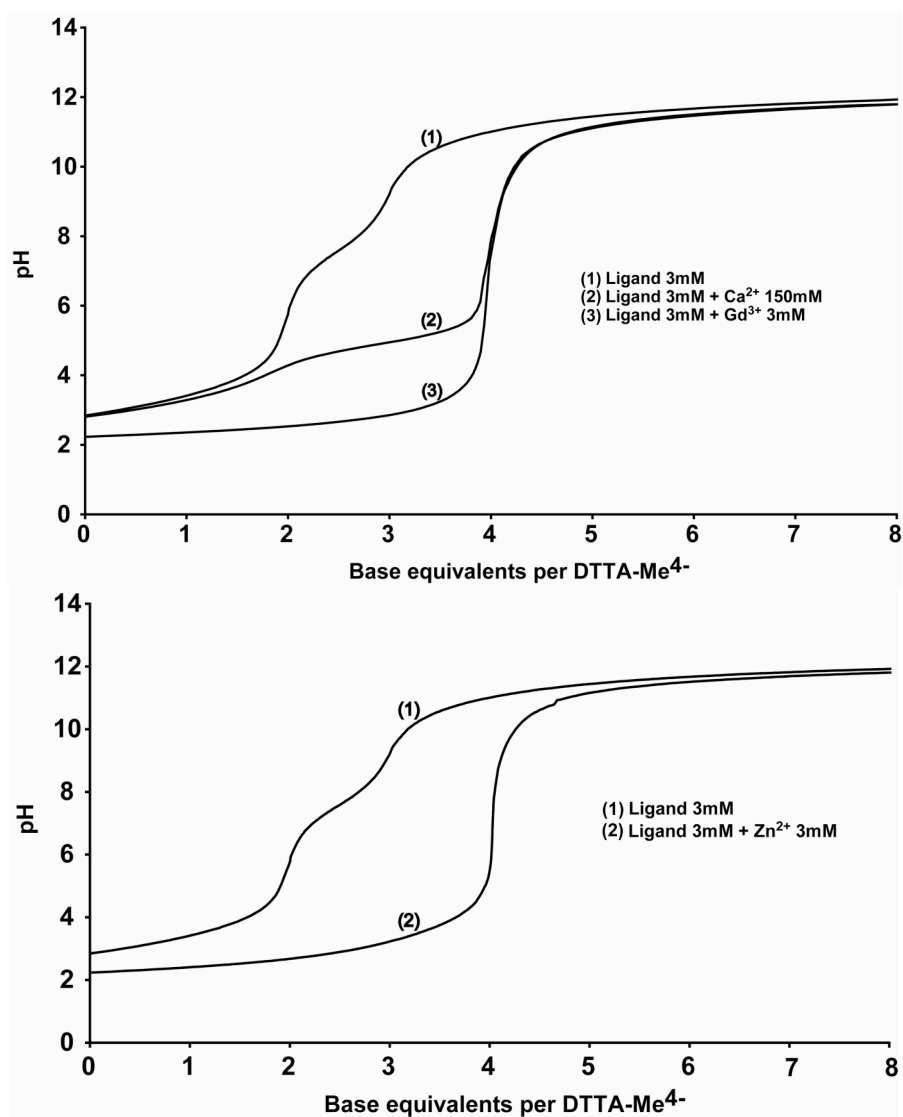


Figure II.3-1. Titration curves at 25 °C and $I=0.1$ M KCl of the DTTA-Me⁴⁻ ligand and its Ca²⁺, Zn²⁺, and Gd³⁺ complexes.

Table II.3-1: Thermodynamic Protonation and Stability Constants for Various Ligands and Their Gd^{3+} and Zn^{2+} complexes (T = 25°C, I = 0.1 M)

Ligand	DTTA-Me ⁴⁻ ^a	bpy(DTTA) _b ⁸⁻	p,mX(DTTA) ₂ ⁸⁻ ^c		tpy-DTTA ⁴⁻ _d	TTAHA ⁶⁻ ^e	DTPA ⁵⁻ ^f	EDTA ⁴⁻	DTPA-BMA ³⁻ ^g
			para	meta					
log K ₁	10.75 (0.03) ^h	9.87 ⁱ	9.84	9.45	8.65	10.66	10.41	10.08 ^j	9.37
log K ₂	7.56 (0.03) ^h	9.16 ⁱ	8.80	8.12	7.63	8.56	8.37	6.42 ^j	4.38
log K ₃	3.76 (0.05) ^h	3.09 ⁱ	3.52	3.97	5.25	8.38	4.09	3.11 ^j	3.31
log K ₄	2.74 (0.05) ^h	1.5 ⁱ	2.40	2.70	3.30	2.92	2.51	2.33 ^j	1.43
log K ₅	1.90 (0.15)	-	-	-	-	2.39	2.04	-	-
log K ₆	-	-	-	-	-	2.0	-	-	-
log K _{GdL}	18.60 (0.10)	18.2	19.1	17.0	10.87	19.0	22.5	17.7 ^j	16.85
log K _{GdHL}	2.12 (0.24)	-	2.1	3.2	3.73	8.3	1.8	-	-
log K _{ZnL}	17.69 (0.10)	18.0	17.94	16.19	-	18.91	18.29	16.4 ^k	12.04
log K _{ZnHL}	3.73 (0.10)	3.4	3.76	4.24	-	8.01	5.6	-	4.04
log K _{ZnH2L}	-	-	-	-	-	3.68	-	-	-
pGd ^l	15.8 (0.1)	14.9	16.2	15.1	10.6	15.5	19.2	15.9	15.8

^a I = 0.1M KCl; this work; numbers in parentheses correspond to two times standard deviation. ^b I = 0.1 M (CH₃)₄NCl; from ref [26]; ^c I = 0.1 M (CH₃)₄NCl; from ref [23]. ^d I = 0.1 M KCl; from ref [24]. ^e I = 0.1 M KCl; from ref [36] ^f I = 0.1 M KCl; from ref [37]. ^g I = 0.1 M KCl; from ref [38]. ^h from Ref [28] at T = 20°C, I = 0.1 M KCl: log K₁ = 10.89, log K₂ = 7.39, log K₃ = 3.65, log K₄ = 2.8.. ⁱ Protonation constants of the poly(aminocarboxylate) moiety. ^j I = 0.1 M KCl; from ref [39]. ^k From r [40]. ^l pM values of GdL complexes under physiologically relevant conditions (pH 7.4; [Gd]_{total} = 1 μM; [L]_{total} = 10 μM)

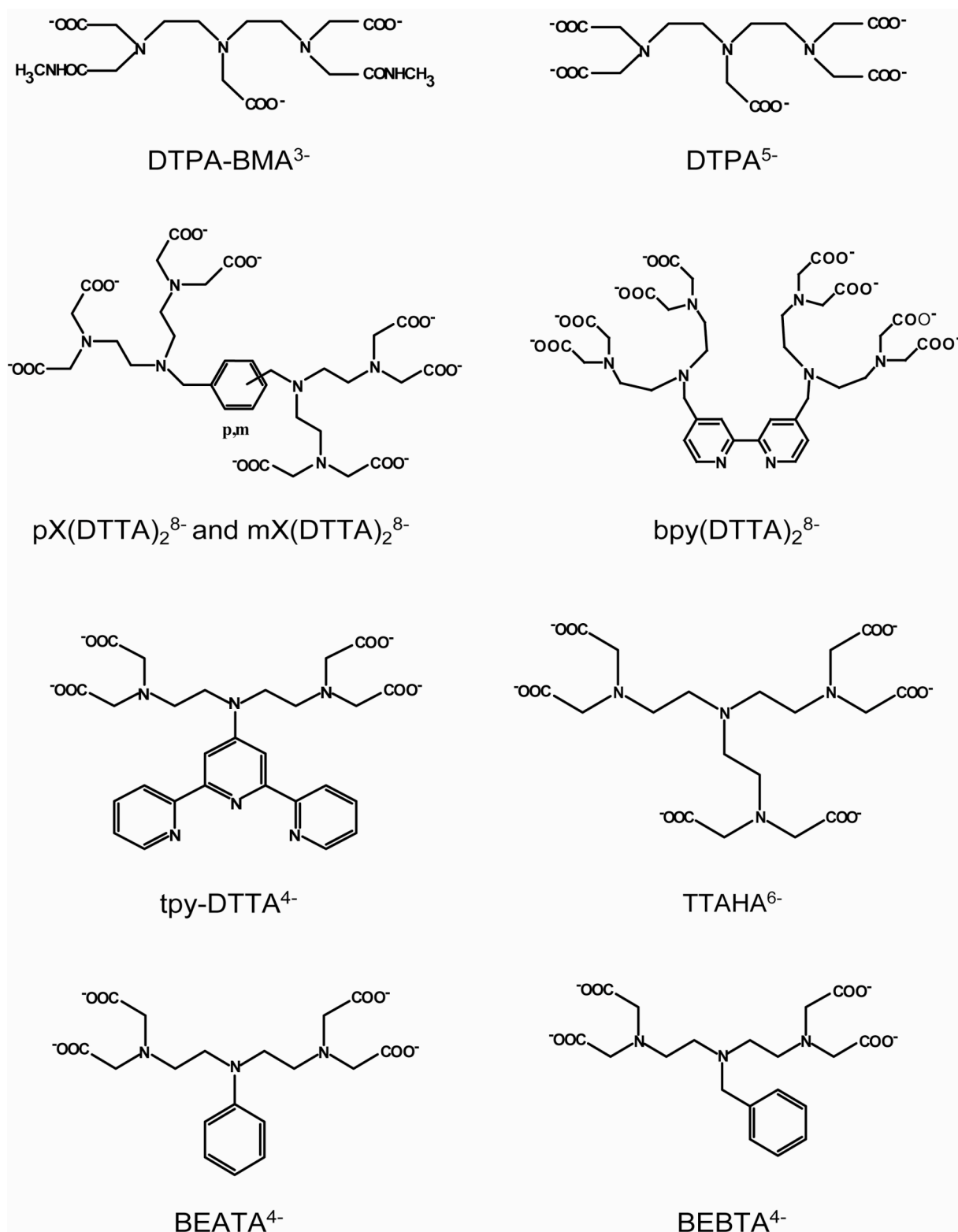


Figure II.3-2. Ligands containing DTTA chelating units.

II.3.2 ¹H NMR in D₂O

¹H NMR chemical shifts of DTTA-Me⁴⁻ were assigned on the basis of signal multiplicities. Samples were prepared in D₂O and pD values have been obtained from the equation pD = pH_{apparent} + 0.44,³⁶ where pH_{apparent} is the measured pH of the sample. The pD dependences of the chemical shifts, $\delta_X^{obs}(D^+)$, of the doublets d1 and d2 and the singlets s1 and s2 (Figure II.3-3) due to successive deuteration of DTTA-Me⁴⁻ can be expressed as in eq II.2:

$$\delta_X^{obs}(D^+) = \sum_{i=0}^5 P_i \cdot \delta_X^{D_i L^{i-4}} \quad \text{II.3-2}$$

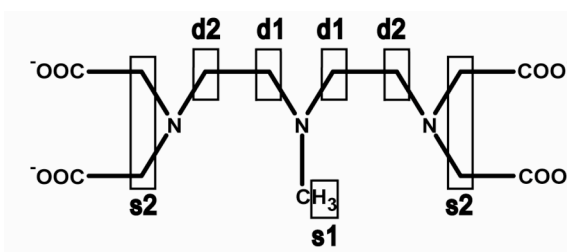


Figure II.3-3: DTTA-Me⁴⁻ ligand.

where $\delta_X^{D_i L^{i-4}}$ are the intrinsic chemical shifts of the protons X (X = s1, s2, d1 or d2) of the $D_i L^{i-4}$ species (i = 0 - 5) and P_i are the fractional populations of species L⁴⁻, DL³⁻, D₂L²⁻, D₃L⁻, D₄L and D₅L⁺, respectively:

$$P_i(D^+) = \frac{[D_i L^{i-4}]}{L_{Total}} = \beta_i^D \cdot P_0 \cdot [D^+]^i \quad \text{with} \quad \beta_i^D = \frac{[D_i L^{i-4}]}{[L^{4-}][D^+]^i} \quad \text{II.3-3}$$

L_{Total} is the total concentration of the ligand L, β_i^D are the cumulative deuteration constants, $[D^+]$ is the deuteron concentration in mol/L calculated as 10^{-pD}, and P_0 , the fractional population of species L⁴⁻, is given by eq II.4:

$$P_0 = \frac{1}{1 + \sum_{i=1}^5 \beta_i^D [D^+]^i} \quad \text{II.3-4}$$

The stepwise deuteration constants K_i^D are expressed following eq II.5:

$$K_i^D = \frac{\beta_i^D}{\beta_{i-1}^D} \quad \text{II.3-5}$$

The $\log K_i^D$ values of DTTA-Me⁴⁻ in D₂O were calculated from least-squares refinement of the chemical shifts measured as a function of pD (eq II.3-5). The deuteration constants found, $\log K_1^D = 11.40$, $\log K_2^D = 8.10$, $\log K_3^D = 4.10$, $\log K_4^D = 3.54$ and $\log K_5^D = 2.53$, are higher than those obtained in H₂O by potentiometry because the deuteron interacts more strongly with oxygen and nitrogen atoms than the proton does. Corrected $\log K_i^H$ values were calculated from $\log K_i^D$ according to $\log K_i^D = 0.32 + 1.044 \cdot \log K_i^H$ ^{37, 38}: $\log K_1^H = 10.61$, $\log K_2^H = 7.45$, $\log K_3^H = 3.62$, $\log K_4^H = 3.09$ and $\log K_5^H = 2.12$. Taking into account that $\text{pH}_{\text{apparent}}$ had to be converted to pD and that an empirical correction has been used to calculate $\log K_i^H$, the protonation constants as obtained from the deuteration constants are in good accordance with potentiometric values (Table II.3-1).

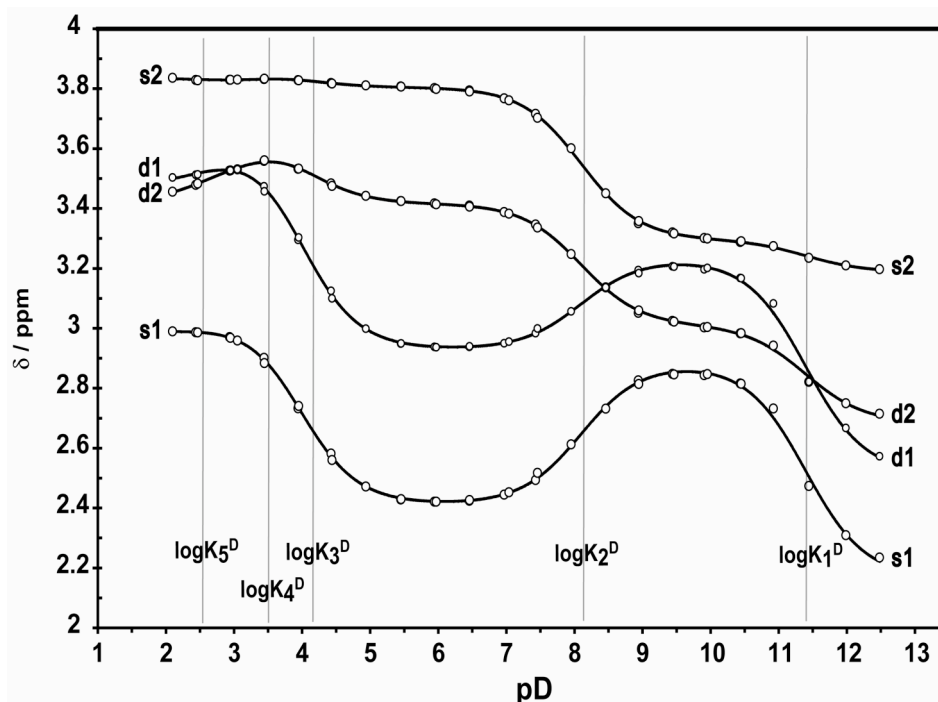


Figure II.3-4: ^1H NMR (400 MHz) DTTA-Me $^{4-}$ chemical shifts versus pD in D_2O at room temperature and $I=0.1$ M KCl. Lines were calculated using the fit parameters from eq 2 to eq 6 describing the first five deuteration steps of DTTA-Me $^{4-}$.

The microscopic titration scheme obtained by ^1H NMR spectroscopy is indicative of the deuteration sites. The deuteration of a basic site leads to a deshielding of adjacent protons.

Following Figure II.3-1, by lowering pD the protons d1 and s1 become first strongly deshielded while d2 and s2 are much less affected. It is, therefore, concluded that the first deuteration step, described by K_1 , occurs mainly on the central nitrogen. Between pD 9.5 and pD ~ 6 , protons d1 and s1 become again more shielded and protons d2 and s2 become deshielded. In the second deuteration step, both terminal nitrogen atoms are deuterated and the deuterium on the central nitrogen is released. The bisdeuterated ligand undergoes stabilization by the formation of five-membered rings due to hydrogen-bond formation between the proton on the terminal nitrogen and an oxygen atom of the carboxylate group, lowering strongly the $\log K_3^{\text{D}}$ value. A similar behavior has been already found by ^1H NMR titration on DTPA $^{5-}$ and EPTPA.³⁹⁻⁴¹

The three subsequent $\log K_i^{\text{D}}$ values, corresponding to a repeated deuteration of central nitrogen ($\log K_3^{\text{D}}$), and the deuteration of the first and second carboxylate ($\log K_4^{\text{D}}$

and $\log K_5^{\text{D}}$), are confirmed by the chemical shift changes of the d1/s1, and d2/s2 protons, respectively.

II.3.3 Stability Constants by Potentiometry

The thermodynamic stability of a metal M with charge m complexed to a chelate L with charge n is given by the stability constant K_{ML} (eq II.3-6):

$$K_{ML} = \frac{[ML^{m+n}]}{[M^m][L^n]} \quad \text{II.3-6}$$

$[M^m]$, $[L^n]$ and $[ML^{m+n}]$ are the equilibrium concentrations of the metal ion, the deprotonated ligand and the complex, respectively. At low pH, protonation of the complexes occurs, which is characterized by the complex protonation constants K_{MH_iL} (eq II.3-7):

$$K_{MH_iL} = \frac{[MH_iL^{m+n+i}]}{[MH_{i-1}L^{m+n+i-1}][H^+]} \quad \text{for } i = 1, 2, \dots \quad \text{II.3-7}$$

The stability constants K_{ML} and K_{MHL} of the complexes $[\text{M}^m(\text{DTTA-Me})]^{m-4}$ ($\text{M}^m = \text{Gd}^{3+}$, Zn^{2+}) were obtained by fitting potentiometric data measured over the pH range 2-12 (Figure II.3-1). The thermodynamic stability of $[\text{Gd}(\text{DTTA-Me})(\text{H}_2\text{O})_2]^-$ (Table II.3-1) is comparable to those of $[\text{Gd}(\text{TTAHA})(\text{H}_2\text{O})_2]^{3-}$, $[\text{Gd}_2(\text{pX}(\text{DTTA})_2)(\text{H}_2\text{O})_4]^{4-}$ and $[\text{Gd}_2(\text{mX}(\text{DTTA})_2)(\text{H}_2\text{O})_4]^{4-}$. All of these compounds bind the metal via a heptadentate DTTA^{4-} unit with a methylene group on the central nitrogen. Replacing this nonionic methylene group by a metal binding acetate group results in an increase of the stability constant by 3 - 4 orders of magnitude, as was found for the octadentate DTPA^{5-} (Table II.3-1). Replacing the methylene group on the central nitrogen by a tpy group leads, however, to a decrease in K_{GdL} of nearly eight orders of magnitude. Tse and Powell observed a much

smaller decrease of $\log K_{\text{GdL}}$ from 17.50 to 15.42 on going from to BEBTA^{4-} to BEATA^{4-} (Table II.3-1) where an electron-withdrawing phenyl group is replaced by an electron-donating benzyl.⁴²

The pGd value (eq II.8), usually calculated for $\text{pH } 7.4$, $[\text{Gd}]_{\text{total}} = [\text{ML}] = 1 \mu\text{M}$, and $[\text{L}]_{\text{total}} = 10 \mu\text{M}$,⁴³ expresses the influence of the ligand H_iL basicity and the protonation of the complex. A higher pGd value means higher complex stability under these conditions, with α_L (eq II.3-9) being the inverse of the $[L^{4-}]$ population fraction for an H_5L ligand.

$$\text{pGd} = -\log [\text{Gd}^{3+}]_{\text{free}} = -\log \frac{[\text{ML}]}{K_{\text{ML}} \cdot [\text{L}^{4-}]} = -\log \frac{[\text{Gd}]_{\text{total}} \cdot \alpha_L}{K_{\text{ML}} \cdot ([\text{L}]_{\text{total}} - [\text{Gd}]_{\text{total}})} \quad \text{II.3-8}$$

$$\alpha_L = \frac{[\text{L}]_{\text{total}}}{[\text{L}^{4-}]} = 1 + \sum_{i=1}^5 \beta_i [\text{H}^+]^i \quad \text{II.3-9}$$

Table II.3-1 shows pGd values for several poly(aminocarboxylate) Gd^{3+} complexes. The pGd of $[\text{Gd}(\text{DTTA-Me})(\text{H}_2\text{O})_2]^-$ ($\text{pGd} = 15.8$) is much smaller than for DTPA or DOTA ($\text{pGd} = 19.2$) complexes, but it is about the same as for the DTPA-BMA and for the EDTA complexes.

II.3.4 Conditional Relative Stability Constant $K_{L1/L2}^*$ of $[\text{Gd}(\text{DTTA-Me})(\text{H}_2\text{O})_2]^-$ Relative to $[\text{Gd}(\text{DTPA-BMA})(\text{H}_2\text{O})]$

The conditional relative stability constant $K_{L1/L2}^*$ (eq II.3-10) is defined by the ratio between the two conditional stability constants $K_{\text{GdL}_1}^*$ and $K_{\text{GdL}_2}^*$ of the Gd^{3+} complexes $[\text{Gd}(\text{DTTA-Me})(\text{H}_2\text{O})_2]^-$ and $[\text{Gd}(\text{DTPA-BMA})(\text{H}_2\text{O})]$, respectively. These two constants, depending on pH , are equal to their corresponding thermodynamic stability constants K_{GdL_1} and K_{GdL_2} divided by the inverse of their non protonated ligand fractions α_{L1} and α_{L2} , respectively (eq II.10).

$$K_{L1/L2}^* = \frac{K_{GdL_1}^*}{K_{GdL_2}^*} = \frac{\alpha_{L_2} \cdot K_{GdL_1}}{\alpha_{L_1} \cdot K_{GdL_2}} = \frac{\alpha_{L_2}}{\alpha_{L_1}} \cdot K_{L1/L2} \quad \text{II.3-10}$$

$$\text{with } \alpha_{L_1} = 1 + \sum_{i=1}^5 \beta_i(L_1)[H^+]^i \text{ and } \alpha_{L_2} = 1 + \sum_{i=1}^4 \beta_i(L_2)[H^+]^i$$

The conditional relative stability constant $K_{L1/L2}^*$ of gadolinium complexes can be measured via ^1H relaxivity measurements provided the relaxivities of the two complexes, $r_1^{GdL_1}$ and $r_1^{GdL_2}$, are sufficiently different. The relaxivity of a paramagnetic compound in aqueous solution is commonly expressed by eq II.3-11: ⁴⁴

$$r_1 = \left(\frac{1}{T_1} - \frac{1}{T_{1,H_2O}} \right) \cdot \frac{1}{c_{Gd^{3+}}} \left[s^{-1} m M^{-1} \right] \quad \text{II.3-11}$$

$1/T_1$ and $1/T_{1,H_2O}$ are the measured longitudinal relaxation rates of water protons of solutions $C_m^{L_2}$ with and without the paramagnetic ion, respectively. The relaxivity, r_1^m , of a sample composed of a mixture of **sol L₁** and **sol L₂** (see Chapter II.2) is given by the relative concentrations $[\text{GdL}_1]$ and $[\text{GdL}_2]$ at equilibrium in respect to the total concentration of gadolinium in the mixture, C_m^{Gd} (eq II.3-12):

$$r_1^m = r_1^{GdL_1} \left(1 - \frac{[\text{GdL}_2]}{C_m^{Gd}} \right) + r_1^{GdL_2} \left(\frac{[\text{GdL}_2]}{C_m^{Gd}} \right) \quad \text{II.3-12}$$

If the total concentrations of the two ligands in the mixture $C_m^{L_1}$ and $C_m^{L_2}$ are known, the conditional relative stability constant $K_{L1/L2}^*$ can be calculated with eq II.13 (see Chapter IV.1.3):

$$K_{L1/L2}^* = \frac{\left(\frac{r_1^m - r_1^{GdL_2}}{r_1^{GdL_1} - r_1^{GdL_2}} \right) \left(\frac{C_m^{L_2}}{C_m^{Gd}} - 1 + \left(\frac{r_1^m - r_1^{GdL_2}}{r_1^{GdL_1} - r_1^{GdL_2}} \right) \right)}{\left(1 - \left(\frac{r_1^m - r_1^{GdL_2}}{r_1^{GdL_1} - r_1^{GdL_2}} \right) \right) \left(\frac{C_m^{L_1}}{C_m^{Gd}} - \left(\frac{r_1^m - r_1^{GdL_2}}{r_1^{GdL_1} - r_1^{GdL_2}} \right) \right)} \quad \text{II.3-13}$$

From the compositions of the individual samples we can calculate relaxivities using $K_{L1/L2}^*$, $r_1^{\text{GdL}_1}$ and $r_1^{\text{GdL}_2}$ as parameters (see Chapter Appendix, scheme VI.1.2-1). Experimental data can be fitted by this function yielding the conditional relative stability constant $K_{L1/L2}^* = 6.4 \pm 0.3$ at pH = 8.3 and 25 °C (Figure II.3-5). At that pH, both ligands exist mainly in the monoprotonated form in solution and the $[\text{H}^+]$ concentration is not altered by the establishment of the equilibrium as defined in eq II.3-14.

II.3-14

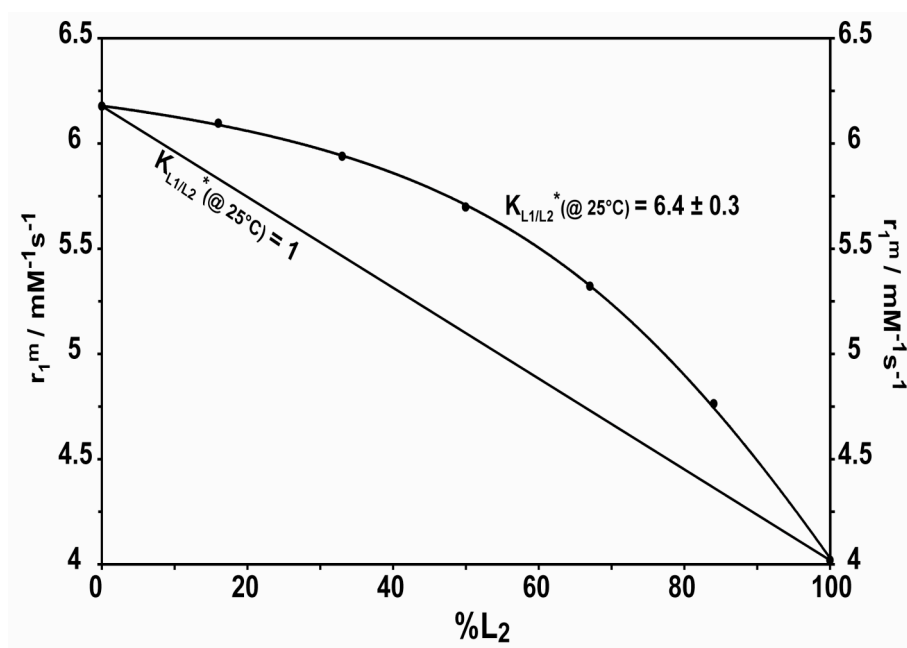
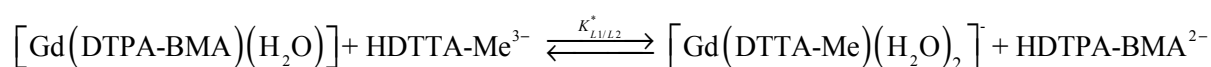


Figure II.3-5. Relaxivities r_1^m of samples containing different concentrations of DTPA-BMA (% L₂). The conditional stability constant $K_{L1/L2}^*$ is calculated from a fit.

The thermodynamic relative stability constant $K_{L1/L2}$ (eq 10), which is independent from the pH, can be calculated using $\alpha_{L_1} = 332.4$ and $\alpha_{L_2} = 12.7$ (calculated from values in Table II.3-1 and sample compositions) as $K_{L1/L2} = 168$. The conditional relative stability constant $K_{L1/L2}^*$ obtained from the competition experiment by relaxometry can be compared to the value

calculated from the stability constants from several potentiometric experiments $\log K_{\text{Gd-DTTA-Me}} = 18.60$ (this work, Table II.3-1) and $\log K_{\text{Gd-DTPA-BMA}} = 16.85$, reported by Rizkalla et al.⁴⁵ Both the directly measured and the calculated $K_{L1/L2}^*$ show a higher relative thermodynamic stability of $[\text{Gd}(\text{DTTA-Me})(\text{H}_2\text{O})_2]^-$ compared to $[\text{Gd}(\text{DTPA-BMA})(\text{H}_2\text{O})]^-$ (Table II.3-2) at pH 8.3. The conditional relative stability constant $\log K_{L1/L2}^*$ as a function of the pH is shown in Figure II.3-6. At pH above 6.8, $[\text{Gd}(\text{DTTA-Me})(\text{H}_2\text{O})_2]^-$ is more stable than $[\text{Gd}(\text{DTPA-BMA})(\text{H}_2\text{O})]^-$. Especially at physiological pH 7.4, the gadolinium complex with the heptadentate DTTA-Me^{4-} is about three times more stable than the one with the octadentate DTPA-BMA^{3-} , as calculated from the directly measured $K_{L1/L2}^*$.

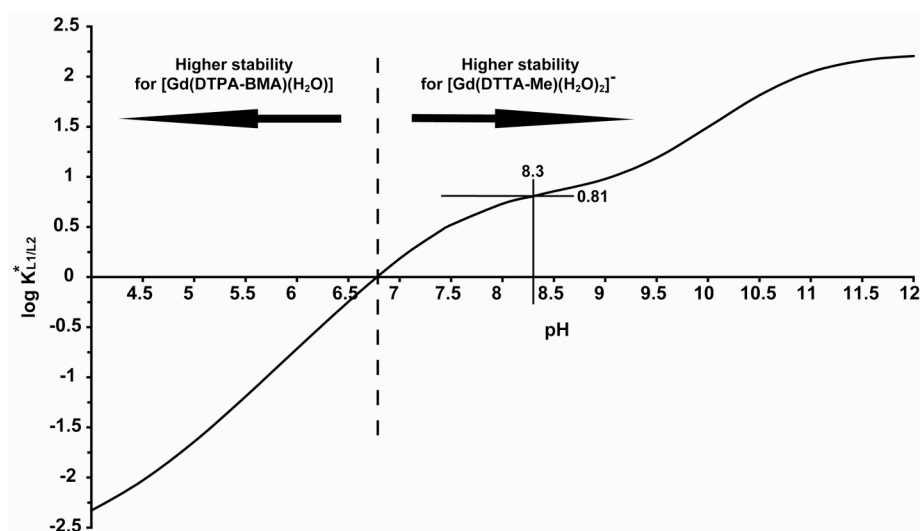


Figure II.3-6: Conditional relative stability constant $\log K_{L1/L2}^*$ as a function of pH.

Relative stability constants of very stable complexes are often measured by competition experiments. In the case of complexes of lanthanide cations, the methods mainly used are spectrophotometric competition titration using colored ligands^{46, 47} or potentiometric competition experiments using, for example, EDTA^{48, 49}. The measurement of ^1H NMR relaxivities at one magnetic field in mixed solutions of gadolinium complexes is a simple method to establishing the relative stabilities of gadolinium complexes. The only necessary condition is that the relaxivities of the two individual complexes have to be sufficiently different with respect to experimental uncertainty. By a proper choice of the magnetic field,

such a difference in the relaxivity can always be found and therefore the relative stability constants can be measured directly for any couple of gadolinium complexes. The standard deviation of 5% on $K_{L1/L2}^*$ obtained in our case is much lower than what can typically be obtained by potentiometric competition experiments.

Table II.3-2. Conditional, $K_{L1/L2}^*$, and Thermodynamic, $K_{L1/L2}$, Relative Stability Constants (T=25 °C, I = 0.1M) for $[\text{Gd}(\text{DTTA-Me})(\text{H}_2\text{O})_2]^-$ (GdL₁) and $[\text{Gd}(\text{DTPA-BMA})(\text{H}_2\text{O})]$ (GdL₂) from Relaxivity and Potentiometric Experiments.

	relaxivity ^a	potentiometry ^b
$\log K_{L1/L2}^*$, pH 8.3	0.81 ± 0.02^c	0.33
$\log K_{L1/L2}^*$, pH 7.4	0.47	-0.01
$\log K_{L1/L2}$	2.23	1.75 ^d

^a I = 0.1 M NaCl. ^b I = 0.1 M KCl; $\log K_{ML}$ for $[(\text{Gd}(\text{DTPA-BMA})(\text{H}_2\text{O}))]$ from ref. [38]. ^cMeasured directly. ^dCalculated from $\log K_{\text{GdL}}$ and $\log K_{\text{GdL1}}$.

II.3.5 Transmetalation of $[\text{Gd}(\text{DTTA-Me})(\text{H}_2\text{O})_2]^-$ with Zn^{2+}

Zn^{2+} is one of the most abundant endogenous metal ions with a concentration of $\sim 32 \mu\text{M}$ in the human plasma.⁵⁰ To determine the stability of the $[\text{Gd}(\text{DTTA-Me})(\text{H}_2\text{O})_2]^-$ complex against the presence of Zn^{2+} ions, a transmetalation experiment was carried out in phosphate buffer (pH 7.0).³⁵ Replacement of Gd^{3+} in the complex with Zn^{2+} leads to free gadolinium ions, which precipitate in the presence of phosphate as GdPO_4 . Because Zn^{2+} is diamagnetic, the total amount of paramagnetic species in solution decreases and therefore the measured decrease in relaxation allows on to following the transmetalation reaction.

In Figure II.3-7, the evolution with time of the ratio of relaxation rates $R_1^m / R_{1,0}$ where R_1^m is the relaxation rate at time t and $R_{1,0}$ is the relaxation rate at time zero (just before successive addition of phosphate and Zn^{2+}) is shown for $[\text{Gd}(\text{DTTA-Me})(\text{H}_2\text{O})_2]^-$ together with the evolution of $[(\text{Gd-DTPA-BMA})(\text{H}_2\text{O})]$ as comparison. After a small initial increase (Figure II.3-7 inset), the relative relaxation rates of both complexes decrease because of the transmetalation reaction. According to Laurent et al.,^{35, 51} two characteristic values can be

used to describe the behavior of a Gd^{3+} chelate in a transmetalation experiment, i.e. the time to reach $R_1^m/R_{1,0} = 0.8$ (ratio index) which gives information about the kinetics of the reaction, and the $R_1^m/R_{1,0}$ value at very long time, $t=\infty$ (long time index, considered after 3 days = 4320 min), reflecting the thermodynamic aspect of the system.

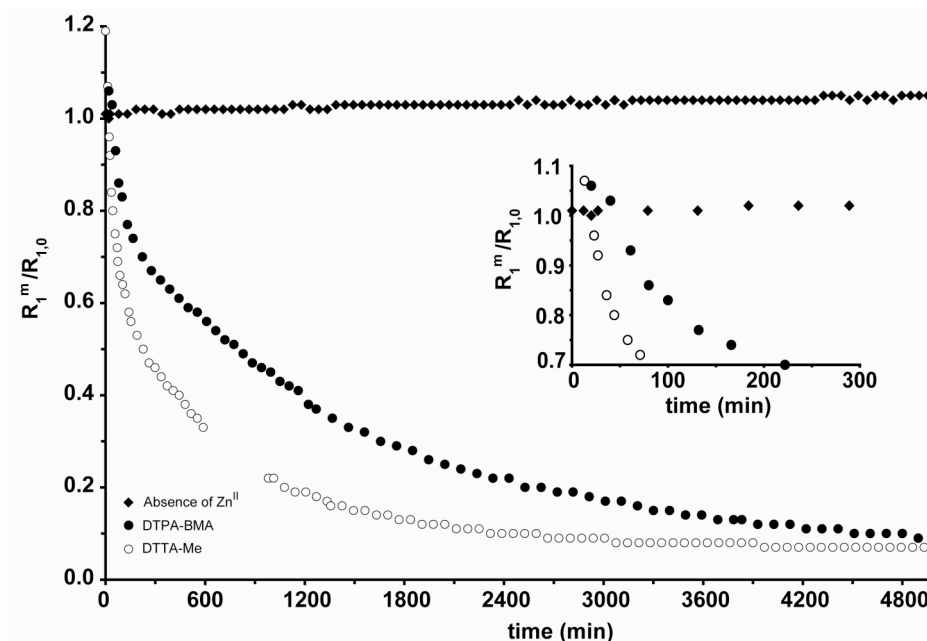


Figure II.3-7: Evolution of $R_1^m/R_{1,0}$ ($T = 310 \text{ K}$; $B = 1.41 \text{ T}$, 60 MHz ; $\text{pH } 7.0$) versus time for (○) $[\text{Gd}(\text{DTTA-Me})(\text{H}_2\text{O})_2]^-$ and (●) $[\text{Gd}(\text{DTPA-BMA})(\text{H}_2\text{O})]^-$ complexes in the presence of equimolar amounts of Zn^{2+} ions in phosphate buffer solution. Evolution of (◆) $[\text{Gd}(\text{DTTA-Me})(\text{H}_2\text{O})_2]^-$ in a phosphate buffer solution without Zn^{2+} ions.

From the values in Table II.3-3, it can be concluded that transmetalation is twice as fast for $[\text{Gd}(\text{DTTA-Me})(\text{H}_2\text{O})_2]^-$ as compared to $[(\text{Gd-DTPA-BMA})(\text{H}_2\text{O})]$. In any case, both are much less stable in respect to transmetalation than the complexes with cyclic ligands like DOTA^{4-} or HPDO3A^{3-} which are especially kinetically stable.^{35, 52} The lower relative thermodynamic stability of $[\text{Gd}(\text{DTTA-Me})(\text{H}_2\text{O})_2]^-$ against transmetalation with Zn^{2+} as compared to $[(\text{Gd}(\text{DTPA-BMA})(\text{H}_2\text{O}))]$ can be understood by comparing the stability constants K_{ML} for Gd^{3+} and Zn^{2+} (Table 1). Even if $[\text{Gd}(\text{DTTA-Me})(\text{H}_2\text{O})_2]^-$ has a higher stability than that of $[(\text{Gd}(\text{DTPA-BMA})(\text{H}_2\text{O}))]$, the relative stability with respect to Zn^{2+} is lower as a consequence of the high stability of the zinc complex of DTTA-Me^{4-} : $\log(K_{\text{Gd-DTTA-Me}}/K_{\text{Zn-DTTA-Me}}) = 0.91$ in respect to $\log(K_{\text{Gd-DTPA-BMA}}/K_{\text{Zn-DTPA-BMA}}) = 4.81$.⁵³

Table II.3-3: Transmetalation with Zn^{2+} : time required to reach the ratio $R_1^m(t)/R_{1,0} = 0.8$ (ratio index. ref. [55]) and value of $R_1^m(t = 4320)/R_{1,0}$ (long time index ref. [55]) for $[\text{Gd}(\text{DTTA-Me})(\text{H}_2\text{O})_2]^-$ and $[\text{Gd}(\text{DTPA-BMA})(\text{H}_2\text{O})]$ (37° C, pH 7.0).

	t for $R_1^m(t)/R_{1,0} = 0.8$	$R_1^m(t = 4320)/R_{1,0}$	
	[min]		
$[\text{Gd}(\text{DTTA-Me})(\text{H}_2\text{O})_2]^-$	44	0.07	this work
$[\text{Gd}(\text{DTPA-BMA})(\text{H}_2\text{O})]$	100 / 100	0.11 / 0.10	this work / [55]
$[\text{Gd}(\text{DTPA})(\text{H}_2\text{O})]^{2-}$	250	0.49	[55]
$[\text{Gd}(\text{DOTA})(\text{H}_2\text{O})]^-$	>5000	0.99	[55]
$[\text{Gd}(\text{HPDO3A})(\text{H}_2\text{O})]^-$	>5000	0.99	[55]

To confirm that the presence of Zn^{2+} ions is provoking transmetalation we performed a blank experiment (Figure II.3-7). A sample containing the $[\text{Gd}(\text{DTTA-Me})(\text{H}_2\text{O})_2]^-$ complex only with phosphate buffer but without Zn^{2+} ions shows no change in relaxivity over more than three days, confirming that phosphate at the considered concentration and pH is unable to extract Gd^{3+} from the chelate.

II.3.6 Search for Adduct Formation between $[\text{Gd}(\text{DTTA-Me})(\text{H}_2\text{O})_2]^-$ and L-lactate

It has been shown by NMR^{18, 20} and by luminescence emission studies^{54, 55} that lanthanide complexes with heptadentate DO3A based ligands form ternary adducts with bidentate anions like carbonate, acetate, phosphate, malonate, and lactate. The anions replace the two water molecules from the first coordination sphere of the lanthanide, leading in the case of gadolinium complexes to a substantial decrease in relaxivity. Like DO3A based ligands, DTTA-Me^{4-} is heptadentate and its Gd^{3+} complex has also two water molecules in the first coordination sphere. Therefore, it could be prone to bind bidentate anions. We studied the eventual complex formation of $[\text{Gd}(\text{DTTA-Me})(\text{H}_2\text{O})_2]^-$ with L-lactate anions, which are present in human blood at ~2 mM, concentrations up to 25 mM can be found under stress or shock.^{56, 57} Following Terreno et al.²⁰ we used ^1H NMR relaxivity, r_1 , to detect the replacement of first sphere-water molecules by a lactate anion.

The change in relaxivity upon titration of $[\text{Gd}(\text{DTTA-Me})(\text{H}_2\text{O})_2]^-$ with L-lactate is shown in Figure II.3-8. Addition of 10 equivalents of lactate to a 1mM solution of $[\text{Gd}(\text{DTTA-Me})(\text{H}_2\text{O})_2]^-$ leads only to a slight decrease in r_1 of 6.5 %. This decrease is much smaller than that observed on complexes based on cyclic DO3A derivatives (Figure II.3-8). Even with 50 equivalents of lactate relaxivity decreases by about $2 \text{ mM}^{-1} \text{ s}^{-1}$. Possible explanations for the small decrease of r_1 are (1) the formation of a small amount of the ternary adduct $[\text{Gd}(\text{DTTA-Me})(\text{C}_3\text{O}_3\text{H}_5)]^{2-}$, (2) the replacement of only one water molecule on some of the Gd^{3+} complexes, and (3) the formation of an outer-sphere complex, leading to a decrease of outer-sphere relaxation.

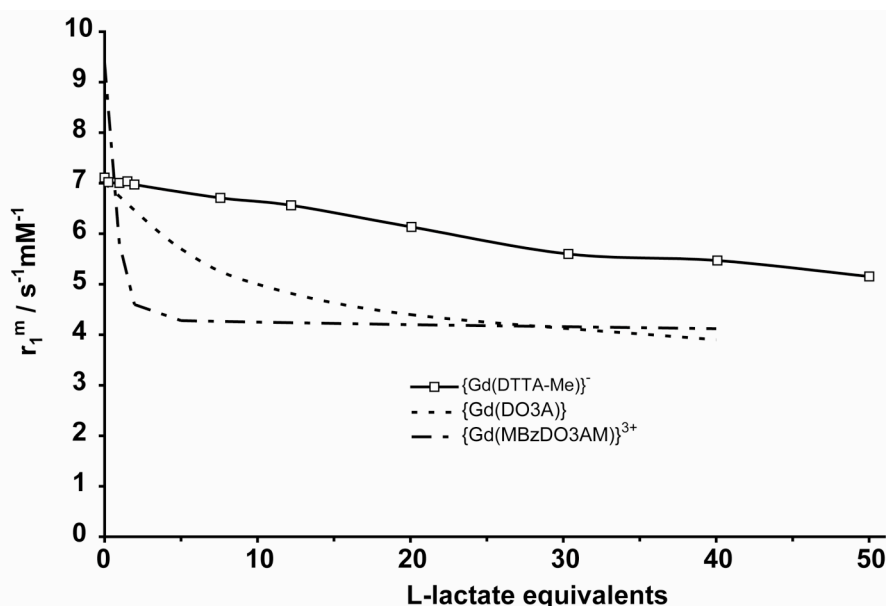


Figure II.3-8: Relaxivity r_1^m ($T = 298 \text{ K}$; $B = 0.235 \text{ T}$, 10 MHz ; $\text{pH } 7.0$) versus L-lactate equivalents for 1 mM solutions of $[\text{Gd}(\text{DTTA-Me})(\text{H}_2\text{O})_2]^-$ (\square) (this work), and $[\text{Gd}(\text{DO3A})(\text{H}_2\text{O})_2]$ (---), $[\text{Gd}(\text{MBzDO3AM})(\text{H}_2\text{O})_2]^{3+}$ (- · - · -) from ref [20].

The difference in the formation of ternary complexes between compounds with cyclic ligands (DO3A-based) and the acyclic ligand (DTTA-Me^{4-}) is probably due to the arrangement of the two first-shell water molecules. In DO3A-type complexes, these water molecules are adjacent, allowing a bidentate binding of the anion. In the $[\text{Gd}(\text{DTTA-Me})(\text{H}_2\text{O})_2]^-$ complex, the two water molecules are probably not next to each other and the lactate could only bind via one oxygen to the gadolinium. Furthermore, in contrast to DO3A complexes of gadolinium, the $[\text{Gd}(\text{DTTA-Me})(\text{H}_2\text{O})_2]^-$ complexes is negatively charged and the formation

of ternary adducts with anions is less favorable. Furthermore, in contrast to DO3A complexes of gadolinium, the $[\text{Gd}(\text{DTTA-Me})(\text{H}_2\text{O})_2]^-$ complex is negatively charged and the formation of ternary adducts or outer-sphere complexes with anions is less favorable.

II.4 CONCLUSION

We report the synthesis and physicochemical characterization of the gadolinium complex with DTTA-Me^{4-} , derived from the parent TTAHA^{6-} . As other DTTA-type complexes, used, for example, in the metallostar²⁶, $[\text{Gd}(\text{DTTA-Me})(\text{H}_2\text{O})_2]^-$ has two water molecules directly bound to the paramagnetic center. The complex shows thermodynamic protonation and stability constants similar to DTTA bound to bpy or a xylene via a CH_2 group. From ^1H NMR it was concluded that the first protonation occurs on the central nitrogen, followed by protonation of the two terminal nitrogen atoms and deprotonation of the central one. The next protonation steps are a repeated protonation of the central nitrogen followed by the protonation of carboxylic acids. The pGd value, which is indicative for the stability at physiological conditions, is very close to that of $[\text{Gd}(\text{DTPA-BMA})(\text{H}_2\text{O})]$.

To measure the conditional relative stability constant for two gadolinium complexes, we propose a method based on relaxivity measurements. This versatile method allows the determination of the relative stability for any couple of ligands, provided its ^1H NMR relaxivities are sufficiently different at an appropriate magnetic field. Using this method, we found that in a slightly basic environment (pH 8.3) the $[\text{Gd}(\text{DTTA-Me})(\text{H}_2\text{O})_2]^-$ complex has a higher stability in respect to $[\text{Gd}(\text{DTPA-BMA})(\text{H}_2\text{O})]$ as has been shown by the direct competition experiment using relaxivities as the indicator. Transmetalation with Zn^{2+} is however, less favorable for the heptadentate DTTA-Me^{4-} compared to the octadentate DTPA-BMA^{3-} . Whereas the long time behavior of both complexes is similar, showing relatively strong transmetalation, the metal exchange from Gd^{3+} to Zn^{2+} is about twice as fast for DTTA-Me^{4-} due to the higher stability of the zinc complex. In contrast to DO3A-based ligands with two water molecules in the first coordination sphere, the formation of ternary complexes with the bidentate lactose anion is very weak. Even at a 10-fold excess of the anion, the measured relaxivity decreases only very slightly.

From the results, it can be concluded that the Gd^{3+} complex of heptadentate DTTA-Me^{4-} behaves similarly as that of the commercial octadentate DTPA-BMA^{3-} . Considering recent suspicions against $[\text{Gd}(\text{DTPA-BMA})(\text{H}_2\text{O})]$ for being involved in Nephrogenic Systemic Fibrosis (NSF) disease, DTTA-type chelates will not be admitted as contrast agents in clinical MRI. However, their use *in vitro* and in animal studies is absolutely conceivable, mainly at

high magnetic fields, where the increase of inner-sphere-coordination water actually seems to be the only promising way to increase the relaxivity.

II.5 ACKNOWLEDGEMENTS

Prof. André E. Merbach is acknowledged for numerous helpful and stimulating discussions.

Dr. Caroline Cannizzo for the synthesis of the ligand DTTA-Me and for the codirection of the master students.

Florent Beyrière and Cora Prestinari for having decided to do their semester projects in our lab and for their interest in this project.

II.6 REFERENCES

1. P. Caravan, J. J. Ellison, T. J. McMurry and R. B. Lauffer, *Chem. Rev.*, 1999, **99**, 2293-2352.
2. A. E. Merbach and É. Tóth, eds., *The Chemistry of Contrast Agents in Medical Magnetic Resonance Imaging*, 1st edn., John Wiley & Sons, Chichester, 2001.
3. P. Caravan, *Chem. Soc. Rev.*, 2006, **35**, 512-523.
4. Z. H. Endre, *Int. Med. J.*, 2007, **37**, 429-431.
5. T. Grobner and F. C. Prischl, *Kidney International*, 2007, **72**, 260-264.
6. M. A. Perazella, *Clin. J. Am. Soc. Nephrol.*, 2007, **2**, 200-202.
7. H. Ersoy and F. J. Rybicki, *J. Magn. Reson. Imag.*, 2007, **26**, 1190-1197.
8. Z. Jaszberenyi, L. Moriggi, P. Schmidt, C. Weidensteiner, R. Kneuer, A. E. Merbach, L. Helm and É. Tóth, *J. Biol. Inorg. Chem.*, 2007, **12**, 406-420.
9. H. Kobayashi and M. W. Brechbiel, *Adv. Drug Deliv. Rev.*, 2005, **57**, 2271-2286.
10. S. Langereis, A. Dirksen, T. M. Hackeng, M. H. P. Van Genderen and E. W. Meijer, *New J. Chem.*, 2007, **31**, 1152-1160.
11. S. Laus, A. Sour, R. Ruloff, É. Tóth and A. E. Merbach, *Chem. Eur. J.*, 2005, **11**, 3064-3076.
12. S. Aime, E. Gianolio, D. Corpillo, C. Cavalotti, G. Palmisano, M. Sisti, G. B. Giovenzana and R. Pagliarin, *Helv. Chim. Acta*, 2003, **86**, 615-632.
13. A. R. Johnson, B. O'Sullivan and K. N. Raymond, *Inorg. Chem.*, 2000, **39**, 2652-2660.
14. E. J. Werner, S. Avedano, M. Botta, B. P. Hay, E. G. Moore, S. Aime and K. N. Raymond, *J. Am. Chem. Soc.*, 2007, **129**, 1870-1871.
15. S. Aime, L. Calabi, C. Cavallotti, E. Gianolio, G. B. Giovenzana, P. Losi, A. Maiocchi, G. Palmisano and M. Sisti, *Inorg. Chem.*, 2004, **43**, 7588-7590.
16. É. Tóth, S. Vauthey, D. Pubanz and A. E. Merbach, *Inorg. Chem.*, 1996, **35**, 3375-3379.
17. R. S. Dickins, D. Parker, J. I. Bruce and D. J. Tozer, *J. Chem. Soc., Dalton Trans.*, 2003, 1264-1271.
18. M. Botta, S. Aime, A. Barge, G. Bobba, R. S. Dickins, D. Parker and E. Terreno, *Chem. Eur. J.*, 2003, **9**, 2102-2109.

19. E. Terreno, P. Boniforte, M. Botta, F. Fedeli, L. Milone, A. Mortillaro and S. Aime, *Eur. J. Inorg. Chem.*, 2003, 3530-3533.
20. E. Terreno, M. Botta, P. Boniforte, C. Bracco, L. Milone, B. Mondino, F. Uggeri and S. Aime, *Chem. Eur. J.*, 2005, **11**, 5531-5537.
21. E. Brücher, in *Magnetic Resonance Contrast Agents*, ed. Krause, W., Springer, Heidelberg, 2002, pp. 103-122.
22. S. Aime, E. Terreno, M. Botta, J. I. Bruce, D. Parker and V. Mainero, *Chem. Commun.*, 2001, 115-116.
23. J. Costa, É. Tóth, L. Helm and A. E. Merbach, *Inorg. chem.*, 2005, **44**, 4747-4755.
24. J. Costa, R. Ruloff, L. Burai, L. Helm and A. E. Merbach, *Journal of the American Chemical Society*, 2005, **127**, 5147-5157.
25. J. B. Livramento, C. Weidensteiner, M. I. M. Prata, P. R. Allegrini, C. F. G. C. Geraldes, L. Helm, R. Kneuer, A. E. Merbach, A. C. Santos, P. Schmidt and É. Tóth, *Contrast Med. Mol. Imaging*, 2006, **1**, 30-39.
26. J. B. Livramento, A. Sour, A. Borel, A. E. Merbach and É. Tóth, *Chem. Eur. J.*, 2006, **12**, 989-1003.
27. J. B. Livramento, L. Helm, A. Sour, C. O'Neil, A. E. Merbach and É. Tóth, *Dalton Trans.*, 2008, 1195 -1202.
28. G. Schwarzenbach, H. Senn and G. Anderegg, *Helv. Chim. Acta*, 1957, **40**, 1886-1900.
29. H. M. Irving, M. G. Miles and L. D. Pettit, *Analytica Chimica Acta*, 1967, **38**, 475-488.
30. P. Gans, A. Sabatini and A. Vacca, *Talanta*, 1996, **43**, 1739-1753.
31. A. Sabatini, A. Vacca and P. Gans, *Coord. Chem. Rev.*, 1992, **120**, 389-405.
32. C. Ammann, P. Meier and A. E. Merbach, *J. Magn. Reson.*, 1982, **46**, 319-321.
33. F. Yerly, *VISUALISEUR/OPTIMISEUR*, EPFL, 2003
34. M. P. M. Marques, C. Geraldes, A. D. Sherry, A. E. Merbach, D. H. Powell, D. Pubanz, S. Aime and M. Botta, *J. Alloys and Compounds*, 1995, **225**, 303-307.
35. S. Laurent, L. Vander Elst, F. Copoix and R. N. Muller, *Invest. Radiology*, 2001, **36**, 115-122.
36. K. Mikkelsen and S. O. Nielsen, *J. Phys. Chem.*, 1960, **64**, 632-637.
37. D. D. Perrin and B. Dempsey, *Buffers for pH and Metal Ions Control*, Chapman and Hall, London, 1974.
38. V. C. Pierre, M. Melchior, D. M. J. Doble and K. N. Raymond, *Inorg. Chem.*, 2004, **43**, 8520-8525.

39. É. Tóth, D. Pubanz, S. Vauthey, L. Helm and A. E. Merbach, *Chem. Eur. J.*, 1996, **2**, 1607-1615.
40. Y.-M. Wang, C.-H. Lee, G.-C. Liu and R.-S. Sheu, *J. Chem. Soc., Dalton Trans.*, 1998, 4113-4118.
41. P. Letkeman and A. E. Martell, *Inorg. Chem.*, 1979, **18**, 1284-1289.
42. P.-K. Tse and J. E. Powell, *Inorg. Chem.*, 1985, **24**, 2727-2730.
43. C. Paul-Roth and K. N. Raymond, *Inorg Chem*, 1995, **34**, 1408-1412.
44. É. Tóth, L. Helm and A. E. Merbach, in *The Chemistry of Contrast Agents in Medical Magnetic Resonance Imaging*, eds. Merbach, A. E. and Tóth, É., John Wiley & Sons, Chichester, 2001, pp. 45-119.
45. E. N. Rizkalla, G. R. Choppin and W. Cacheris, *Inorg. Chem.*, 1993, **32**, 582-586.
46. A. D. Sherry, W. P. Cacheris and K.-T. Kuan, *Magn. Reson. Med.*, 1988, **8**, 180-190.
47. J. Huskens and A. D. Sherry, *Inorg. Chem.*, 1996, **35**, 5137-5143.
48. J. Huskens, D. A. Torres, Z. Kovacs, J. P. Andre, C. F. G. C. Geraldes and A. D. Sherry, *Inorg. Chem.*, 1997, **36**, 1495-1503.
49. Z. Jaszberenyi, I. Banyai, E. Brücher, R. Kiraly, K. Hideg and T. Kalai, *Dalton Trans.*, 2006, 1082-1091.
50. L. S. Nikolaeva, V. V. Chirkov, N. A. Dobrynina, L. L. A. and V. E. Pastorova, *Pharm. Chem. J.*, 2005, **39**, 57-63.
51. S. Laurent, L. Vander Elst and R. N. Muller, *Contrast Med. Mol. Imaging*, 2006, **1**, 128-137.
52. S. Laurent, F. Botteman, L. Vander Elst and R. N. Muller, *Helv. Chim. Acta*, 2004, **87**, 1077-1089.
53. W. P. Cacheris, S. C. Quay and S. M. Rocklage, *Magn. Reson. Imag.*, 1990, **8**, 467-481.
54. J. I. Bruce, R. S. Dickins, L. J. Govenlock, T. Gunnlaugsson, S. Lopinski, M. P. Lowe, D. Parker, R. D. Peacock, J. J. B. Perry, S. Aime and M. Botta, *J. Am. Chem. Soc.*, 2000, **122**, 9674-9684.
55. R. S. Dickins, S. Aime, A. Batsanov, A. Beeby, M. Botta, J. I. Bruce, J. A. K. Howard, C. S. Love, D. Parker, R. D. Peacock and H. Puschmann, *J. Am. Chem. Soc.*, 2002, **124**, 12697-12705.
56. B. A. Mizock and J. L. Falk, *Critical care medicine*, 1992, **20**, 80-93.
57. D. Lafrance, L. C. Lands and D. H. Burns, *Talanta*, 2003, **60**, 635-641.

CHAPTER III.

RUTHENIUM-BASED

METALLOSTAR: SYNTHESIS, SENSITIZED

LUMINESCENCE AND ¹H RELAXIVITY

TABLE OF CONTENTS CHAPTER III

<u>III.1</u>	<u>INTRODUCTION</u>	<u>81</u>
<u>III.2</u>	<u>EXPERIMENTAL SECTION</u>	<u>84</u>
III.2.1	SYNTHESIS AND CHARACTERIZATION	84
III.2.2	^1H NMR SPECTROSCOPY	85
III.2.3	MAGNETIC RELAXIVITY	85
III.2.4	OPTICAL SPECTROSCOPY	85
<u>III.3</u>	<u>RESULTS AND DISCUSSION</u>	<u>87</u>
III.3.1	THE RU(II) BASED METALLOSTAR - A SYNTHETIC CHALLENGE	87
III.3.2	OPTICAL CHARACTERIZATION OF THE TRIS-(2,2'-BIPYRIDYL)RUTHENIUM(II) UNIT	88
III.3.3	SENSITIZED EU LUMINESCENCE	91
III.3.4	^1H RELAXIVITY OF $\{\text{Ru}[\text{Gd}_2\text{BPY-DTTA}_2(\text{H}_2\text{O})_4]_3\}^{4+}$	94
<u>III.4</u>	<u>CONCLUSION</u>	<u>99</u>
<u>III.5</u>	<u>ACKNOWLEDGEMENTS</u>	<u>100</u>
<u>III.6</u>	<u>REFERENCES</u>	<u>101</u>

III.1 INTRODUCTION

The development of lanthanide-containing markers and labels for analytical and biophysical purposes is presently a very active field of research in view of important applications in magnetic resonance imaging (MRI)¹ and optical cell imaging and sensing.²⁻⁴

Complexes of trivalent gadolinium act as contrast agents for T_1 -weighted MR images since they decrease the longitudinal relaxation time T_1 by increasing the relaxation rate of the spins of the surrounding water protons. The effectiveness of an MRI contrast agent is measured in terms of its relaxivity, r_1 , which is defined as the longitudinal relaxation rate in s^{-1} measured in a solution of a Gd^{3+} concentration of 1 mM. The water proton relaxivity of a gadolinium compound is mainly governed by four parameters: the number of water molecules in the first sphere of Gd^{3+} (q), the exchange rate for these water molecules, the relaxation behaviour of the electron spin of Gd^{3+} , and the rotational diffusion of the complex in solution (τ_R).⁵⁻⁸ The influence of these parameters on r_1 varies strongly with the strength of magnetic field applied, with exception of the coordination number q which is mainly a linear scaling factor. Typically, mid- and large-size compounds ($\text{MW} > 1200 \text{ g mol}^{-1}$) show a maximum of relaxivity at fields between 0.24 and 2.4 T corresponding to proton resonance frequencies of 10 to 100 MHz. The value and the exact field of the relaxivity maximum strongly depend on the rotational correlation time τ_R : the slower is the rotational diffusion of the complex (long τ_R), the higher is the relaxivity and the lower is the magnetic field of the maximum

Livramento et al⁹⁻¹¹ presented recently a compound they named metallostar which is based on the concept of self-assembly of gadolinium chelates around a d-transition metal centre first described by Jacques and Desreux.^{12,13} Three bipyridyl ligands, each bearing two chelating units complexed with Gd^{3+} , self-assemble with Fe^{2+} to form an edifice with six paramagnetic centres. The use of DTTA as chelating group ($q = 2$) leads to a total number of 12 water molecules bound to Gd^{3+} and a relaxivity of $33.2 \text{ s}^{-1} \text{ mM}^{-1}$ at 1.4 T (60 MHz) and 25 °C. The r_1 -values of this metallostar were found to be remarkable at very high magnetic fields ($r_1 = 15.8 \text{ s}^{-1} \text{ mM}^{-1}$ at 4.7 T, 200 MHz, and 37 °C) and led to signal enhancement in the inversion recovery MRI images on mice considerably higher than after the injection of the commercial contrast agent $[\text{Gd}(\text{DOTA})(\text{H}_2\text{O})]^-$.⁹

Relaxivity measurements in mouse serum and phosphate-buffered saline (PBS) solution showed that metallostars may not have sufficiently long-term stability in biological media¹⁰ and therefore an increase in stability of the bipyridyl binding to the d-transition metal centre is desirable. In order to increase the thermodynamic and kinetic stability of metallostar molecules we have chosen Ru^{2+} as the central metal ion since $[\text{Ru}(\text{bpy})_3]^{2+}$ is known for its outstanding chemical stability.¹⁴⁻¹⁶ Furthermore, this compound has remarkable photophysical properties, in particular it features metal-to-ligand charge transfer states which are shifted into the visible part of the spectrum.¹⁶

In the same time numerous lanthanide complexes with encapsulating ligands have been developed, which exhibit reasonable visible or near-infrared emission in solution upon excitation in the near UV.¹⁷⁻¹⁹ The main problem of these systems in bioanalytical applications is autofluorescence and photodegradation of the biological species with UV light. A possible way to circumvent these difficulties is to develop luminescent markers in which the emission can be excited in the visible part of the electromagnetic spectrum,^{20, 21} in particular through states involving d-transition metal ions.²² Combining the $[\text{Ru}(\text{bpy})_3]^{2+}$ centre with a luminescent lanthanide chelate could therefore lead to a compound with interesting bimodal properties as both MRI contrast agent and luminescent probe.

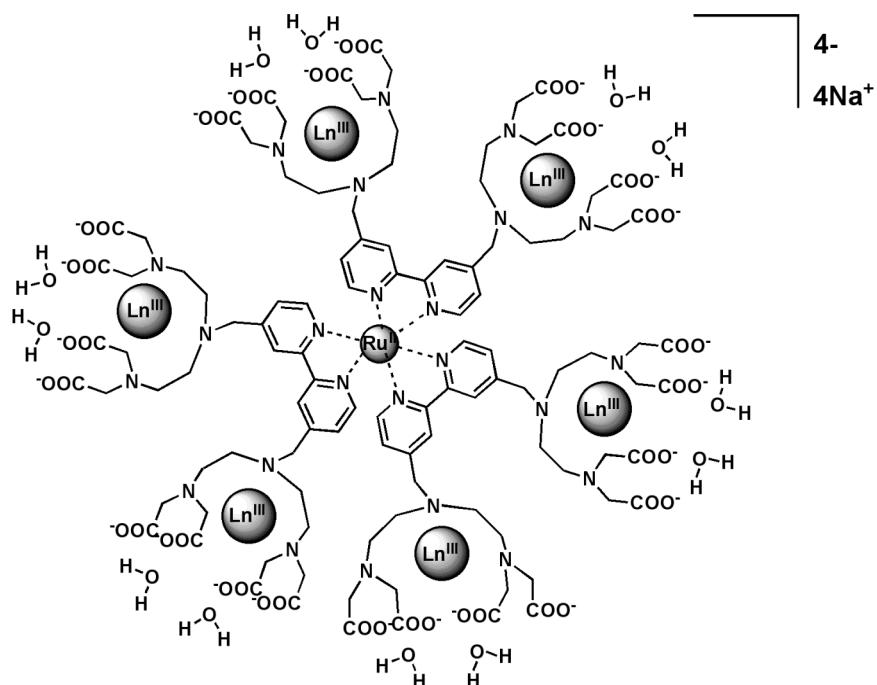


Figure III.1-1: Self-assembled Ru(II)-based metallostar systems $\{\text{Ru}[\text{Ln}_2\text{bpy-DTTA}_2(\text{H}_2\text{O})_4]_3\}^{4-}$ with ($\text{Ln} = \text{Y}, \text{Gd}, \text{or Eu}$).

In this chapter, we report the synthesis and properties of three d/f heptametallic assemblies $\{\text{Ru}[\text{Ln}_2\text{bpy-DTTA}_2(\text{H}_2\text{O})_4]_3\}^{4-}$ with $\text{Ln} = \text{Y}^{3+}, \text{Gd}^{3+}, \text{Eu}^{3+}$ (Figure III.1-1). While the diamagnetic yttrium complex allows structural characterization by ^1H NMR spectroscopy, the gadolinium complex is used to obtain the relaxivity properties via nuclear magnetic relaxation dispersion (NMRD) profiles. Luminescence properties of the europium assembly are presented.

III.2 EXPERIMENTAL SECTION

III.2.1 Synthesis and Characterization

The synthesis of the ligand $\text{H}_8\text{bpy-DTTA}_2$ has been described in a previous communication.¹¹ $[\text{Ru}(\text{H}_2\text{O})_6](\text{OTs})_2$ ($\text{OTs}^- = p\text{-toluenesulfonate anion}$) was synthesized according to the literature.²³

$\text{H}_8\text{bpy-DTTA}_2$ was first reacted with a slight excess (1-2%) of LnCl_3 ($\text{Ln} = \text{Y}^{3+}, \text{Gd}^{3+}, \text{Eu}^{3+}$) to form $[\text{Ln}_2\text{bpy-DTTA}_2(\text{H}_2\text{O})_4]^{2-}$. The synthesis of metallostars was first optimized with the diamagnetic yttrium complex in D_2O and under argon atmosphere to allow monitoring the degree of completion of the reaction by ^1H NMR. All equipment was carefully degassed under Ar atmosphere. In a round-bottomed flask, 2 mL of D_2O were added to $[\text{Ru}(\text{H}_2\text{O})_6](\text{OTs})_2$ (37.7 μmol) under stirring. In a second flask, a stoichiometric excess of $[\text{Y}_2\text{bipy-DTTA}_2(\text{H}_2\text{O})_4]^{2-}$ (118.8 μmol) was dissolved in 4 mL of D_2O . The pD was adjusted to 6.5 with 0.1 M NaOD. The purple Ru^{2+} solution was slowly transferred by cannula to the ligand-containing solution and the complexation reaction was performed at 95°C . Colour changed rapidly to dark red. Triethylamine (240 μmol) was added after 4 h. After 6 h of continuous stirring at 95°C , the reaction was complete as indicated by ^1H NMR, and the solution displayed an intense orange colour. The solution was filtered (Schleicher and Schuell, RC-L 58, 0.2 μm) and evaporated to dryness. The remaining orange solid was dissolved in 2 mL H_2O and loaded onto an exclusion-size column (Sephadex LH-20, 100 g, 40 cm high, 4 cm diam.). The column was eluted with H_2O until the first front (orange) was released. Eluate was recovered by fractions of 10 mL until all the second front (red) was released of the column. The 10 mL eluates were evaporated under reduced pressure to complete dryness, re-dissolved in D_2O and characterized by ^1H NMR (Figure III.3-1). Pure $\text{Na}_4\{\text{Ru}[\text{Y}_2\text{bpy-DTTA}_2(\text{H}_2\text{O})_4]_3\}$ was obtained as an orange solid in 47 % yield (17.7 μmol , 68.8 mg) and was characterized in solution by UV-Vis and ^1H NMR (400 MHz, D_2O , pD = 6.85): $\delta = 7.21$ (d, 6H), 7.64 (d, 6H), 8.34 (s, 6H).

Synthesis with of $\{\text{Ru}[\text{Ln}_2\text{bpy-DTTA}_2(\text{H}_2\text{O})_4]_3\}^{4-}$ with $\text{Ln} = \text{Gd}$ and Eu has been performed following the same procedure. Due to the paramagnetism of Gd^{3+} and Eu^{3+} , characterization of the elutes was only accomplished by UV-vis spectroscopy.

III.2.2 ^1H NMR spectroscopy

All ^1H NMR spectra were recorded on a Bruker DRX-400 spectrometer (9.4 T). The water peak was used as an internal reference ($\delta = 4.8$ ppm).

III.2.3 ^1H relaxivity

The $1/T_1$ NMRD profiles of $\{\text{Ru}[\text{Gd}_2\text{bpy-DTTA}_2(\text{H}_2\text{O})_4]_3\}^{4-}$ were measured at 25.0°C, and 37.0°C on a Stellar Spinmaster fast field cycling NMR relaxometer ($2.35 \cdot 10^{-4}$ - 0.47 T; ^1H Larmor frequencies: 0.01–20 MHz) equipped with a VTC90 temperature control unit, on Bruker Minispecs (0.71 T (30 MHz), 0.94 T (40 MHz), and 1.41 T (60 MHz)), on a Bruker Avance-200 console connected to 2.35 T (100 MHz), and 4.7 T (200 MHz) cryomagnets, on a Bruker DRX-400 (9.4 T, 400 MHz), and on a Bruker Avance-II 800 (18.8 T, 800 MHz) spectrometer. Sample solutions were placed in cylindrical sample containers placed in NMR tubes with 10- or 7.5-mm for relaxometer and high field measurements or for the Bruker Minispecs, respectively. The diamagnetic corrections to the ^1H longitudinal relaxation rates were 0.37 s^{-1} (25.0°C), and 0.33 s^{-1} (37.0°C). In all NMRD measurements the temperature was determined by a substitution technique.²⁴ The gadolinium concentration of the sample was 8.31 mM as obtained from susceptibility measurements performed at 9.4 T.²⁵ Least-squares fitting of the NMRD data was performed by means of the programs VISUALISEUR/OPTIMISEUR²⁶ running on a Matlab platform, version 6.5 for the Solomon-Bloembergen-Morgan theory with Lipari-Szabo model-free approach and by using the “modified Florence” program.^{27,28}

III.2.4 Optical Spectroscopy

Room temperature (295 K) absorption spectra have been measured on a Lambda 900 spectrometer from Perkin Elmer using 1-cm quartz Suprasil[®] (QS) cells.

Steady-state, gated emission, and excitation spectra, as well as lifetime measurements have been recorded on a Fluorolog-FL22-3 spectrometer from Horiba-Jobin-Yvon equipped with a 450 W xenon arc light source, a UV xenon flash tube, a Spex R928 photomultiplier, and double excitation and emission monochromators. For room temperature luminescence measurements the same quartz cell as for absorption was used and for the cryogenic experiments aqueous solutions containing 10 vol% of spectrophotometric grade Glycerol from Acros Organics, were transferred into quartz tubes and cooled to 77 K by immersion of the quartz tubes in liquid nitrogen.

Emission and excitation spectra have been corrected for the instrumental response and the source intensity, respectively, and are displayed as photon flux versus wavelength.

III.3 RESULTS AND DISCUSSION

III.3.1 The Ru(II) based metallostar - a synthetic challenge

Livramento and al. reported the synthesis of $\{\text{Fe}[\text{Gd}_2\text{bpy-DTTA}_2(\text{H}_2\text{O})_4]_3\}$.^{4-10, 11} The metallostar $\{\text{Fe}[\text{Gd}_2\text{bpy-DTTA}_2(\text{H}_2\text{O})_4]_3\}^{4-}$ forms instantaneously on adding Fe^{2+} to a solution of $[\text{Gd}_2\text{bpy-DTTA}_2(\text{H}_2\text{O})_4]^{2-}$. The synthesis of the ruthenium analogue proved to be more tedious, due to fast oxidation of Ru^{2+} in presence of O_2 and due to the high stability of the $\{\text{Ru}[\text{Gd}_2\text{bpy-DTTA}_2(\text{H}_2\text{O})_4]_2\}^{2-}$ intermediate. Rather than forming the Ru^{3+} complex followed by *in situ* reduction, as it is commonly the case for Ru(II)-terpyridine complexes, we started from the hexaaqua ruthenium(II) salt $[\text{Ru}(\text{H}_2\text{O})_6](\text{OTs})_2$, which allowed us to avoid numerous purification steps. As for the iron analogue the ruthenium metallostar was synthesized in two steps: firstly, the ligand bpy-DTTA_2^{8-} was complexed with two lanthanide ions and secondly, the three $[\text{Ln}_2(\text{bipyDTTA})_2]^{2-}$ anionic complexes were self-assembled around the transition metal ion. To avoid side products with one carboxylate arm released from the lanthanide as observed by Costa et al.²⁹, a 1-2% excess of the lanthanide salt was used to allow full complexation of the chelating ligand before reaction with Ru^{2+} . All of the solids, solvents, as well as the glassware were carefully degassed and the complexation reaction was performed at 95°C in aqueous medium under Ar atmosphere to avoid both oxidation from O_2 and N_2 fixation to Ru^{2+} . On one hand, low pH values are usually preferred because they slow down the oxidation of Ru^{2+} ; on the other hand, an acidic medium also slows down the complexation reaction by protonating the bipyridyl nitrogen atoms.¹⁰ The reaction was therefore started at pH 6.5 and was complete after 6 hours. Two equivalents of triethylamine per bipyridine moiety had to be added to prevent a decrease in pH due to protons released during the complexation with Ru^{2+} .

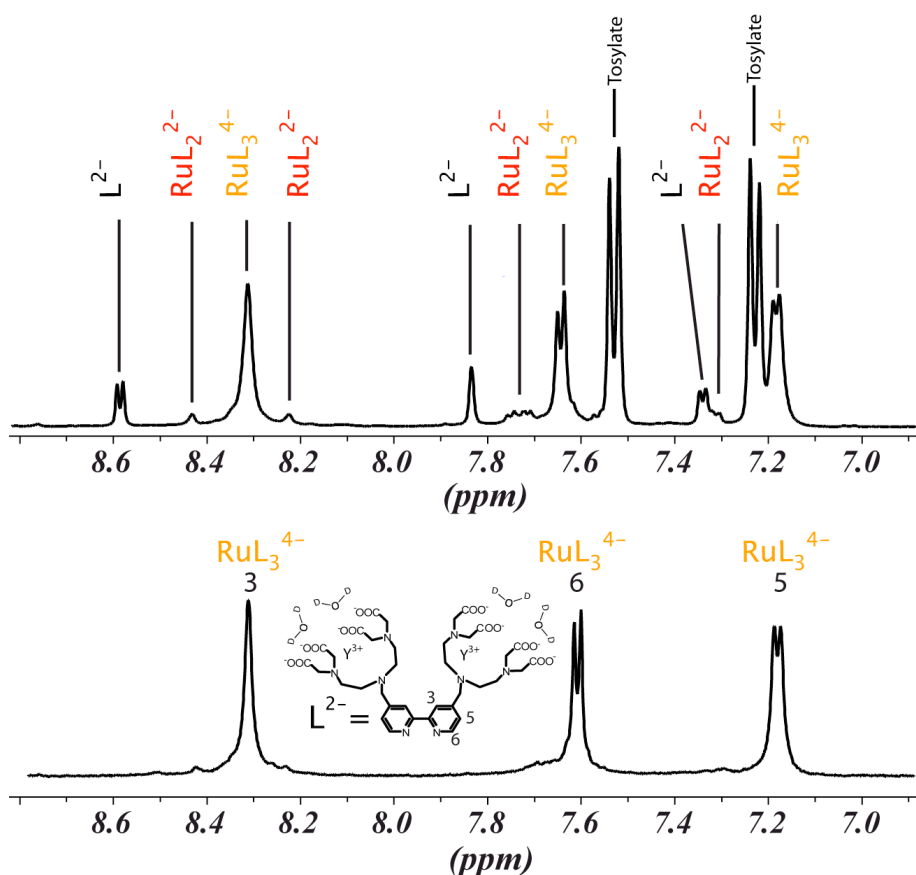


Figure III.3-1. Signal of aromatic protons in the ^1H NMR spectra of L^{2-} : $[\text{Y}_2\text{bpy-DTTA}_2(\text{H}_2\text{O})_4]^{2-}$, RuL_2^{2-} : $\{\text{Ru}[\text{Y}_2\text{bpy-DTTA}_2(\text{H}_2\text{O})_4]_2\}^{2-}$ and RuL_3^{4-} : $\{\text{Ru}[\text{Y}_2\text{bpy-DTTA}_2(\text{H}_2\text{O})_4]_3\}^{4-}$ before (upper figure) and after (lower figure) purification with Sephadex LH20 size-exclusion chromatography.

The chromatographic purification of $\{\text{Ru}[\text{Ln}_2\text{bpy-DTTA}_2(\text{H}_2\text{O})_4]_3\}^{4-}$ has been monitored by ^1H NMR for $\text{Ln} = \text{Y}$ (Figure III.3-1). The first 40 mL of eluate coming out of the size-exclusion column contain pure orange $\{\text{Ru}[\text{Y}_2\text{bpy-DTTA}_2(\text{H}_2\text{O})_4]_3\}^{4-}$. The following 10 mL present traces of $\{\text{Ru}[\text{Y}_2\text{bpy-DTTA}_2(\text{H}_2\text{O})_4]_2(\text{H}_2\text{O})_2\}^{2-}$ and the last 40 mL contain a mixture of red $\{\text{Ru}[\text{Y}_2\text{bpy-DTTA}_2(\text{H}_2\text{O})_4]_3\}^{4-}$, $\{\text{Ru}[\text{Y}_2\text{bpy-DTTA}_2(\text{H}_2\text{O})_4]_2(\text{H}_2\text{O})_2\}^{2-}$ and free $[\text{Y}_2\text{bpy-DTTA}_2(\text{H}_2\text{O})_4]^{4-}$ ligand.

III.3.2 Optical characterization of the tris-(2,2'-bipyridyl)ruthenium(II) unit

Room-temperature absorption (Figure III.3-2(a)), excitation (Figure III.3-2(b), dotted trace) and emission spectra (Figure III.3-2(b), solid trace) of $\{\text{Ru}[\text{Ln}_2\text{bpy-DTTA}_2(\text{H}_2\text{O})_4]_3\}^{4-}$ ($\text{Ln} = \text{Y}^{3+}, \text{Eu}^{3+}$) were recorded in bi-distilled water (1.5×10^{-5} mM) (Table III.3-1). The spectra of

the two-lanthanide complexes look identical in terms of band shapes and positions, and only those of the Eu^{3+} complex are shown here.

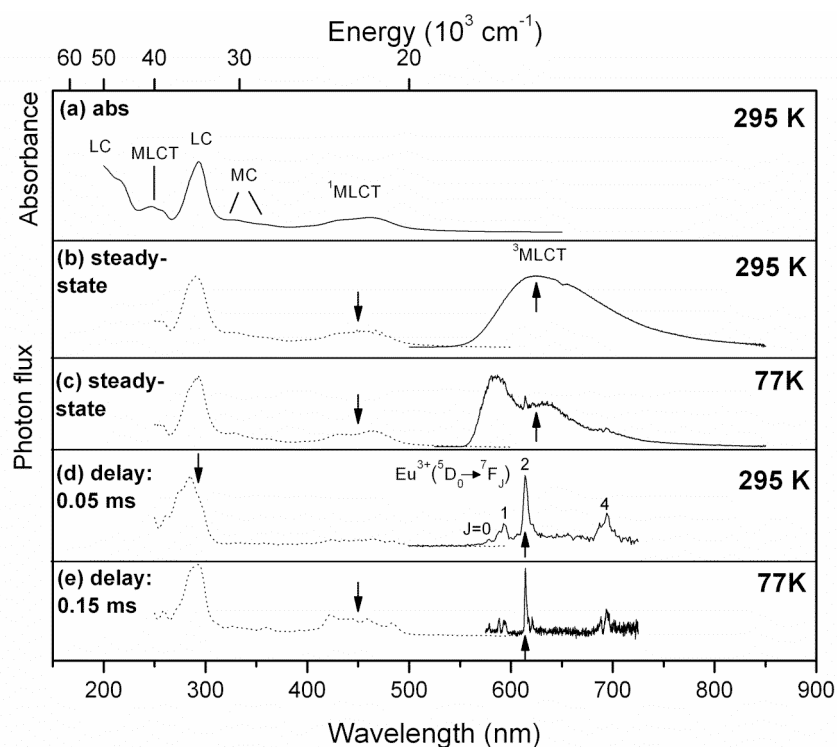


Figure III.3-2. Normalized absorption and luminescence spectra of $1.5 \cdot 10^{-5}$ M aqueous solutions of $\text{Na}_4\{\text{Ru}[\text{Eu}_2\text{bpy-DDTA}_2(\text{H}_2\text{O})_4]_3\}$: (a) 295 K absorption spectrum, (b) 295 K steady-state excitation spectrum (dotted trace) monitored at 625 nm (upwards arrow) and emission spectrum (solid trace) upon excitation at 450 nm (downwards arrow); (c) same as (b) but at 77 K; (d) 295 K gated excitation spectrum (dotted trace) monitored at 614 nm, (upwards arrow) and emission spectrum (solid trace) upon excitation at 293 nm (downwards arrow) recorded with a 0.05 ms delay, (e) 77 K gated excitation spectrum (dotted trace) recorded at 614 nm (upwards arrow) and emission spectrum (solid trace) upon excitation at 450 nm (downwards arrow) recorded with a 0.15 ms delay.

The absorption bands arising on the high-energy side of the spectrum displayed on Figure III.3-2(a), as well as the one peaking at 293 nm, are assigned to ligand-centred (LC) $\pi\pi^*$ transitions.³⁰ The remaining intense bands around 250 and 450 nm (the latter of which being responsible for the deep orange color of the complexes), are attributed to spin-allowed metal-to-ligand-charge-transfer ($^1\text{MLCT}$) $d \rightarrow \pi^*$ transitions; the shoulders at 330 and 360 nm are probably the metal-centred (MC) $d \rightarrow d$ transitions. The presence of a second absorption band on the low-energy side of the $^1\text{MLCT}$ transition, i.e. at 530-550 nm, would indicate the

presence of the bis-aqua complexes $\{\text{Ru}[\text{Ln}_2\text{bpy-DTTA}_2(\text{H}_2\text{O})_4]_2\}^{2-}$,³⁰ which is not the case here.

Table III.3-1. Transition wavelengths and energies determined from the spectra presented in Figure III.3-2 and lifetimes (τ_{obs}) of $\text{Eu}({}^5\text{D}_0)$.

λ [nm]	λ^{-1} [cm^{-1}]	Assignment	τ_{obs} [ms]
< 200	> 50000	bpy LC $\tau \rightarrow \tau^*$	
215	46512	bpy LC $\tau \rightarrow \tau^*$	
247	40486	$[\text{Ru}(\text{bpy})_3]^{2+}$ MLCT $d \rightarrow \tau^*$	
256	39063	$[\text{Ru}(\text{bpy})_3]^{2+}$ MLCT $d \rightarrow \tau^*$	
293	34130	bpy LC $\tau \rightarrow \tau^*$	
330	30303	Ru^{2+} MC $d \rightarrow d$	
360	27778	Ru^{2+} MC $d \rightarrow d$	
400	25000	$[\text{Ru}(\text{bpy})_3]^{2+ 1}$ MLCT $d \rightarrow \tau^*$	
430	23256	$[\text{Ru}(\text{bpy})_3]^{2+ 1}$ MLCT $d \rightarrow \tau^*$	
462	21645	$[\text{Ru}(\text{bpy})_3]^{2+ 1}$ MLCT $d \rightarrow \tau^*$	
584	17123	$[\text{Ru}(\text{bpy})_3]^{2+ 3}$ MLCT $d \rightarrow \tau^*$	
625	16000	$[\text{Ru}(\text{bpy})_3]^{2+ 3}$ MLCT $d \rightarrow \tau^*$	
660	15151	$[\text{Ru}(\text{bpy})_3]^{2+ 3}$ MLCT $d \rightarrow \tau^*$	
680	14706	$[\text{Ru}(\text{bpy})_3]^{2+ 3}$ MLCT $d \rightarrow \tau^*$	
578	17301	$\text{Eu}({}^5\text{D}_0 \rightarrow {}^7\text{F}_0)$	
588	17007	$\text{Eu}({}^5\text{D}_0 \rightarrow {}^7\text{F}_1)$	
594	16835	$\text{Eu}({}^5\text{D}_0 \rightarrow {}^7\text{F}_1)$	0.04 ± 0.001 (295 K)
614	16287	$\text{Eu}({}^5\text{D}_0 \rightarrow {}^7\text{F}_2)$	
621	16103	$\text{Eu}({}^5\text{D}_0 \rightarrow {}^7\text{F}_2)$	0.64 ± 0.001 (77 K)
687	14556	$\text{Eu}({}^5\text{D}_0 \rightarrow {}^7\text{F}_4)$	
695	14388	$\text{Eu}({}^5\text{D}_0 \rightarrow {}^7\text{F}_4)$	

Steady-state excitation of solutions of the three Ln complexes at 295 K and 450 nm (see downwards arrow in Figure III.3-2(b)) into the $[\text{Ru}(\text{bpy})_3]^{2+ 1}$ MLCT absorption band leads to the emission spectrum presented in Figure III.3-2(b) (solid trace). The broad and intense emission band extending from 550 to nearly 850 nm with a peak and a shoulder at 625 and 660 nm, respectively, is due to transitions from $[\text{Ru}(\text{bpy})_3]^{2+ 3}$ MLCT excited states to the $\text{Ru}({}^1\text{A}_1)$ ground state.³¹ When monitoring the $[\text{Ru}(\text{bpy})_3]^{2+ 3}$ MLCT emission at 625 nm (see upwards arrow in Figure III.3-2(b)) the excitation spectrum closely follows the absorption spectrum (Figure III.3-2(a)(b)).

Upon cooling an aqueous solution of $\{\text{Ru}[\text{Eu}_2\text{bpy-DTTA}_2(\text{H}_2\text{O})_4]_3\}^{4-}$ 1.5×10^{-5} M to 77 K, a dramatic change is observed in the emission spectrum in terms of band shapes and positions (see solid trace, Figure III.3-2(c)) with respect to the corresponding room-temperature data: the 77 K spectrum is blue-shifted, with maxima at 584 nm and 625 nm with an shoulder around 680 nm. In addition, a sharp band is observed at 614 nm being assigned to the $\text{Eu}({}^5\text{D}_0 \rightarrow {}^7\text{F}_2)$ transition.

When monitoring the $[\text{Ru}(\text{bpy})_3]^{2+}$ ${}^3\text{MLCT}$ emission of an aqueous solution of $\text{Na}_4\{\text{Ru}[\text{Eu}_2\text{bpy-DTTA}_2(\text{H}_2\text{O})_4]_3\}$ 1.5×10^{-5} M at 625 nm, the excitation spectrum at 77 K again closely matches the absorption spectrum (Figure III.3-2(a)(c)), indicating no drastic change of the $[\text{Ru}(\text{bpy})_3]^{2+}$ absorption properties between 77 K and 295 K.

The ruthenium(II) tris(bipyridine) complex is usually considered as being essentially photochemically inert towards ligand substitution at room temperature.¹⁵ the quantum yield of $[\text{Ru}(\text{bpy})_3]$ disappearance in aqueous solution lies in the range $10^{-5} - 10^{-3}$, depending on pH and temperature. A detailed mechanism for the ligand photo-substitution reaction has been proposed by Durham and al.:¹⁶ thermally activated formation of a MC excited state leads to the cleavage of a Ru-N bond with subsequent formation of a five-coordinate square pyramidal species. When coordinating anions are present, as in the chloride salt, an hexacoordinate monodentate bipyridyl species can lose one bpy ligand upon formation of $[\text{Ru}(\text{bpy})_2\text{X}_2]$, or by a self-annealing process (chelate ring closure), with reformation of $[\text{Ru}(\text{bpy})_3]$. The self-annealing protective step has been shown to be favored in aqueous solution.¹⁶ In our case, due to the presence of polyamino-carboxylate complexed by lanthanides, steric hindrance should disfavour the formation of the 5-coordinate species and no change of the spectra has been observed after illumination.

III.3.3 Sensitized Eu luminescence

The weak and sharp $\text{Eu}({}^5\text{D}_0 \rightarrow {}^7\text{F}_2)$ emission band observed at 614 nm in the steady-state emission spectrum at 77 K (Figure III.3-2(c)) is masked by the broad and much stronger $[\text{Ru}(\text{bpy})_3]^{2+}$ ${}^3\text{MLCT}$ emission extending from 550 to nearly 800 nm. Fortunately, the luminescence lifetime of the $\text{Eu}({}^5\text{D}_0)$ excited state is several orders of magnitude longer compared to that of the ${}^3\text{MLCT}$ excited state of $[\text{Ru}(\text{bpy})_3]^{2+}$, which lies in the μs range.^{32, 33}

Thus, the $\text{Eu}({}^5\text{D}_0 \rightarrow {}^7\text{F}_J)$ emission spectrum can be unraveled by means of time-gated emission spectroscopy, i.e. upon enforcing an appropriate delay time (here 0.05 ms) between the excitation pulse and detection of the emission. This method has been applied to the solution of $\text{Na}_4\{\text{Ru}[\text{Eu}_2\text{bpy-DTTA}_2(\text{H}_2\text{O})_4]_3\}$ $1.5 \cdot 10^{-5}$ mM in H_2O and the resulting room-temperature spectrum obtained under excitation at 293 nm (maximum of the bpy $\pi\pi^*$ absorption band) is displayed on Figure III.3-2(d). It exhibits several sharp bands, which can unambiguously be attributed to $\text{Eu}({}^5\text{D}_0 \rightarrow {}^7\text{F}_J, J = 0-4)$ transitions.

The excitation spectrum (dotted trace, Figure III.3-2(d)) obtained under monitoring the $\text{Eu}({}^5\text{D}_0 \rightarrow {}^7\text{F}_2)$ emission band at 614 nm, resembles the absorption spectrum of Figure III.3-2(a), except for the relative band intensities. In the excitation spectrum, the ligand-centred (LC) transition around 293 nm is much more intense with respect to the ${}^1\text{MLCT}$ band around 450 nm. This observation is in line with the fact that at 295 K no $\text{Eu}({}^5\text{D}_0 \rightarrow {}^7\text{F}_J)$ luminescence could be measured upon excitation of the $[\text{Ru}(\text{bpy})_3]^{2+}$ ${}^1\text{MLCT}$ excited state(s) at 450 nm. This indicates that at room temperature, there is either no $[\text{Ru}(\text{bpy})_3]^{2+} \rightarrow \text{Eu}^{3+}$ energy transfer and/or very efficient non-radiative quenching of the $\text{Eu}({}^5\text{D}_0 \rightarrow {}^7\text{F}_J)$ luminescence (Figure III.3-3).

However, the situation is different at 77 K, where excitation at 450 nm into the $[\text{Ru}(\text{bpy})_3]^{2+}$ ${}^1\text{MLCT}$ absorption band leads to the $\text{Eu}({}^5\text{D}_0 \rightarrow {}^7\text{F}_J)$ emission spectrum (Figure III.3-2(e)) when a time delay 0.15 ms is enforced. In addition, the excitation spectrum obtained upon monitoring the hypersensitive ${}^5\text{D}_0 \rightarrow {}^7\text{F}_2$ transition (dotted trace, Figure III.3-2(e)) closely matches the absorption spectrum, even in terms of relative band intensities. The similarities in the two excitation spectra recorded at 295 and 77 K prove that the sharp-line emission occurs through excitation of the $[\text{Ru}(\text{bpy})_3]^{2+}$ unit and is not due to other species present in the sample at trace levels.

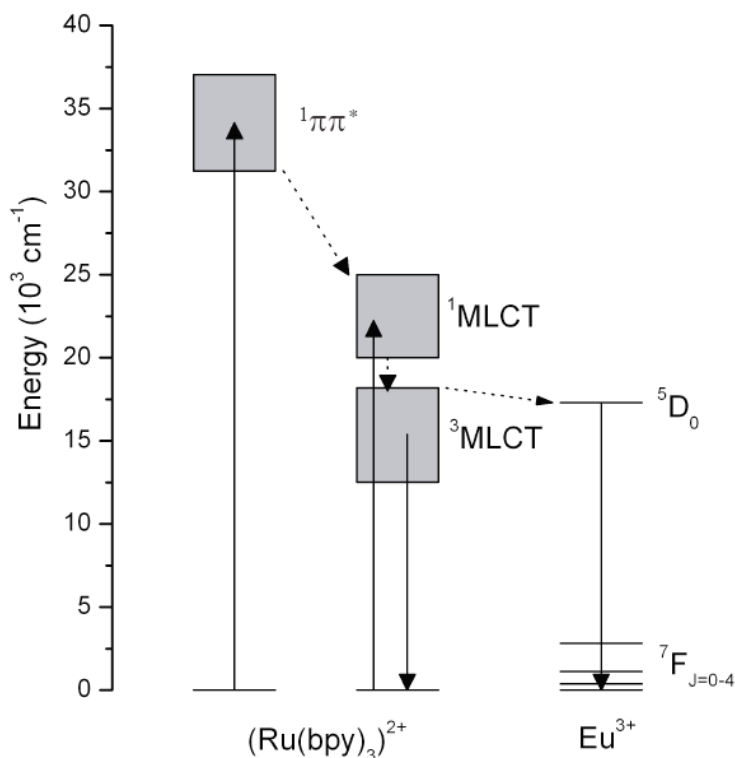


Figure III.3-3. Energy diagram accounting for the most important pathways of energy transfer in aqueous solutions of $\text{Na}_4\{\text{Ru}[\text{Eu}_2\text{bpy-DDTA}_2(\text{H}_2\text{O})_4]_3\}$.

The most straightforward explanation for the observation of $\text{Eu}(^5\text{D}_0)$ luminescence at 77 K and not at 295 K is a decrease in the efficiency of non-radiative quenching processes upon lowering the temperature. Additionally, the blueshift of the emission spectrum of the $[\text{Ru}(\text{bpy})_3]^{2+}$ donor upon cooling leads to an increased spectral overlap¹ with the $\text{Eu}(^7\text{F}_J \rightarrow ^5\text{D}_0)$ absorption spectrum of the acceptor. Unfortunately, the latter could not be measured due to the too small molar absorption coefficients of these transitions.

To gain more information about the quenching of the $\text{Eu}(^5\text{D}_0)$ luminescence by its chemical environment at 295 K and at 77 K, the luminescence lifetime of $\text{Na}_4\{\text{Ru}[\text{Eu}_2\text{bpy-DDTA}_2(\text{H}_2\text{O})_4]_3\}$ in H_2O was determined upon monitoring the maximum of the $\text{Eu}(^5\text{D}_0 \rightarrow ^7\text{F}_2)$ emission band at 614 nm. At room temperature, excitation was into the ligand $\pi\pi^*$ absorption at 293 nm while at 77 K the complex was excited into the $[\text{Ru}(\text{bpy})_3]^{2+}$ $^1\text{MLCT}$ absorption at 450 nm. Mono-exponential decays of the europium emission were observed at both temperatures, yielding $\text{Eu}(^5\text{D}_0)$ luminescence lifetimes of 0.40 ± 0.001 ms and 0.64 ± 0.001 ms at 295 K and 77 K, respectively. These values are in agreement with the presence of two water molecules in the first coordination sphere of the Eu^{3+} ions (Figure III.1-1).

III.3.4 ^1H Relaxivity of $\{\text{Ru}[\text{Gd}_2\text{bpy-DTTA}_2(\text{H}_2\text{O})_4]_3\}^{4-}$

The longitudinal ^1H relaxation rates for $\{\text{Ru}[\text{Gd}_2\text{bpy-DTTA}_2(\text{H}_2\text{O})_4]_3\}^{4-}$ were measured as a function of the magnetic field at two temperatures (298 and 310 K) and normalized to millimolar Gd^{3+} concentration to obtain the longitudinal proton relaxivity, r_1 , in $\text{mM}^{-1}\text{s}^{-1}$.³⁴ At NMR frequencies below 100 MHz the relaxivities measured for the Ru-metallostar are slightly higher than those for the Fe-metallostar (Figure III.3-4).¹⁰ Both profiles show a relaxivity hump between 10 and 100 MHz characteristics for slowly rotating molecules. In that frequency range the relaxivities of both metallostars are considerably higher than those observed for the dinuclear complex $[\text{Gd}_2\text{bpy-DTTA}_2(\text{H}_2\text{O})_4]^-$ used as building block for the metallostars.

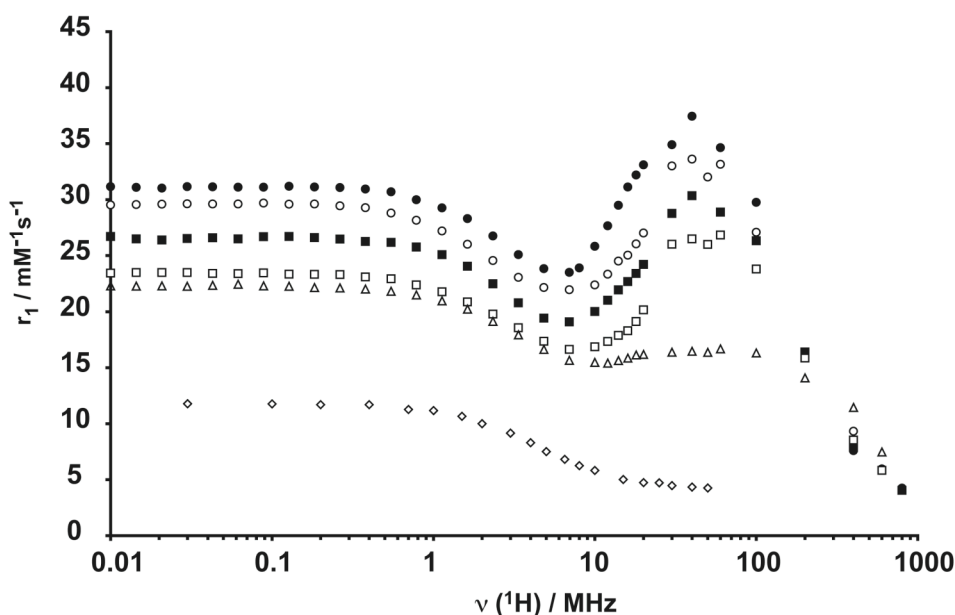


Figure III.3-4. ^1H NMRD profiles and of (●) $\{\text{Ru}[\text{Gd}_2\text{bpy-DTTA}_2(\text{H}_2\text{O})_4]_3\}^{4-}$ at 25°C, (○) $\{\text{Fe}[\text{Gd}_2\text{bpy-DTTA}_2(\text{H}_2\text{O})_4]_3\}^{4-}$ at 25°C, (■) $\{\text{Ru}[\text{Gd}_2\text{bpy-DTTA}_2(\text{H}_2\text{O})_4]_3\}^{4-}$ at 37°C, (□) $\{\text{Fe}[\text{Gd}_2\text{bpy-DTTA}_2(\text{H}_2\text{O})_4]_3\}^{4-}$ at 37°C, (△) $[\text{Gd}_2\text{bpy-DTTA}_2(\text{H}_2\text{O})_4]^{2-}$ at 25°C and (◇) $[\text{GdDOTA}(\text{H}_2\text{O})]^-$ at 25°C.

The slight differences in the NMRD profiles of the metallostars cannot be explained by inaccurate gadolinium concentrations, because its amplitude varies with magnetic field and temperature. The slightly lower relaxivity for $\{\text{Fe}[\text{Gd}_2\text{bpy-DTTA}_2(\text{H}_2\text{O})_4]_3\}^{4-}$ suggests that the iron-containing metallostar solution might contain a small amount of the bis-complex $\{\text{Fe}[\text{Gd}_2\text{bpy-DTTA}_2(\text{H}_2\text{O})_4]_2\}^{2-}$ in solution, having faster rotation correlation times τ_R and

different electronic relaxation. In this case the observed r_1 would be the weighted mean of a small contribution due to the bis-complex and a major contribution due to the tris-complex.

Livramento et al.¹⁰ tried to perform a combined analysis of multi frequency ^{17}O and ^1H relaxation data on $\{\text{Fe}[\text{Gd}_2\text{bpy-DTTA}_2(\text{H}_2\text{O})_4]_3\}^{2-}$ using Solomon-Bloembergen-Morgan (SBM) theory³⁵⁻³⁷ together with the Lipari-Szabo model-free approach^{38, 39} for internal rotation (SBM-LS). In this approach the electron spin relaxation rates, $1/T_{1e}$, are due to the time dependent transient zero-field-splitting (ZFS) and no static ZFS is considered. However, a simultaneous analysis of ^{17}O and ^1H relaxation data was not possible; in particular, an acceptable fit of the ^{17}O transverse relaxation rates seemed to be incompatible with the low-field NMRD data.^{10, 34, 40}

In a first attempt, we analyzed the NMRD profiles at 25° C of both $\{\text{Ru}[\text{Gd}_2\text{bpy-DTTA}_2(\text{H}_2\text{O})_4]_3\}^{4-}$ and $\{\text{Fe}[\text{Gd}_2\text{bpy-DTTA}_2(\text{H}_2\text{O})_4]_3\}^{4-}$ using the same SBM-LS approach. We fixed the distances between the electron spin and the nuclear spin to the usual values of $r_{\text{GdH}} = 3.1 \text{ \AA}$ (first sphere water protons) and $a_{\text{GdH}} = 3.5 \text{ \AA}$ (outer sphere water protons). To reduce the number of fitted parameters further we fixed the constant for intermolecular translational diffusion to $D_{\text{diff}}^{298} = 2.5 \times 10^{-9} \text{ m}^2 \text{ s}^{-1}$ and the exchange rate constant for first sphere water molecules to $k_{\text{ex}}^{298} = 8.3 \times 10^6 \text{ s}^{-1}$, a value that is common for DTTA complexes.^{10, 11, 41, 42} Only five parameters are left for fitting the NMRD profiles: the global and local rotational correlation times τ_g^{298} and τ_l^{298} , respectively, the transient ZFS parameter, Δ_i^2 and its correlation time, τ_v^{298} , and the order parameter S^2 . It can clearly be seen from the fitted curves (Figure III.3-5 and Figure III.3-6, dashed lines) that SBM theory is not able to reproduce the flat dispersion at Larmor frequencies between 0.5 and 8 MHz. Relaxivities at high resonance frequencies ($\geq 40 \text{ MHz}$) are however well reproduced by the SBM-LS approach.

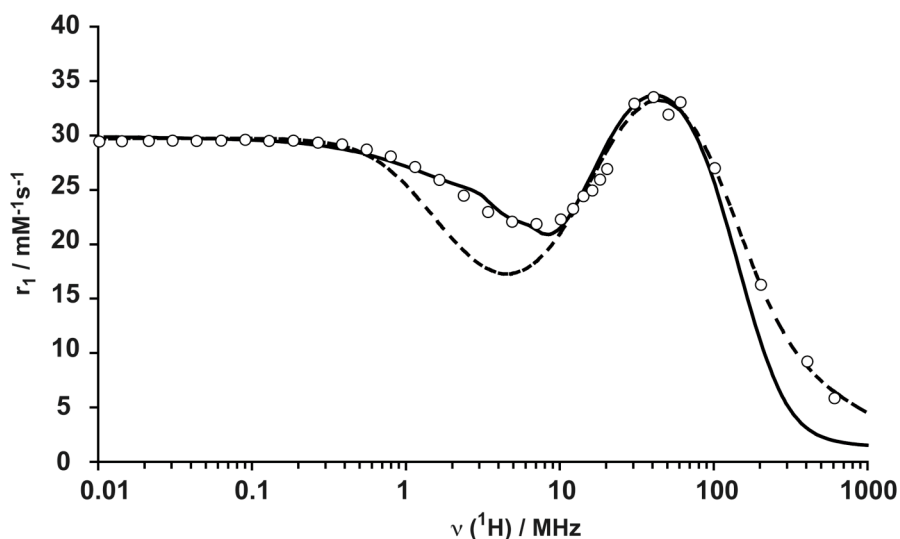


Figure III.3-5. ^1H NMRD profiles at 25°C of $\{\text{Ru}[\text{Gd}_2\text{bpy-DTTA}_2(\text{H}_2\text{O})_4]_3\}^{4-}$. The lines represent the least-squares fitting of all data points following S-B-M theory with Lipary-Szabo (- - -) and Florence approach (solid trace).

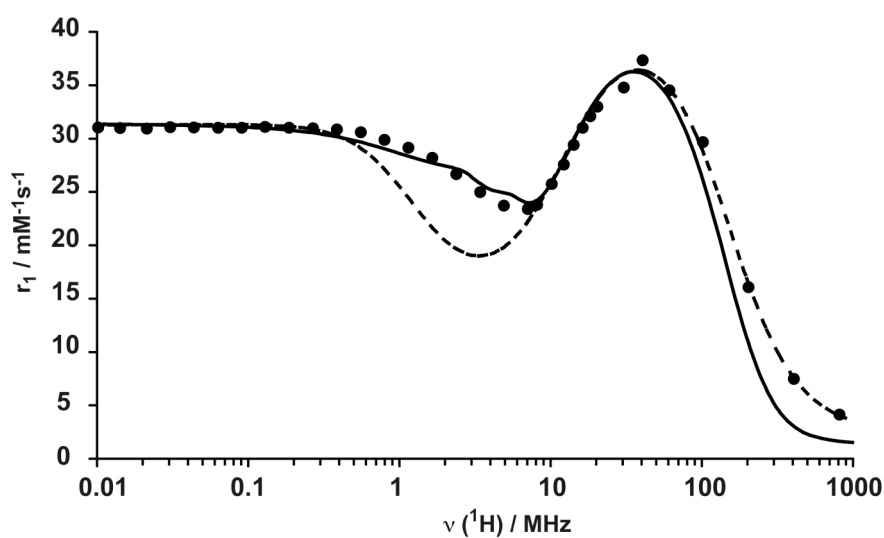


Figure III.3-6. ^1H NMRD profiles at 25°C of $\{\text{Fe}[\text{Gd}_2\text{bpy-DTTA}_2(\text{H}_2\text{O})_4]_3\}^{4-}$. The lines represent the least-squares fitting of all data points following S-B-M theory with Lipary-Szabo (- - -) and Florence approach (solid trace).

In a second attempt we used the approach of Bertini et al.²⁷ and Kruk et al.²⁸ also called the "modified Florence method".⁴³ This method includes a transient and a static ZFS, and assumes a slow reorientation of the paramagnetic complex and a lack of correlation between the rotation and translation of the complex and the electron spin dynamics.²⁸ The electron spin

relaxation uses the pseudo-rotation model for the modulation of the transient ZFS and is described by a Redfield formulation. It has been shown that the modified Florence method is well-suited for fitting experimental NMRD profiles for slowly-rotating complexes of Gd^{3+} .⁴³

Table III.3-2. Parameters at 298 K obtained for $\{\text{Ru}[\text{Gd}_2\text{bpy-DTTA}_2(\text{H}_2\text{O})_4]_3\}^{4-}$ and $\{\text{Fe}[\text{Gd}_2\text{bpy-DTTA}_2(\text{H}_2\text{O})_4]_3\}^{4-}$ complexes from fitting ^1H NMRD data (k_{ex}^{298} has been fixed).

	$\{\text{Fe}^{\text{II}}[\text{Gd}_2\text{bpy-DTTA}_2(\text{H}_2\text{O})_4]_3\}^{4-}$		$\{\text{Ru}^{\text{II}}[\text{Gd}_2\text{bpy-DTTA}_2(\text{H}_2\text{O})_4]_3\}^{4-}$	
	SBM with Lipari-Szabo	modified Florence	SBM with Lipari-Szabo	modified Florence
k_{ex}^{298} (10^6 s^{-1})	8.3 (fixed)	8.3 (fixed)	8.3 (fixed)	8.3 (fixed)
τ_g^{298} (ps)	1200	832	1120	833
τ_l^{298} (ps)	143	-	59	-
τ_v^{298} (ps)	23	16	28	23
Δ_t^2 (10^{20} s^{-2})	0.17	0.082	0.12	0.051
Δ_s^2 (10^{20} s^{-2})	-	0.982	-	0.580
S^2	0.50	-	0.61	-

The influence of the static ZFS on NMRD profiles depends on its symmetry and its orientation with respect to the Zeeman interaction.^{44, 45} If we limit the description to second-order, the static ZFS parameter Δ_t^2 can be expressed in terms of the axial (D) and rhombic (E) coefficients as $2/3 \times D^2 + 2 \times E^2$.⁴⁶ For simplicity we assumed axial symmetry ($E = 0$) and coinciding tensors for the static ZFS and the dipole-dipole interaction. NMRD profiles for both $\{\text{Ru}[\text{Gd}_2\text{bpy-DTTA}_2(\text{H}_2\text{O})_4]_3\}^{4-}$ and $\{\text{Fe}[\text{Gd}_2\text{bpy-DTTA}_2(\text{H}_2\text{O})_4]_3\}^{2-}$ are well reproduced up to 100 MHz (Figure III.3-5 and Figure III.3-6). At higher frequencies the modified Florence approach underestimates the relaxivities because it assumes rigid molecules and neglects internal motion.

The fitted parameters of both analyses are given in Table II.3-2. Because Δ_t^2 and τ_v^{298} from SBM-LS analysis should be considered to be fitting parameters only without specific physical meaning, we will not discuss them. The global rotational correlation times τ_g^{298} are very similar, as expected from the similar size of the metallostars. The small differences in the local correlation times and the order parameters have to be regarded with caution. These

parameters are strongly correlated and essentially defined by the high-field data points. The fitted order parameters S^2 are relatively high indicating fairly rigid complexes.

The rotational correlation times obtained with the modified Florence approach are about 2/3 of τ_g^{298} because, as already mentioned, no internal rotation is considered in this approach. Correlation times due to electron spin relaxation, τ_s , can be calculated in the low field limit from Δ_t^2 and τ_v^{298} .²⁷ Both calculated values, 710 ps (Ru-metallostar) and 635 ps (Fe-metallostar), are smaller than the rotational correlation times τ_r^{298} justifying the use of the modified Florence approach.²⁷ Benmelouka et al.⁴⁴ measured static ZFS parameters on frozen solutions of several DTTA-type Gd^{3+} -complexes. Our Δ_s^2 values (Table III.3-1) are close to those, which can be calculated from D and E values in Table 1 in reference 44 (with Δ_s^2 values in the range $0.87 \times 10^{20} \text{ s}^{-2}$ to $0.92 \times 10^{20} \text{ s}^{-2}$). However, a rhombic distortion from axial symmetry which is close to theoretical maximum ratio of $E/D=1/3$ has been found for frozen solutions. We tried without success to fit the NMRD profiles for both metallostars using this $E/D = 0.3$. One possible explanation for this failure is that at 300 K we observe a mixture of different coordination polyhedra for Gd^{3+} in solution, each having different static ZFS parameters. The distribution at room temperature among these structural isomers can well be different from what is observed at 4 K in frozen solutions. A further problem arises from the assumption that the tensors for static ZFS and for dipole-dipole interaction coincide. There are two water molecules in the first coordination sphere of Gd-DTTA^- and the assumption used can only be strictly valid for one of them. Treating the two inner sphere water molecules differently in the data fitting would lead to an unreasonable number of parameters, even if we assume that the distances r_{GdH} and exchange rate constants k_{ex} are equal.

III.4 CONCLUSION

In this chapter III, we describe the self-assembly of the d/f heptametallic edifices $\{\text{Ru}[\text{Ln}_2\text{bpy-DTTA}_2(\text{H}_2\text{O})_4]_3\}^{4-}$ with $\text{Ln} = \text{Y}^{3+}, \text{Gd}^{3+}, \text{Eu}^{3+}$. Besides the higher stability of the $[\text{Ru}(\text{bpy})_3]^{2+}$ unit compared to its iron(II) analogue, the ruthenium-based metallostar shows interesting photophysical properties in addition to its capacity to act as MRI contrast agent. Structural characterization in solution was achieved by ^1H NMR on the diamagnetic yttrium complex by analyzing the aromatic protons of the bipyridyl unit. The gadolinium complex gives rise to NMRD profiles in accordance with those of the iron-based metallostar.² NMRD profiles of both Ru^{2+} and Fe^{2+} based metallostars have been analysed using SBM theory including a Lipary-Szabo treatment of internal motion and using the modified Florence approach developed for slowly rotating, rigid complexes. Data-analysis showed the incapability of SBM theory to reproduce correctly NMRD profiles between 0.5 and 8 MHz for slowly rotating compounds. Parameters of static ZFS as obtained from the modified Florence method are in reasonable agreement with low temperature EPR results.⁴⁴ Comparison of both methods shows that inclusion of internal motion is necessary to have a correct description of high-frequency relaxivity.

The photophysical data determined for $\text{Na}_4\{\text{Ru}[\text{Eu}_2\text{bpy-DTTA}_2(\text{H}_2\text{O})_4]_3\}$ demonstrate the feasibility of d \rightarrow f visible-sensitized europium $^5\text{D}_0\rightarrow^7\text{F}_J$ luminescence in aqueous solution. This opens the way for the development of bimodal biological art bimodal bioprobes

III.5 ACKNOWLEDGEMENTS

Prof. Jean-Claude Bünzli and Dr. Annina Aebischer are strongly thanked for the very nice luminescence study they performed on the Ru-based metallostar compounds.

Dr. Céline Fellay from the group of Prof. Dyson and Dr. Steve Comby from the group of Prof. Bünzli are acknowledged for her help during the synthesis of the $[\text{Ru}(\text{H}_2\text{O})_6](\text{tos})_2$ and for the absorbance and emission spectra respectively.

Dr. Md. Khaja Nazeeruddin from the group of Prof. Graetzel and Joël Teuscher from the group of Prof. Moser are thanked for their advice for the purification step of the synthesis.

Dr. Alain Borel and Prof. André E. Merbach are thanked for their very useful discussions.

III.6 REFERENCES

1. É. Tóth, L. Helm and A. E. Merbach, in *Metal ions in biological systems*, eds. Sigel, A. and Sigel, H., Marcel Dekker Inc., New York, 2003, vol. 40, Ch. 15.
2. R. A. Poole, C. P. Montgomery, E. J. New, A. Congreve, D. Parker and M. Botta, *Org. Biomol. Chem.*, 2007, **5**, 2055-2062.
3. F. Kielar, G. L. Law, E. J. New and D. Parker, *Org. Biomol. Chem.*, 2008, **6**, 2256-2258.
4. J. C. Bünzli, A. S. Chauvin, C. D. B. Vandevyver, S. Bo and S. Comby, *Ann. N. Y. Acad. Sci.*, 2008, **1130**, 97-105.
5. A. E. Merbach and É. Tóth, in *The Chemistry of Contrast Agents in Medical Magnetic Resonance Imaging*, John Wiley & Sons, Chichester, 2001.
6. P. Caravan, J. J. Ellison, T. J. McMurry and R. B. Lauffer, *Chem. Rev.*, 1999, **99**, 2293-2352.
7. S. Aime, M. Botta and E. Terreno, *Adv. Inorg. Chem.*, 2006, **57**, 173-237.
8. P. Caravan, *Chem. Soc. Rev.*, 2006, **35**, 512-523.
9. J. B. Livramento, C. Weidensteiner, M. I. M. Prata, P. R. Allegrini, C. F. G. C. Geraldes, L. Helm, R. Kneuer, A. E. Merbach, A. C. Santos, P. Schmidt and É. Tóth, *Contrast Med. Mol. Imaging*, 2006, **1**, 30-39.
10. J. B. Livramento, A. Sour, A. Borel, A. E. Merbach and É. Tóth, *Chem. Eur. J.*, 2006, **12**, 989-1003.
11. J. B. Livramento, E. Tóth, A. Sour, A. Borel, A. E. Merbach and R. Ruloff, *Angewandte Chemie, International Edition*, 2005, **44**, 1480-1484.
12. V. Jacques and J. F. Desreux, in *Contrast Agents I*, 2002, vol. 221, pp. 123-164.
13. V. Jacques and J. F. Desreux, *Top. Curr. Chem.*, 2002.
14. J. Van Houten and R. J. Watts, *J. Am. Chem. Soc.*, 1976, **98**, 4853-4858.
15. J. Van Houten and R. J. Watts, *Inorg. Chem.*, 1978, **17**, 3381-3385.
16. B. Durham, J. V. Caspar, J. K. Nagle and T. J. Meyer, *J. Am. Chem. Soc.*, 1982, **104**, 4803-4810.
17. J. C. Bünzli and C. Piguet, *Chem. Soc. Rev.*, 2005, **34**, 1048-1077.
18. J. C. G. Bünzli, *J. Alloys Compd.*, 2006, **408-412**, 934-944.
19. J. C. Bünzli, S. Comby, A. S. Chauvin and C. D. B. Vandevyver, *J. Rare Earth*, 2007, **25**, 257-274.
20. M. Gagliardo, F. Rizzo, M. Lutz, A. Spek, G. Van Klink, A. Merbach, L. De Cola and G. van Koten, *Eur. J. Inorg. Chem.*, 2007, 2853-2861.
21. P. Kadjane, L. Charbonniere, F. Camerel, P. P. Laine and R. Ziessel, in *J Fluoresc*, Editon edn., 2008, vol. 18, pp. 119-129.

22. S. Pope, B. J. Coe, S. Faulkner, E. V. Bichenkova, X. Yu and K. T. Douglas, *J. Am. Chem. Soc.*, 2004, **126**, 9490-9491.
23. P. Bernhard, M. Biner and A. Ludi, *Polyhedron*, 1990, **9**, 1095-1097.
24. C. Ammann, P. Meier and A. E. Merbach, *J. Magn. Reson.*, 1982, **46**, 319-321.
25. D. Corsi, C. Platas-Iglesias, H. van Bekkum and J. Peters, *Magn. Reson. Chem.*, 2001, **39**, 723-726.
26. F. Yerly, *VISUALISEUR/OPTIMISEUR*, EPFL, 2003
27. I. Bertini, J. Kowalewski, C. Luchinat, T. Nilsson and G. Parigi, *J. Chem. Phys.*, 1999, **111**, 5795-5807.
28. D. Kruk, T. Nilsson and J. Kowalewski, *Phys. Chem. Chem. Phys.*, 2001, **3**, 4907-4917.
29. J. Costa, R. Ruloff, L. Burai, L. Helm and A. E. Merbach, *J. Am. Chem. Soc.*, 2005, **127**, 5147-5157.
30. A. Juris, V. Balzani, F. Barigelletti, S. Campagna, P. Belser and A. von Zelewsky, *Coord. Chem. Rev.*, 1988, **84**, 85-277.
31. S. A. McFarland and N. S. Finney, *Chem. Commun. (Cambridge, U. K.)*, 2003, **9**, 388-389.
32. S. Encinas, A. F. Morales, F. Barigelletti, A. M. Barthram, C. M. White, S. M. Couchman, J. C. Jeffery, M. D. Ward, D. C. Grills and M. W. George, *J. Chem. Soc., Dalton Trans.*, 2001, 3312-3319.
33. B. Henderson and G. F. Imbusch, in *Optical Spectroscopy of Inorganic Solids*, ed. Publications, Oxford Science, Oxford, 1989, Ch. 10, pp. 445-504.
34. É. Tóth, L. Helm and A. E. Merbach, in *The Chemistry of Contrast Agents in Medical Magnetic Resonance Imaging*, eds. Merbach, A. E. and Tóth, É., John Wiley & Sons, Chichester, 2001, pp. 45-119.
35. I. Solomon and N. Bloembergen, *J. Chem. Phys.*, 1956, **25**, 261-266.
36. N. Bloembergen, *J. Chem. Phys.*, 1957, **27**, 572-573.
37. N. Bloembergen and L. O. Morgan, *J. Chem. Phys.*, 1961, **34**, 842-850.
38. G. Lipari and A. Szabo, *J. Am. Chem. Soc.*, 1982, **104**, 4546-4559.
39. G. Lipari and A. Szabo, *J. Am. Chem. Soc.*, 1982, **104**, 4559-4570.
40. É. Tóth, L. Helm, K. E. Kellar and A. E. Merbach, *Chem. Eur. J.*, 1999, **5**, 1202-1211.
41. J. Costa, E. Tóth, L. Helm and A. E. Merbach, *Inorg. Chem.*, 2005, **44**, 4747-4755.
42. J. B. Livramento, L. Helm, A. Sour, C. O'Neil, A. E. Merbach and É. Tóth, *Dalton Trans.*, 2008, 1195-1202.
43. J. Kowalewski, D. Kruk and G. Parigi, *Adv. Inorg. Chem.*, 2006, **57**, 41-104.
44. M. Benmelouka, J. Van Tol, A. Borel, M. Port, L. Helm, L. C. Brunel and A. E. Merbach, *J. Am. Chem. Soc.*, 2006, **128**, 7807-7816.
45. T. Nilsson, G. Parigi and J. Kowalewski, *J. Phys. Chem. A*, 2002, **106**, 4476-4488.
46. P. Fries and E. Belorizky, *J. Chem. Phys.*, 2007, **126**.

CHAPTER IV.

DTTA THIOL DERIVATIVES COATED TO GOLD NANOPARTICLES (DTNP)

TABLE OF CONTENTS CHAPTER IV

<u>IV.1</u>	<u>INTRODUCTION</u>	<u>107</u>
<u>IV.2</u>	<u>EXPERIMENTAL SECTION</u>	<u>111</u>
IV.2.1	SYNTHESIS OF LANTHANIDE FUNCTIONALIZED GOLD NANOPARTICLES (LN-DtNP)	111
IV.2.2	TRANSMISSION ELECTRON MICROSCOPY (TEM, STEM/EDX)	114
IV.2.3	DYNAMIC LIGHT SCATTERING (DLS)	114
IV.2.4	INDUCTIVELY COUPLED PLASMA-MASS SPECTROMETRY (ICP-MS)	114
IV.2.5	BULK MAGNETIC SUSCEPTIBILITY	116
IV.2.6	¹ H RELAXIVITY	116
IV.2.7	MOLECULAR MODELING	117
<u>IV.3</u>	<u>RESULTS AND DISCUSSION</u>	<u>118</u>
IV.3.1	PARTICLES SIZE DISTRIBUTIONS.	118
IV.3.2	DtNP STRUCTURAL DESCRIPTION	121
IV.3.3	MOLECULAR MODELING	123
IV.3.4	STEM/EDX	125
IV.3.5	ICP/MS	127
IV.3.6	MAGNETIC PROPERTIES	127
IV.3.7	¹ H RELAXIVITY	131
<u>IV.4</u>	<u>CONCLUSION</u>	<u>137</u>
<u>IV.5</u>	<u>ACKNOWLEDGEMENTS</u>	<u>138</u>
<u>IV.6</u>	<u>REFERENCES</u>	<u>139</u>

IV.1 INTRODUCTION

Colloidal and functionalized nanoparticles are presently under intensive study to produce useful tools for molecular diagnosis, therapies, and biotechnology. Several papers reported interesting behavior for nanoparticles as for example a longer vascular half-life than for small molecular agents, suggesting a real potential as contrast agents for medical imaging.¹⁻⁵

Among metallic elements, Pd, Pt, and Au nanoparticles have been widely synthesized because noble metals are easier to reduce than transition metals. In a cluster, noble metal atoms spontaneously form large particles (diameter > 10 nm) to reduce their surface energy. A practical means of preventing this cohesion is to isolate nanoparticles by coating them with protective agents. These chemically synthesized metal nanoparticles can be generally categorized into two subgroups, colloidal clusters and clusters covalently bonded to ligands. Gold clusters have been reported recently with protective agents in colloids such as polyacrylonitrile, polyallyl amine hydrochloride and polyvinyl pyrrolidone,⁶⁻⁹ or covalently stabilized with a mercapto bond such as dodecane thiol.^{10, 11}

Gold nanoparticles are easily functionalized by thiol derivatives, opening multimodal perspectives. As MRI contrast agent, nanoparticles coated with Gd³⁺ chelates present the advantage of offering a rigid core to the contrast agents, minimizing internal degrees of freedom. Another interesting aspect is the high electron density of these objects, promising gold nanoparticles as agent for X-ray spectroscopy. In 2007, Tillement et al.¹² reported multilayer Gd³⁺ chelates capped gold nanoparticles combining magnetic resonance imaging (MRI) and X-ray computed tomography (CT) imaging. They showed that their particles are suited for freely circulating in the blood vessels without undesirable accumulation in the lungs, spleen and liver.

The creation of perfect nanometer-scale crystallites (nanocrystals), identically replicated in almost unlimited quantities, in a state that can be manipulated and understood as pure macromolecular substances, is an ultimate challenge of modern materials research with outstanding fundamental and potential technological consequences.¹³

Bulk Au metal is chemically stable and has diamagnetic properties. However, recent studies revealed that Au nanoparticles can show magnetism at nanoscale (nm). In 1999, Hori et al.¹⁴

presented magnetization of Pd and Au nanoparticles with a diameter of around 3 nm at 4.2 K where poly-N-vinyl-2-pyrrolidone (PVP) was used as protective agents to the metal particles. The data of magnetization of nanoparticles of both elements showed an unexpectedly large magnetic moment suggesting the existence of some spin correlation mechanism in the nanoparticles.

Electronic and magnetic properties induced by close-packed monolayers of thiols on gold were presented in 2003 by Carmeli et al.¹⁵. Particles formed with octadecanethiolated or ethanethiolated molecules self-assembled on gold show a surprisingly large ferromagnetism and the phenomenon can be considered as a new type of magnetism. Charge transfer between the substrate and the adsorbed layer is indicated as the origin of this magnetism.

Direct observation of intrinsic magnetization behavior of Au in thiol-capped gold nanoparticles with permanent magnetism at room temperature was reported in 2004 by Hori et al.⁷ The magnetic moment per Au atom in the particle attains its maximum value in the magnetization-diameter curve at a diameter of about 3 nm. Because Au metal is a typical diamagnetic material, they supposed that the ferromagnetic polarization mechanism is quite different from the ferromagnetism observed in transition metals and the size effect suggests the existence of some spin-correlation effect at the nanoscale.

The origin of orbital magnetism of thiol capped gold films and nanoparticles as a consequence of spin-orbit coupling was discussed in 2005 by Hernando et al.¹⁶ A great difference exists between the magnetic behavior observed for nanoparticles and for thin films for the case of gold capped with thiol groups. For both cases, a large anisotropy can be detected. However, whereas the magnetic moment reaches giant values (10 or even 100 μ_B per atom) for films, it is extremely low (0.01 μ_B per atom) for NPs. There is experimental evidence associating the appearance of magnetic properties with the charge transfer that takes place by thiol bonding. Uncapped gold thin films as well as uncapped gold NPs have been shown to be diamagnetic as bulk gold metal.

An exhaustive characterization of thiol-capped gold nanoparticles (NPs) with two different average particle sizes was presented in 2006 by Guerrero et al.¹⁷ The set of analyzed samples shows microstructures at the nanoscale with different proportions of Au atoms bonded either to S or to Au atoms. It was experimentally shown that the presence of a ferromagnetic-like behavior is associated to the formation of NPs with simultaneous presence of Au–Au and Au–

S bonds. In order to explain such magnetic behavior, they proposed a model based on the spin-orbit coupling so that localized charges and/or spins of the Au-S bonds can trap conduction electrons from Au-Au bonds in orbits.

The preparation, the characterization and the magnetic properties of gold and gold-iron oxide particles prepared in the presence of aqueous solution of thiol functionalized neoglycoconjugates (GNPs) was described in 2006 by De la Fuente et al.¹⁸ Iron-free gold or gold-iron oxide particles with controlled gold-iron ratios were obtained. The average core-size diameters are in the range of 1.5-2.5 nm. They observed a permanent magnetism up to room temperature in the iron-free gold GNPs. This magnetism was not present in the corresponding gold-iron oxide.

An experiment showing that magnetic impurities reduce the ferromagnetic order temperature in thiol-capped Au glyconanoparticles was reported in 2006 by Crespo et al.¹⁹ The spontaneous magnetization of AuFe glyconanoparticles exhibits a fast decrease with temperature that contrasts with the almost constant value of the magnetization observed in Au NPs. Moreover, hysteresis disappears below 300 K. Both features indicate that Fe impurities reduce the high local anisotropy field responsible for the ferromagnetic behavior in Au glyconanoparticles. As a consequence, the amazing ferromagnetism in Au NPs should not be associated with the presence of magnetic impurities.

A direct observation of the intrinsic magnetization behavior of Au in thiol-capped gold nanoparticles with permanent magnetism at room temperature were reported in 2008 by Garitaonandia et al.²⁰ They show that silver and copper nanoparticles synthesized by the same chemical procedure also present room-temperature permanent magnetism. The observed permanent magnetism at room temperature in Ag and Cu dodecanethiol-capped nanoparticles proves that the physical mechanisms associated to this magnetization process can be extended to more elements, opening the way to new and still not-discovered applications and to new possibilities to research basic questions of magnetism.

We present here well-defined thiol-capped gold nanoparticles coated with DTTA derivatives,²¹ complexed with gadolinium(III) and yttrium(III) lanthanides (Gd-DtNP and Y-DtNP). We provide characterization of solutions of gold nanoparticles using TEM, dynamic light scattering (DLS), ICP-MS, STEM coupled EPX analysis and protons relaxation enhancement in water. Relaxivity and bulk magnetic susceptibility measurements have been

used to observe whether there is a significant paramagnetic behavior of the gold core in these DtNP systems.

IV.2 EXPERIMENTAL SECTION

IV.2.1 Synthesis of lanthanide functionalized gold nanoparticles (Ln-DtNP)

All commercial reagents were used as received unless otherwise noted. Compound **3** (Figure IV.2-1) has been synthesized as described in literature.²²

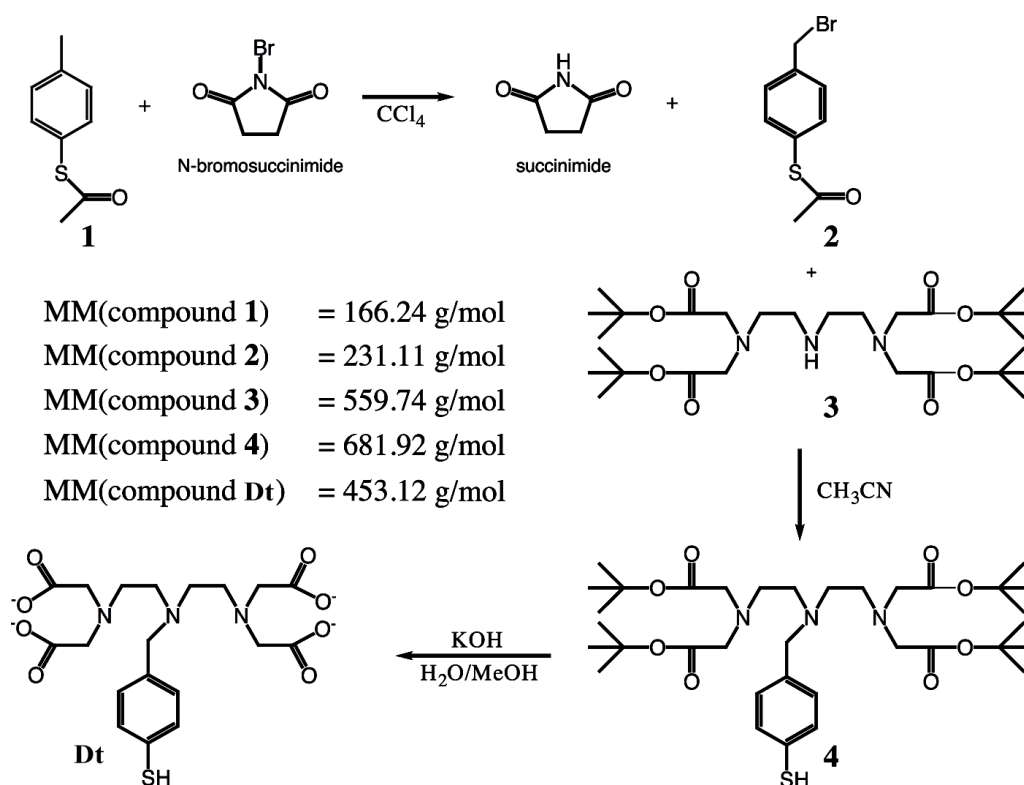


Figure IV.2-1. Synthetic route of the compound Dt.

Synthesis of compound 2

To a solution of compound **1** (*S*-(4-Methylphenyl)thioacetate) (2.75 g, 16.5 mmol) and of *N*-bromosuccinimide (2.90 g, 16.5 mmol) in CCl_4 (41.3 ml), was added AIBN (azobisisobutyronitrile) (23 mg). The reaction mixture was refluxed with stirring over night. The solution was cooled to room temperature and the succinimide removed by filtration. After evaporation of the volatiles, the residue was purified by column chromatography (SiO_2) eluted with petroleum ether / DCM (95:5). Concentration of the eluate gave the bromide **2** as colorless oil, which solidifies in the fridge (2.2 g, 55%). ^1H NMR (δ , CDCl_3): 2.32 (s, 3H),

4.46 (s, 2H), 7.10 (d, 2H, $J = 8.1$ Hz), 7.38 (d, 2H, $J = 8.1$ Hz); ^{13}C NMR (δ , CDCl_3): 30.2, 32.5, 129.5, 129.7, 134.6, 139.0, 193.5.

Synthesis of compound 4

Compound **3** (*N,N'*-[(imino)bis(ethane-2,1-diyl)]bis[*N*-(carboxymethyl)glycine] tetrakis(1,1-dimethylethyl) ester) (3.15 g, 5.62 mmol), was dissolved in dry CH_3CN (393 ml) under argon. Compound **2** (2.13 g, 8.5 mmol) and K_2CO_3 (2.3 g, 17 mmol) were added. The solution was heated to 83°C with stirring for 36 h under argon atmosphere and then cooled to room temperature. The resulting mixture was filtrated, evaporated under reduced pressure and purified by column chromatography on a neutral alumina stationary phase eluted with $\text{CH}_2\text{Cl}_2/\text{MeOH}$ (100: 4). Compound **4** (brown oil) was obtained (594 mg, 0.87 mmol). (yield: 15.4%) ^1H NMR, 400 MHz, CDCl_3 , δ in ppm : 1.42 (s, 36 H); 2.59 (m, 4 H); 2.81 (m, 4 H); 3.39 (s, 8 H); 3.59 (s, 2 H); 7.26 (d, 2 H, $J = 7.34$ Hz); 7.39 (d, 2 H, $J = 7.34$ Hz). MS (ESI): m/z : 681.34 $[\text{MH}]^+$.

Synthesis of compound Dt

The compound **4** (594 mg, 0.87 mmol) was deprotected by saponification with KOH (750 mg, 13.4 mmol) under stirring for 32 h in boiling $\text{H}_2\text{O}/\text{MeOH}$ (50/50) (80 ml). After evaporation, the crude product was acidified at $\text{pH} \approx 2$ and purified by ion-exchange chromatography on Bio-Rad AG 50W-4X resin eluted with a gradient of HCl (1-5 M) and then aqueous NH_3 0.5 M. The pure fractions were evaporated; the resulting yellow oil was dried under vacuum (194 mg, 0.428 mmol) (yield: 49.2%). ^1H NMR, 400 MHz, D_2O , δ in ppm: 2.85 (m, 8 H); 3.39 (m, 8 H); 3.60 (s, 16 H); 3.64 (s, 4 H), 7.31 (d, 4 H, $J = 7.83$ Hz); 7.51 (d, 4 H, $J = 7.82$ Hz). MS (ESI): m/z : 458.23 $[\text{MH}]^+$.

DTTA thiol capped gold nanoparticles (DtNP)

Three batches (DtNP(1); DtNP(2); DtNP(3)) have been synthesized with different HAuCl_4/Dt ratios (Figure IV.2-2).

	HAuCl₄	+	Dt	$\xrightarrow[0^{\circ}\text{C}]{\text{NaBH}_4}$	DtNP
	in CH ₃ OH		in H ₂ O/ acetic acid		
(1)	15.5 μmol		121.0 μmol		DtNP(1)
(2)	15.5 μmol		17.7 μmol		DtNP(2)
(3)	46.5 μmol		171.0 μmol		DtNP(3)

Figure IV.2-2. Quantities of gold and Dt used to synthesise the three DtNP samples.

At 0°C, in methanolic solution of HAuCl₄ (DtNP(1): 6 mg, 15.5 μmol, 2 ml MeOH ; DtNP(2): 6 mg, 15.5 μmol, 2 ml MeOH ; DtNP(3): 6 mg, 15.5 μmol, 2 ml MeOH), an aqueous solution of compound **Dt** (DtNP(1): 55 mg, 121.0 μmol, 18 ml ; DtNP(2): 8 mg, 17.7 μmol, 3 ml ; DtNP(3): 77.5 mg, 171.0 μmol, 29 ml) was added with glacial acetic acid (DtNP(1): 195 μl ; DtNP(2): 32 μl ; DtNP(3): 389 μl). Then, an aqueous solution of NaBH₄ (DtNP(1): 1.95 ml, 0.35 M ; DtNP(2): 320 μl, 0.35 M ; DtNP(3): 3.89 ml, 0.35 M) was added at once. Black-brown flocculates appeared after about 10 mn. Flocculates were recovered by centrifugation and dissolved in pure water.

Ln-DtNP

The DtNP batches have been complexed with gadolinium(III) (Gd-DtNP(1), Gd-DtNP(2) and Gd-DtNP(3)) and yttrium(III) (Y-DtNP(2), and Y-DtNP(3)).

Stock solutions of GdCl₃ and YCl₃ were prepared in double distilled water. Concentrations were determined by complexometric titration with standardized Na₂H₂edta solution using xylenol orange as indicator (H₄edta = ethylene- diaminetetraacetic acid). Solutions of Ln-DtNP were prepared by mixing solutions of LnCl₃ and solutions of the functionalized gold nanoparticles DtNP under stirring at room temperature. An excess of LnCl₃ was used and the pH was adjusted to about 7-7.5 by adding solution of NaOH. Solutions were filtered with a 0.4 μm micropore filters and purified with a size-exclusion column (Sephadex LH20). The absence of free metal was checked in each sample by the xylenol orange test. A part of Y-DtNP(3) and Gd-DtNP(3) solutions have been diluted to obtain solutions Y-DtNP(3)-2 and

Gd-DtNP(3)-2, Gd-DtNP(3)-3 and Gd-DtNP(3)-4 respectively. Solution concentrations were determined with ICP-MS technique (see below).

IV.2.2 Transmission Electron Microscopy (TEM, STEM/EDX)

Visualization of gold nanoparticles was performed with a transmission electron microscope (TEM) JEOL 2010 UHR in the Interdisciplinary Centre for Electron Microscopy (CIME) at EPFL (Lausanne, Switzerland). Samples were prepared by dropping a gold nanoparticle solution onto a carbon-coated copper grid, and allowing the solvent to evaporate at room temperature and standard pressure. TEM images have been treated with Adobe Photoshop software and Feret's diameter distributions of each TEM image have been calculated with ImageJ 1.41k software.²³

Imaging on a scanning transmission electron microscope (STEM) with mapping by energy dispersive X-ray (EDX analysis) was performed on the same samples prepared for TEM spectroscopy. STEM and EDX signals can be obtained simultaneously, allowing direct correlation of image and quantitative EDX data.

IV.2.3 Dynamic light scattering (DLS)

The dynamic light scattering was performed in cubic cells of 0.5 ml with a Zetasizer Nano from Malvern Instruments Ltd. The hydrodynamic diameter distributions were analyzed for the aqueous samples (real part of the refractive index $n = 1.6$, imaginary part of the refractive index $k = 0.1$),²⁴ characterized with a single angle 173° backscatter system incorporating a 633nm laser.

IV.2.4 Inductively Coupled Plasma-Mass Spectrometry (ICP-MS)

Yttrium, gadolinium, and gold concentrations in solution were determined by ICP-MS analysis using an ELAN 6100 DRC mass spectrometer (Perkin Elmer, Norfolk, Canada) interfaced to an Apex sample introduction system (Epond SA, Vevey, Switzerland) at the Institut de Minéralogie et Géochimie, University of Lausanne. The argon flow rates of the

spectrometer amounted to 0.76-0.80, 1.20 and 15 L/min for the nebulizer, auxiliary and main flows, respectively. The ICP RF power was set at 1275 W. The solution uptake rate was close to 100 $\mu\text{L}/\text{min}$. Typical sensitivities obtained during optimization of the spectrometer were in the range of $20\text{-}25 \cdot 10^3$ cps for Mg^{24} , $60\text{-}80 \cdot 10^3$ cps for In^{115} and $70\text{-}90 \cdot 10^3$ cps for U^{238} (1 ppb Perkin Elmer optimization solution). The CeO and Ba^{2+} production rates were below 1.5 and 2.9 %, respectively. The instrumental background measured on masses 8.5 and 220 was below 1-2 cps. The isotopes analyzed in sample solutions were Y^{89} , Rh^{103} , Gd^{157} and Au^{197} . The measurement protocol included a 40 ms dwell time per isotope; peak hopping mode was employed. 8 runs per measurement were performed, with each containing 50 scans of the isotope intensities. Wash times amounted to 60 s for sample solutions and to 120 s after each (re-)standardization. In order to obtain a stable signal, a 60 s sample flush preceded each measurement.

The blank solution contained distilled water used to dilute the sample solutions. Two standards with known concentrations of Y^{3+} , Gd^{3+} and Au^{3+} were prepared from titrated solutions. Standard solution I had 0.997 ppm Y^{3+} , 1.002 ppm Gd^{3+} and 2.220 ppm Au^{3+} , while standard solution II contained 0.111 ppm Y^{3+} , 0.165 ppm Gd^{3+} and 0.240 ppm Au^{3+} (henceforth, all values in ppm or percents correspond to weight concentrations). All blank, standard and sample solutions were acidified by adding 0.2 % HNO_3 and doped with 0.38 ppm Rhodium for internal standardization. In order to minimize the calibration drift of the instrument, the standard solutions were re-measured after each two-sample solution.

To evaluate the analytical uncertainties of our measurements, a repetitive analysis of a sample solution was performed (see Table IV.2-1). Very low concentration (ppb-level) of Y and Gd detected in some solutions, which should have been free of Y and Gd (respectively Gd-DtNP and Y-DtNP), are concerned with contamination issues during standardization as well as analysis of Y- and Au-rich solutions.

Table IV.2-1. Standardization table carried out for the three elements Y(III), Gd(III) and Au(III) on a mixed solution of Gd-DtNP and Y-DtNP, divided in two container (1st place, 2nd place) with the ICP-MS technique.

	1st place			2nd place		
	after standardisation					
	Y [ppm]	Gd [ppm]	Au [ppm]	Y [ppm]	Gd [ppm]	Au [ppm]
1st standardisation	0.564	0.603	1.161	0.566	0.603	1.159
2nd standardisation	0.569	0.598	1.129	0.569	0.597	1.129
3rd standardisation	0.563	0.595	1.126	0.565	0.595	1.141
average	0.565	0.599	1.139	0.567	0.599	1.143
st. Dev. (1 sigma)	0.002	0.003	0.016	0.002	0.003	0.012
RSD (%)	0.435	0.558	1.395	0.266	0.577	1.071

IV.2.5 Bulk magnetic susceptibility

Gd-DtNP and Y-DtNP solutions containing 5% (v/v) of tert-butyl alcohol were placed in a 5 mm NMR tube. The bulk magnetic susceptibility was determined with measurement using an inner co-axial tube containing 10% (v/v) tert-butyl alcohol in D₂O from the frequency shift of the tert-butyl alcohol signal on a Bruker Avance-II 800 NMR spectrometer coupled to an Ultra-Compact UltraShield Plus magnet (18.8 T). The frequency shift of the two resonance signals from the methyl protons of the tert-butyl alcohol, originating from the inner and outer tubes, corrected by 0.091 ppm due the presence of D₂O in the reference, represents the bulk magnetic susceptibility shift.

IV.2.6 ¹H Relaxivity

The 1/T₁ NMRD profiles of Gd-DtNP(1) and Gd-DtNP(3) were obtained at 25.0°C on a Stellar Spinmaster fast field cycling NMR relaxometer (2.35·10⁻⁴ - 0.47 T; proton Larmor frequencies 0.01–20 MHz) equipped with a VTC90 temperature control unit, on Bruker Minispecs (0.71 T (30 MHz), 0.94 T (40 MHz), and 1.41 T (60 MHz)), on a Bruker Avance-200 console connected to 2.35 T (100 MHz), and 4.7 T (200 MHz) cryomagnets and on a Bruker DRX-400 (9.4 T, 400 MHz). The diamagnetic corrections to the ¹H longitudinal relaxation rates were 0.37 s⁻¹ (25.0°C), and 0.33 s⁻¹ (37.0°C). Least-squares fitting of NMRD data was performed with the approach of Bertini et al.²⁵ and Kruk et al.²⁶ also called the

"modified Florence method".²⁷ This method includes a transient and a static ZFS, and assumes a slow reorientation of the paramagnetic complex and a lack of correlation between the rotation and translation of the complex and the electron spin dynamics.²⁶ The electron spin relaxation uses the pseudorotation model for the modulation of the transient ZFS and is described by a Redfield formulation. It has been shown that the "modified Florence method" is well suited for fitting experimental NMRD profiles for slowly-rotating complexes of Gd^{3+} .²⁷

IV.2.7 Molecular modeling

A molecular model of Y-DtNP containing 201 gold atoms and 56 Y-Dt chelates was built using the CAChe program.²⁸ The structure was partially optimized using molecular mechanics (MM3 force field).

IV.3 RESULTS AND DISCUSSION

IV.3.1 Particles size distributions.

The size diameters distributions are determined from transmission electron microscope (TEM) images and dynamic light scattering (DLS) analysis. Figure IV.3-1 shows a distribution of Feret's diameter, which is the greatest distance possible between any two points along the boundary of a region of interest, obtained with a single TEM image.

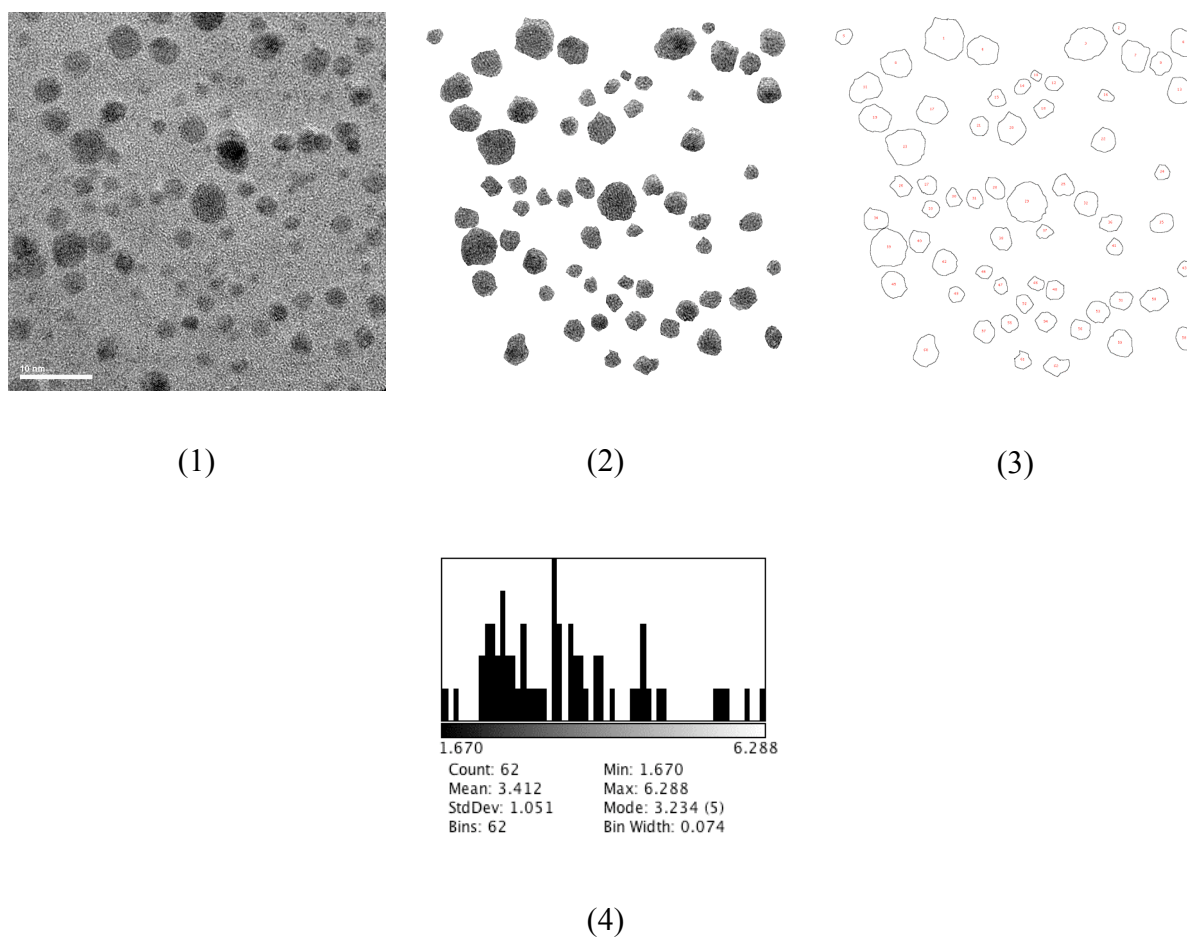
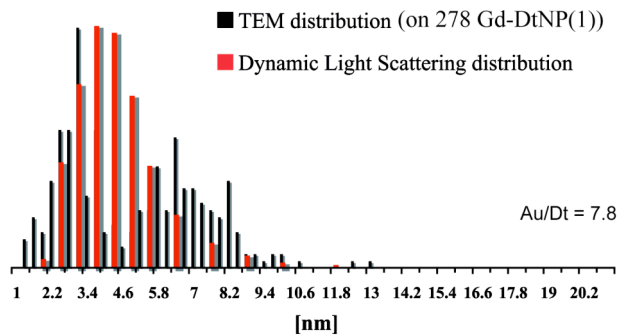


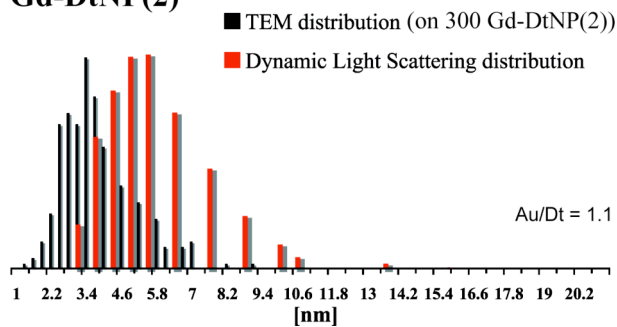
Figure IV.3-1. (1) TEM image. (2) After photoshop treatment erasing the noisy background. (3) After ImageJ 1.41k software treatment. (4) Feret's diameter (greatest distance possible between any two points along the boundary of a region of interest) distribution.

Feret's diameter distributions provided by TEM images are obtained over about 300 particles for Gd-DtNP(1), Gd-DtNP(2) and Y-DtNP(2) and over 674 particles for Gd-DtNP(3) and are compared with DLS mean hydrodynamic diameters distribution in Figure IV.3-2. The two size distribution techniques present good accordance for both Gd-DtNP(1) and Gd-DtNP(3) samples.

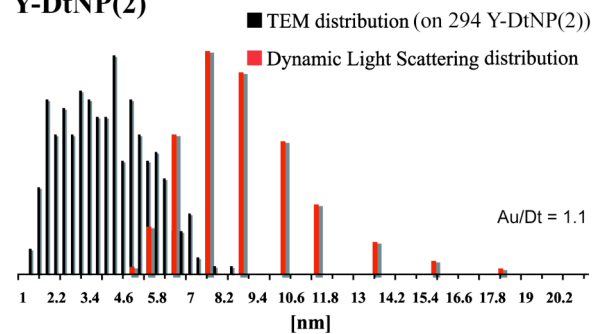
Gd-DtNP(1)



Gd-DtNP(2)



Y-DtNP(2)



Gd-DtNP(3)

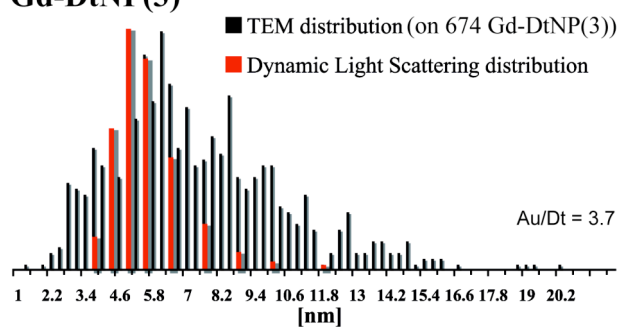


Figure IV.3-2. Diameter size distributions obtained with transmission electron microscope (TEM) images treatment and dynamic light scattering (DLS).

Samples Gd-DtNP(2) and Y-DtNP(2) show DLS diameter distributions shifted to higher values compared to TEM images size distributions. These two samples are both derived from

the solution DtNP(2), which was synthesized with a ratio $Au/Dt = 1.1$ (see Figure IV.3-2). Because the Au/Dt ratios for DtNP(1) and DtNP(3) are respectively 7.8 and 3.7, one can expect that distributions indicate larger nanoparticles in the two DtNP(2) derived samples. The difference between Gd-DtNP(2) and Y-DtNP(2) size distributions come probably from aggregation which occurred during the synthesis. In fact, three aggregation processes might be identified before analysis of the particle size distribution by TEM. The first process can occur during the nanoparticle synthesis. DtNP nanoparticles are synthesized following reduction of gold salt with sodium borohydride ($NaBH_4$) in the presence of thiolated derivatives of DTTA in methanol inducing aggregation and precipitation. The formed DtNP are then dispersed in water. As second, the complexation of DTTA with the lanthanide(III) can induce partial aggregation of nanoparticles. This aggregation can however be considered as reversible by increasing pH of the solution to 7. The third aggregation process can occur when TEM samples are prepared by dropping solutions of gold nanoparticles onto carbon-coated-copper grids and evaporating the solvent to dry.

Even if aggregation can perhaps occur, analyzed TEM images do not show the presence of considerable amounts of aggregates and thus certainly only single nanoparticle size distributions are obtained. Size distribution including formation of nanoparticle clusters in solution is probably better determined with dynamic light scattering (DLS). DLS utilizes time variation of the scattering signal from suspended particles under Brownian motion to extract information on particle size distribution. Multiple scattering is avoided or filtered out by the apparatus used. However, if particle-particle interaction exists, particle motion is not purely Brownian. The apparent particle size computed from the measured diffusion coefficient with the Stokes-Einstein equation can increase or decrease with particle concentration resulting that the size and its distribution are not necessarily the real hydrodynamic size.²⁹ To confirm that such particle-particle interaction do not influence hydrodynamic radius, we performed experiments with concentrated (DtNP-(1)) and diluted (DtNP-(3)) samples, resulting in the same size distributions.

In conclusion, Gd-DtNP(1) and Gd-DtNP(3) present similar diameter size distributions measured with both experimental techniques. Gd-DtNP(2) and Y-DtNP(2) show noticeable aggregation of nanoparticles. The supposed origins of aggregation are from nanoparticle synthesis and lanthanide complexation processes.

IV.3.2 DtNP structural description

State of the art. In 1996, Whetten et al.¹³ reported on series of gold nanocrystals, passivated by self-assembled monolayers of straight-chain alkythiolate molecules. Initial examination of crude mixtures by high-resolution electron microscopy showed particles having all faceted, crystalline gold cores with diameters in the 1.5-3.5 nm range. Fractionation of the crude mixture through cycles of fractional crystallization showed a discrete sequence of energetically optimal fcc structures of a truncated octahedral morphological motif.

In 1997, Cleveland et al.³⁰ determined theoretically via energy-minimization methods and experimentally by synchrotron x-ray diffraction analysis the properties of small gold nanocrystals passivated by a alkylthiolate self assembled monolayer with ratios of S to surface Au atoms in the range of 1:2 to 1:3 and in the 1.5 – 2.5 nm range diameter. Quantitative comparison of the experimental diffraction patterns with patterns calculated from the structures provides evidence for a definite transition from the Marks-type decahedral structures to a particular truncated-octahedral morphology in the 1.7 to 2.0 nm range (≈ 200 atoms).

The structural size-evolution in gold nanoparticles may be described as a sequence of transitions, rather than a continuum of sizes and structures as showed in 1999 by Barnett et al.³¹ First, there are specific “molecular” structures, at the extremely small size range, with equivalent cluster diameter smaller than 1 nm (< 30 atoms). Then there is noncrystallographic order, in particular Marks decahedra structures³² and finally culminating for sizes larger than 2 nm (250 atoms) with the so called crystallites of bulk lattice structure with specific faceted morphologies as truncated octahedra, variants thereof and their twins.

In 2006, Barnard et al.³³ presented a systematic study focused on the variety of face-centered cubic (fcc) gold nanoparticles less than 3 nm in size (13 to 171 atoms) using density functional theory including relativistic effects. They showed that among the equilibrium shape of fcc gold nanoparticles, the cuboctahedral shape is energetically preferred for small sizes, less than 1.5 nm, and the truncated octahedron dominates at larger sizes, over 1.5 nm. They have shown also that small icosahedral and decahedral clusters are actually more likely to exhibit deviations from ideal atomic positions than fcc nanocrystals of comparable size.

Following those information and considering the magic numbers describing the total number of points G_n and the total number of surface point S_n for cuboctahedron (CO) (eq IV.3-1)³⁴

and truncated octahedron (TO) (eq IV.3-2)³⁴ morphology, Table IV.3-1 can be built describing the discrete series of gold nanoparticles that we should face on our study.

$$G_n = \frac{1}{3}(2n+1)(5n^2+5n+3) \text{ and } S_n = 10n^2+2 \quad \text{IV.3-1}$$

$$G_n = 16n^3+15n^2+6n+1 \text{ and } S_n = 30n^2+2 \quad \text{IV.3-2}$$

With n describing the shell number, the particle edge length can be approximated as $n+1$ times gold atomic diameter (270 pm) and the diameter equal to $2/\sqrt{2}$ times the edge length for cuboctahedron and $4/\sqrt{2}$ times the edge length for truncated octahedron shapes.

Table IV.3-1. Magic numbers describing the total number of points G_n and the total number of surface point S_n for cuboctahedron (CO) and truncated octahedron (TO) morphology.

Shell number n	morphology	atoms/edge	G_n	S_n	S_n / G_n	edge length	NP diameter
					%	[nm]	[nm]
1	CO	2	13	12	92	0.54	0.76
2	CO	3	55	42	76	0.81	1.15
1	TO	2	38	32	84	0.54	1.53
2	TO	3	201	122	61	0.81	2.29
3	TO	4	586	272	46	1.08	3.05
4	TO	5	1289	482	37	1.35	3.82
5	TO	6	2406	752	31	1.62	4.58
6	TO	7	4033	1082	27	1.89	5.35
7	TO	8	6266	1472	23	2.16	6.11
8	TO	9	9201	1922	21	2.43	6.87
9	TO	10	12934	2432	19	2.70	7.64
10	TO	11	17561	3002	17	2.97	8.40
11	TO	12	23178	3632	16	3.24	9.16
12	TO	13	29881	4322	14	3.51	9.93
13	TO	14	37766	5072	13	3.78	10.69
14	TO	15	46929	5882	13	4.05	11.46
15	TO	16	57466	6752	12	4.32	12.22
16	TO	17	69473	7682	11	4.59	12.98
17	TO	18	83046	8672	10	4.86	13.75
18	TO	19	98281	9722	10	5.13	14.51
19	TO	20	115274	10832	9	5.40	15.27
20	TO	21	134121	12002	9	5.67	16.04
21	TO	22	154918	13232	9	5.94	16.80
22	TO	23	177761	14522	8	6.21	17.56
23	TO	24	202746	15872	8	6.48	18.33
24	TO	25	229969	17282	8	6.75	19.09
25	TO	26	259526	18752	7	7.02	19.86
26	TO	27	291513	20282	7	7.29	20.62

IV.3.3 Molecular modeling

A partially optimized spatial arrangement of Y-DtNP containing 56 Y-Dt chelates and 201 gold atoms is assessed by molecular mechanics (MM3 field) (Figure IV.3-3).

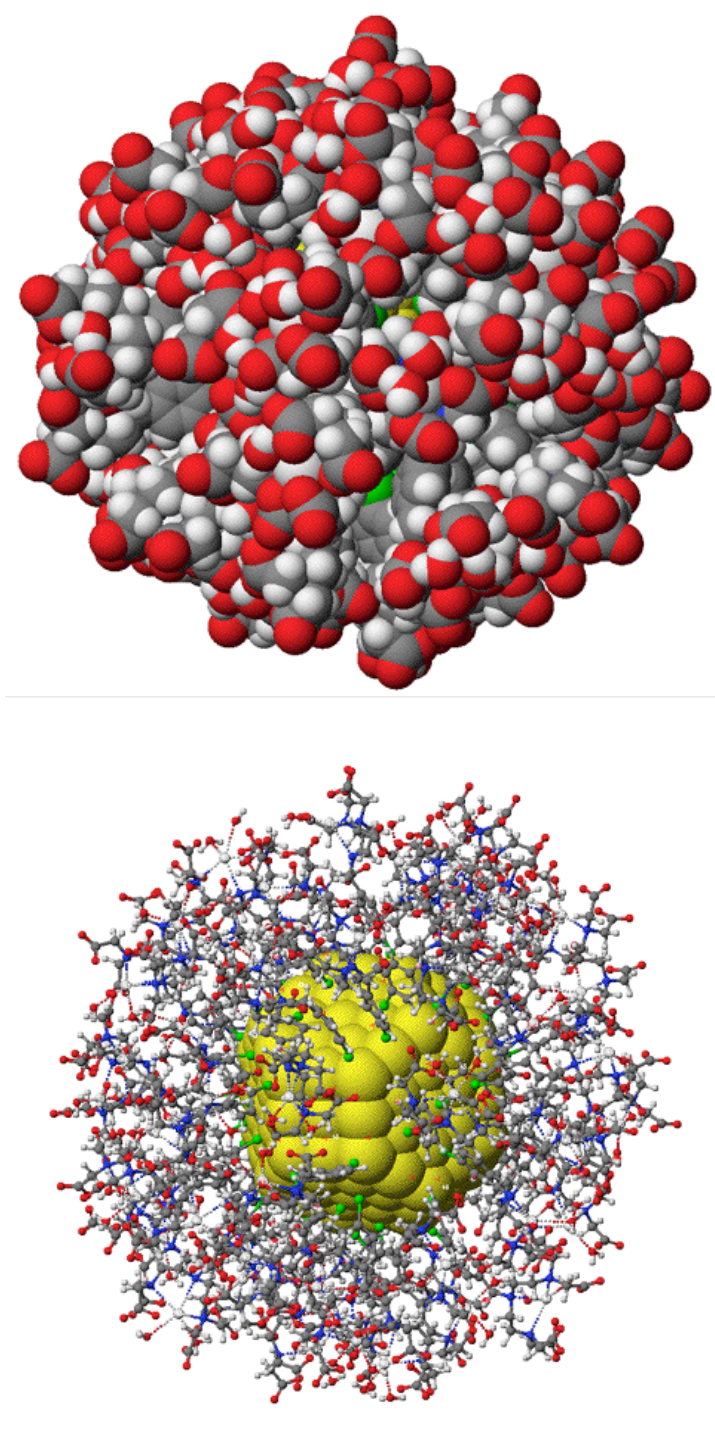


Figure IV.3-3. Partially optimized structure (MM3 force field) of Y-DtNP containing 201 gold atoms, 56 Y-Dt chelates and 112 water molecules.

The gold core, composed of 201 Au atoms, has been built as a truncated octahedron before optimization. The number of Y-Dt complexes around the gold core has been chosen following the free space observed on the gold core surface. We estimate, because of steric hindrance

evidence, that a maximum of about 60 Y-Dt can be expected for a gold core composed of 201 gold atoms ($\text{Au/Y-Dt} = 3.35$).

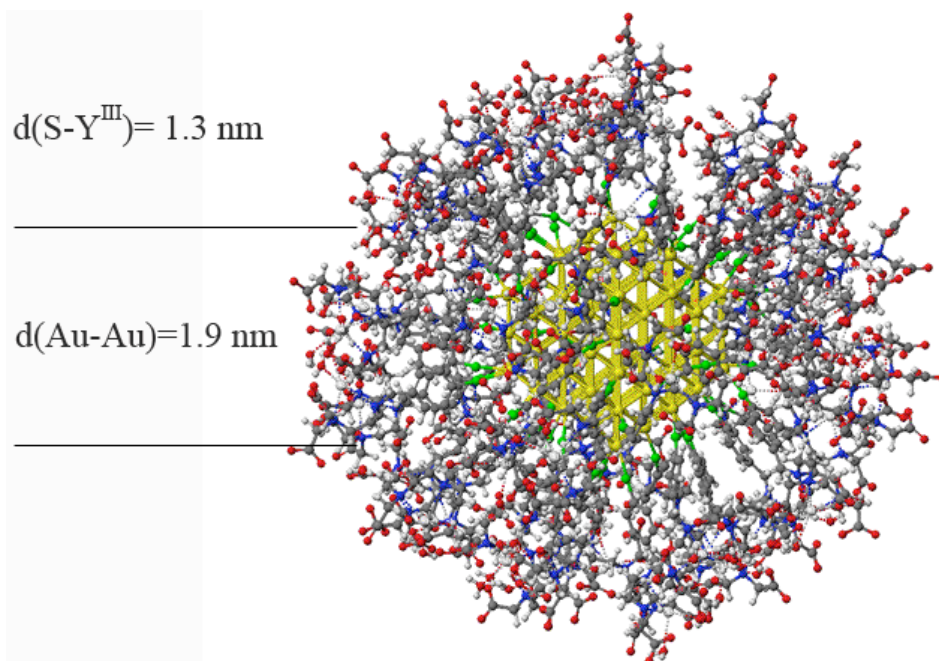
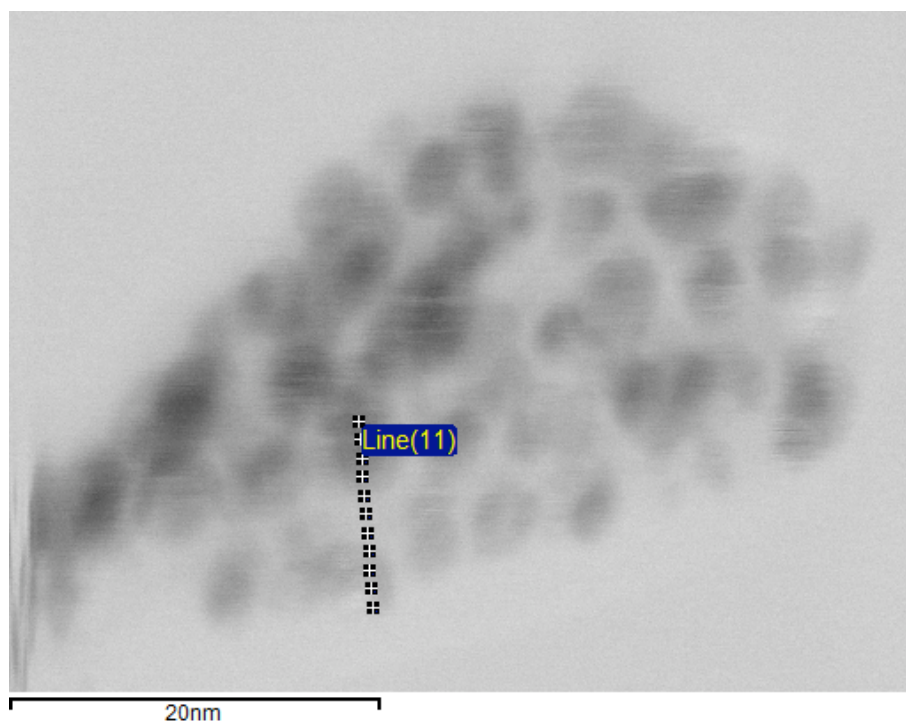


Figure IV.3-4. Rough estimations of the distance between a sulfur and an yttrium ($d(\text{S-Y}^{\text{III}})$) and the diameter of the gold core of a system composed of 56 Y-Dt and 201 gold atoms.

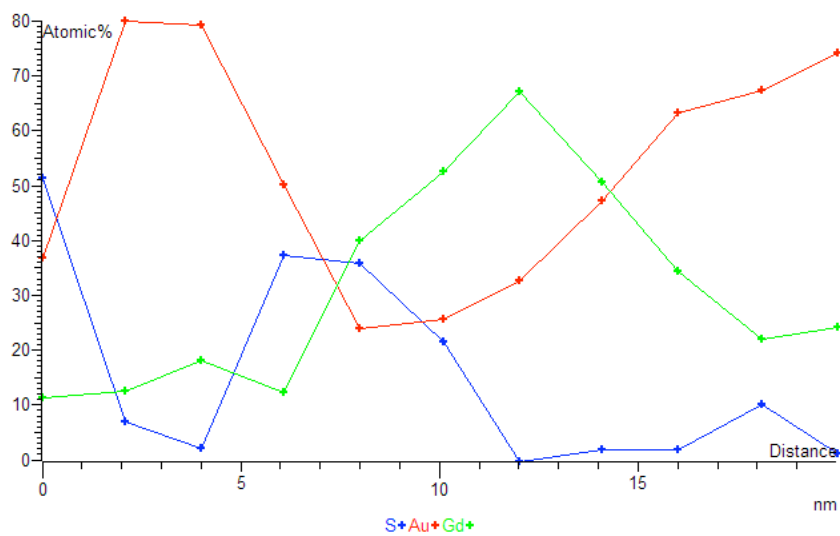
As Figure IV.3-4 shows, a rough estimation of the distance between sulfur linked to gold surface and yttrium(III) can be given: $d(\text{S-Y}^{\text{III}}) = 1.3 \pm 0.3 \text{ nm}$. This distance is mainly determined by the conformation of the methylene bridges linking the DTTA unit on the central nitrogen to the benzene ring. The diameter of the 201 gold atoms core can be as well estimated to $1.9 \pm 0.3 \text{ nm}$. The total diameter of the constructed nanoparticles is about 4.5 nm.

IV.3.4 STEM/EDX

The STEM/EDX results are presented in Figure IV.3-5. This experiment confirms the presence of lanthanide chelates Ln-Dt on the surfaces of gold nanoparticles.



(1)



(2)

Figure IV.3-5. STEM with EDX analysis. (1) STEM images, with the pathway (line 11) describing the EDX analysis result in (2). The lower point of the pathway (line 11) is the starting point 0 in the graph (2).

X rays emitted along line 11 (Figure IV.3-5) after excitation of the encountered atoms by electrons give relative percentages of sulfur, gold and gadolinium elements.

IV.3.5 ICP/MS

Gold, gadolinium and yttrium compositions of the samples derivated from DtNP(1), DtNP(2) and DtNP(3) have been analyzed with ICP/MS and the resulting concentrations are summarized in Table IV.3-2. The Au/Ln ratio for Gd-DtNP(1) hasn't been established for technical reason. As introduced in the experimental part, Gd-DtNP(3)-2, Gd-DtNP(3)-3 and Gd-DtNP(3)-4 are diluted solutions of Gd-DtNP(3), and Y-DtNP(3)-2 is a diluted solution of Y-DtNP(3).

Table IV.3-2. Au, Gd and Y concentrations from ICP-MS analysis.

Sample	Au [μM]	Gd ³⁺ [μM]	Y ³⁺ [μM]	Au/Ln ³⁺
Gd-DtNP(1)	-	378.1 (0.8)	-	-
Gd-DtNP(2)	87 (2)	15.3 (0.2)	-	5.7
Y-DtNP(2)	53 (1)	-	3.4 (0.1)	16.3
Gd-DtNP(3)	709 (10)	200.6 (0.5)	-	3.5
Gd-DtNP(3)-2	428 (7)	120.4 (0.3)	-	3.5
Gd-DtNP(3)-3	214 (4)	55.5 (0.2)	-	3.8
Gd-DtNP(3)-4	126 (2)	34.2 (0.2)	-	3.7
Y-DtNP(3)	1570 (25)	-	824 (1.6)	1.9
Y-DtNP(3)-2	894 (13)	-	479 (1.0)	1.9

Regarding the results presented in Table IV.3-2, one has to keep in mind that the Au/Ln³⁺ ratios are mean values over the solutions. From TEM and DLS experiments, it is known that the size of DtNP particles varies between 1.5 and 15.5 nm, inducing a strong variation of Au/Ln³⁺ ratios for the different particles present in the solutions.

IV.3.6 Magnetic properties

Paramagnetic species induce chemical shifts in nuclear magnetic resonance frequencies via three possible mechanisms, which are the diamagnetic, the hyperfine and the bulk magnetic susceptibility. The shifts provoked by the diamagnetic mechanism are generally small and may be neglected in comparison to the other mechanisms. The hyperfine mechanism, which

has two components, the scalar (contact) contribution and the dipolar (pseudo-contact) contribution, require interaction with the paramagnetic center either through bond (contact) or through space (pseudo-contact). Finally, the shifts induced by the bulk magnetic susceptibility mechanism (Δ_x) originate from the partial alignment of the magnetic moments of the paramagnetic species by the external magnetic field. The Evans method^{35, 36} is a simple technique for the accurate determination of the susceptibility of paramagnetic molecules in solution. It utilizes the bulk magnetic susceptibility shift of an inert compound caused by the presence of a paramagnetic solute. Thus the ^1H NMR chemical shift for an inert reference compound such as t-butyl alcohol can be exploited in order to determine the effective magnetic moment, μ_{eff} , of the paramagnetic species in solution.³⁷ The bulk magnetic susceptibility shift (Δ_x) may be expressed in a good approximation by equ IV.3-3:³⁸

$$\Delta_x [\text{ppm}] = \frac{4\pi \cdot s}{T} \cdot \left(\frac{\mu_{\text{eff}}}{2.84} \right)^2 c [\text{mM}] \cdot 10^3 \quad \text{IV.3-3}$$

The concentration of paramagnetic solute, c , is given in mmol l^{-1} , the factor s is dependent on the shape of the sample and its position in the magnetic field ($s = 1/3$, $-1/6$ and 0 for a cylindrical sample parallel to the main field, a cylindrical perpendicular to the main field and a spherical sample, respectively), T is the absolute temperature and μ_{eff} is the effective magnetic moment for a particular paramagnetic centre.

For a Gd^{3+} paramagnetic ($\mu_{\text{eff}} = 7.94$)³⁹ contribution in a solution at 298.15°C using a NMR sample having a cylinder shape is expressed in equ IV.3-4:

$$\Delta_x (\text{Gd}^{3+}) = \frac{4\pi}{298.15} \cdot \frac{1}{3} \cdot \left(\frac{7.94}{2.84} \right)^2 c \cdot 10^3 = 109.8 \cdot c [\text{mM}] \quad \text{IV.3-4}$$

In considering the gadolinium(III) concentrations determined by ICP-MS and the ^1H NMR chemical shifts induced by the bulk magnetic susceptibility mechanism for the inert reference compound t-butyl alcohol, effective magnetic moments for each solution can be obtained and compared to the effective moment of gadolinium(III) ion. (Table IV.3-3).

Table IV.3-3: ^1H -NMR shift Δ_x observed between the protons of t-butyl alcohol in the reference and in the Gd-DtNP samples at 800 MHz. The gadolinium(III) concentration $[\text{Gd}^{3+}]$ has been measured by ICP-MS.

	T	Δ_x	$[\text{Gd}^{3+}]$	μ_{eff}
	[K]	[ppm]	[mM]	
Gd-dtNP(1)	297.0	0.0397	0.344	8.12
Gd-dtNP(2)	297.9	0.0016	0.015	7.86
Gd-dtNP(3)	297.9	0.0238	0.192	8.43
Gd-dtNP(3)-2	297.9	0.0123	0.116	7.81
Gd-dtNP(3)-3	297.9	0.0072	0.053	8.80
Gd-dtNP(3)-4	297.9	0.0034	0.033	7.64

The measured chemical shifts agree very well with calculated shifts using the effective magnetic moment of Gd^{3+} (Figure IV.3-6). A linear regression of the experimental data results in an effective magnetic moment of the Gd-DtNP of $\mu_{\text{eff}} = 8.19$.

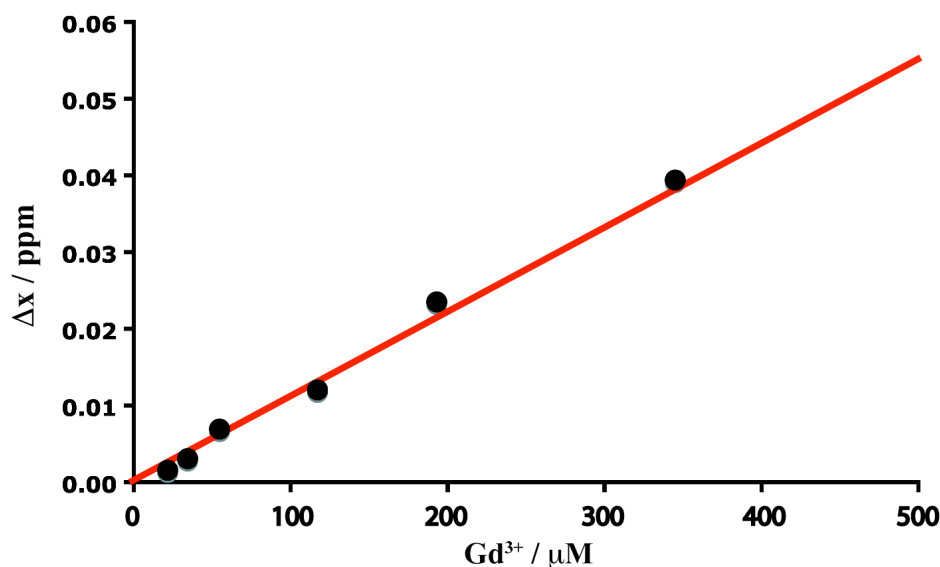


Figure IV.3-6. t-butyl alcohol ^1H NMR chemical shift Δ_x due to the presence of paramagnetic Gd-DtNP (measured at 18.8 T) versus gadolinium(III) concentration obtained from ICP-MS analysis. The red line corresponds to shifts calculated with equ IV.3-4 ($\mu_{\text{eff}} = 7.94$).

The t-butyl alcohol ^1H NMR signal in presence of Y-DtNP samples (Y-DtNP(2), Y-DtNP(3), and Y-DtNP(3)-2) present no significant shift, in respect to t-butyl alcohol ^1H NMR signal in

the internal diamagnetic reference. The effective magnetic moment of Y-DtNP is thus small ($\mu_{\text{eff}} = < 0.2$).

From the results obtained with gadolinium(III) and yttrium(III) DtNP solutions, we can conclude that the gold core of our nanoparticles does not induce a significant effective magnetic moment as it has been expected following the literature.^{7, 14-18, 20} Yamamoto et al.⁴⁰ in a recent review describe results from X-ray magnetic circular dichroism (XMCD) spectroscopy and element-specific magnetization (ESM) experiments allowing revealing intrinsic magnetic polarization in Au nanoparticles with a mean diameter of 1.9 nm. Following the external magnetic field and temperature dependence of the ESM signal, they suggest that magnetization of Au nanoparticles consists of ferromagnetism from surface atoms (obeying the Curie law) and a temperature-independent Pauli-paramagnetic part from the core atoms. The explanation for the observed overall ferromagnetic polarization of the particles is the large ratio of the number of atoms on the surface in respect to the number in the core. But even more important, it has been found that protective agent interacting with the surface play a crucial role for the magnetization of gold nanoparticles: the electronic properties of Au particles strongly depend on the type of binding atoms used. Dodecanthiol-protected gold nanoparticles showed much smaller magnetization than gold nanoparticles protected by polymers such as polyacrylonitril (PAN) and polyallyl amine hydrochloride (PAAHC). The PAAHC polymer has amino (-NH₂) functional group and the interaction between the surface of Au nanoparticles and NH₂ is considered to be weak if compared to strong ligands such as mercapto (-SH) and carbonyl group (-CO). Experimental results suggest that PAAHC-Au can be regarded as a nearly freestanding cluster, and thus the surface magnetic moment survives. The most characteristic property of gold nanoparticles coated with dodecanthiol is the strong covalent bond between the thionic group and Au and thus ligand molecules with strong affinity to the metal tend to quench the magnetic moment at the surface of nanoparticles. However, as we mentioned in the introduction of this chapter IV, distinct magnetization behavior was recently reported for Au nanoparticles protected by molecules with thiol functional group. Yamamoto et al.⁴⁰ attributed these observations to a charge transfer process from the surface to the molecule.

The absence of a marked magnetic moment of gold nanoparticles coated with thiol groups excludes its use as MRI contrast agent *per se* and coating of AuNP with weakly interacting

ligands would lead to freestanding cluster, which would probably cluster in solution. This behavior will exclude its use as MRI contrast agent.

IV.3.7 ^1H relaxivity

Dilution effect

Longitudinal ^1H nuclear spin relaxation rates at 30 MHz and 25°C have been measured for four different samples to determine whether a dilution effect can be observed from the relaxivity, r_1 , of the Gd-DtNP system. An aggregation of nanoparticles at higher concentrations would at the chosen observation frequency lead to an increase in T_1 due to longer rotational correlation times. Measured relaxivities (Table IV.3-4, Figure IV.3-7) are within experimental error independent on the gadolinium concentration. Therefore, no aggregation of the nanoparticles is observed in the concentration range we worked in the Gd-DtNP systems.

Table IV.3-4. Longitudinal relaxation rate T_1 observed at 30 MHz and 25°C and calculated relaxivities r_1 for various gadolinium concentrations.

	Gd^{3+} [μM]	T_1 [ms]	r_1 [$\text{mM}^{-1}\text{s}^{-1}$]
Gd-DtNP(1)	378	42.6	61
Gd-DtNP(2)	15.3	844.6	53
Gd-DtNP(3)	201	82.6	59
Gd-DtNP(3)-2	120	136.1	58

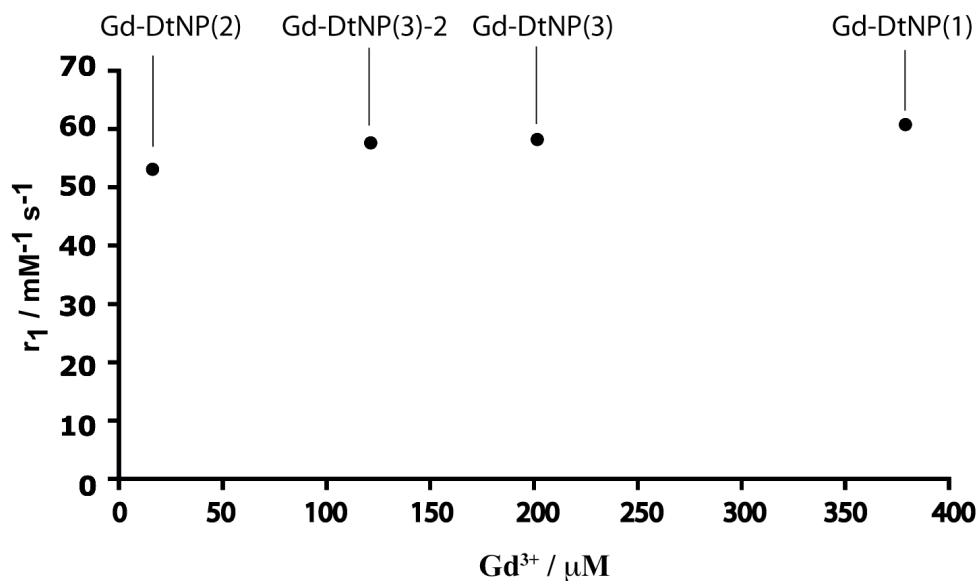


Figure IV.3-7. Measured relaxivities (30 MHz, 25° C) as a function of gadolinium concentration.

Furthermore, different batches from synthesis result in the same relaxivity, which allows us to conclude that Gd-DtNP can be synthesized with good reproducibility at least in respect to r_1 .

¹H nuclear magnetic relaxation dispersion (NMRD)

The NMRD profiles of Gd-DtNP(1) and Gd-DtNP(3) are presented in Figure IV.3-8. Both DtNP batches lead to very similar relaxivities, which are below 200 MHz much higher than that of the Ru metallostar $\{\text{Ru}[\text{Gd}_2\text{bpyDTTA}_2(\text{H}_2\text{O})_4]_3\}^{4+}$ (see chapter III) and the bimetallic compound $[\text{Gd}_2\text{bpy-DTTA}_2(\text{H}_2\text{O})_4]^{2-}$.⁴¹

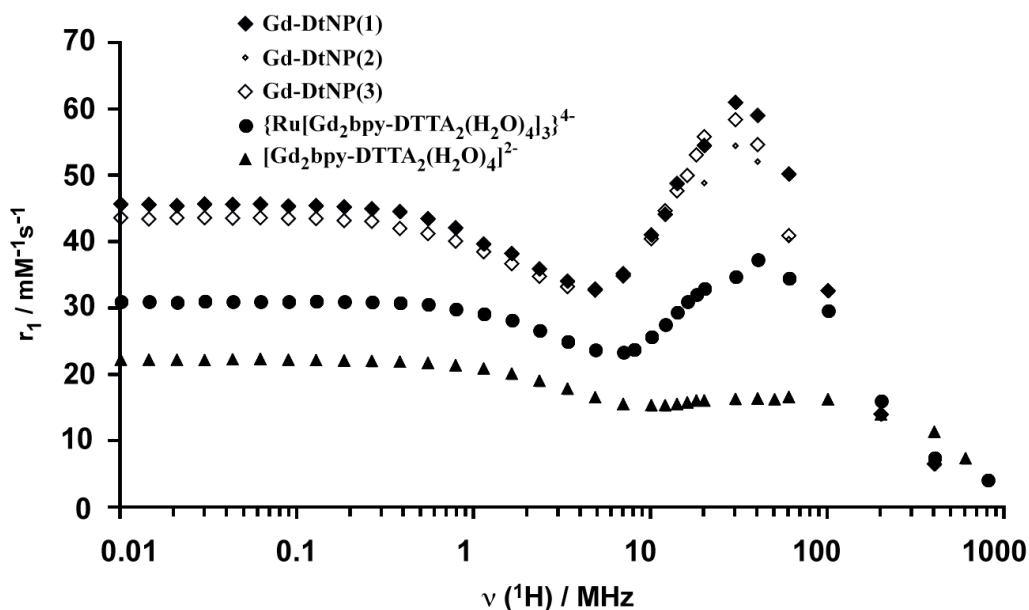


Figure IV.3-8: ^1H nuclear magnetic relaxation dispersion profiles, recorded at 25°C of Gd-DtNP(1), Gd-DtNP(2), Gd-DtNP(3), Ru-based metallostar $\{\text{Ru}[\text{Gd}_2\text{bpy-DTTA}_2(\text{H}_2\text{O})_4]_3\}^{4+}$ and the $[\text{Gd}_2\text{bpy-DTTA}_2(\text{H}_2\text{O})_4]^{2-}$ bimetallic complex.

Several aspects can be considered to understand the high r_1 values. In a first attempt a contribution from the Au-core of the nanoparticle has to be looked at. A high magnetic moment of the gold center would lead to a contribution to relaxivity due to Curie relaxation. This contribution increases with the square of the magnetic field and is of importance only at very high resonance frequencies. From our results of bulk susceptibility measurements (chapter IV.3.6) and from the NMRD profiles in Figure IV.3-8 it can be seen that T_1 -Curie relaxation can be neglected. The only contribution to relaxation enhancement observed for the water protons comes thus from dipolar interaction between the electron spin of Gd^{3+} and first sphere and outer sphere water molecules.

Because the gadolinium chelates are tightly bound to the nanoparticles, we expect a relatively long rotational correlation time and therefore we used the approach developed by Bertini et al.²⁵ and Kruk et al.²⁶ also called the "modified Florence method".²⁷ This method includes a transient and a static ZFS, and assumes a slow reorientation of the paramagnetic complex and a lack of correlation between the rotation and translation of the complex and the electron spin dynamics.²⁶ The electron spin relaxation uses the pseudorotation model for the modulation of the transient ZFS and is described by a Redfield formulation. It has been shown that the

"modified Florence method" is well-suited for fitting experimental NMRD profiles for slowly-rotating complexes of Gd^{3+} .²⁷ NMRD profiles of several compounds with Gd-DTTA chelating units have been previously analyzed which allowed to fix in the fitting process several parameters to reasonable values (see chapter III): the number of inner sphere water molecules, $q = 2$, the exchange rate constant, $k_{ex}^{298} = 8.3 \cdot 10^6 \text{ s}^{-1}$, the Gd-water proton distance for inner sphere water molecules, $r_{GdH} = 3.1 \text{ \AA}$, the closest distance of approach of outer sphere water molecules, $a_{GdH} = 3.5 \text{ \AA}$, the diffusion constant for outer sphere water molecules $D_{diff}^{298} = 2.5 \cdot 10^9 \text{ m}^2 \text{ s}^{-1}$. As can be seen from Figure IV.3-10, the experimental NMRD profile is fitted perfectly even at high frequencies. Because the modified Florence approach uses only a global rotational movement of the particles and does not include internal rotation, significant deviations between experimental and calculated relaxivities are observed with flexible molecules (see chapter III). The relatively good agreement between measured and calculated r_1 values at $\nu > 200 \text{ MHz}$ suggests that Gd-DtNP are very rigid. This high rigidity can either be due to very dense packing of Gd-Dt units at the surface of the Au-core as nicely shown on the molecular model (Figure IV.3-9) or it can be due to interactions between the benzene wings of Dt (π stacking).

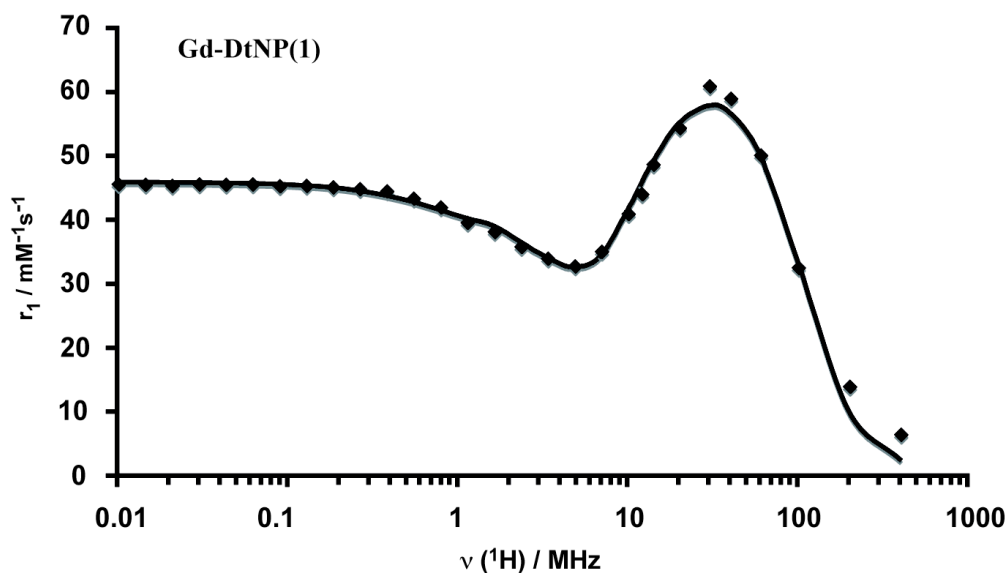


Figure IV.3-10. Gd-DtNP(1) NMRD curve (dotes) and the fit using the modified Florence approach (black line).

Table IV.3-5. Fit parameters of the modified Florence approach for the two systems $\{\text{Ru}^{\text{II}}[\text{Gd}_2\text{bpy-DTTA}_2(\text{H}_2\text{O})_4]_3\}^{4-}$ and Gd-DtNP(1).

	$\{\text{Ru}^{\text{II}}[\text{Gd}_2\text{bpy-DTTA}_2(\text{H}_2\text{O})_4]_3\}^{4-}$	Gd-DtNP(1)
k_{ex}^{298} (10^6 s^{-1})	8.3 (fixed)	8.3 (fixed)
τ_g^{298} (ps)	833	1181
τ_v^{298} (ps)	23.0	22.2
Δ_t^2 (10^{20} s^{-2})	0.051	0.045
Δ_s^2 (10^{20} s^{-2})	0.580	0.387

Due to the (-1) charge of the Gd-Dt units, our Gd-DtNP nanoparticles are strongly negatively charged at the surface, attracting many positively charged counter ions. It could therefore be questioned if analyzing the NMRD profiles without a contribution of second sphere water molecules is appropriate. The excellent fit of the experimental data as well as the reasonable parameters obtained (Table IV.3-6) shows that if there is such a contribution, its contribution to r_1 is small. A classical molecular dynamics simulation of the Y-DtNP in aqueous solution would probably give more insight on the behavior of water molecules and cations on the surface of the particle.

The fitted parameters given in Table IV.3-7 show that Δ_t^2 and τ_v^{298} , which determine electron spin relaxation, are close to values found for the Ru-metallostar which is build using the same DTTA chelating unit. The amplitude of the static zero-field splitting, Δ_s^2 , is however about 30% lower than for $\{\text{Ru}[\text{Gd}_2\text{bpyDTTA}_2(\text{H}_2\text{O})_4]_3\}^{4-}$. The rotational correlation time τ_R^{298} of the Ru-based metallostar is about 30% smaller than τ_R^{298} of the Gd-DtNP(1) complex, which is oddly the same ratio between their relaxivity values at low field. The rotational correlation time τ_R^{298} can be used to estimate the radius of the rotating particle in a medium with viscosity η by means of the Debye-Stokes-Einstein theory (equ IV.4-8). With this approach, an average diameter of 2.2 nm for Gd-DtNP(1) (eq IV.4-8) is obtained which is the lower end of the particle size distribution measured (chapter IV.3.1).

$$r = \sqrt[3]{\frac{3 \cdot \tau_R \cdot kT}{4\pi \cdot \eta}} = 1.1 \text{ nm}$$

$$\text{with } k_B = 1.3806 \cdot 10^{-23} \frac{\text{N} \cdot \text{m}}{\text{K}}; \eta_{\text{water}}^{298.15} = 0.8909 \cdot 10^{-3} \frac{\text{N} \cdot \text{s}}{\text{m}^2}; \tau_R^{298} = 1181 \text{ ps}$$

IV.4-8

Finally, the relaxivities r_1 for Gd-DtNP show no substantial decrease by increasing the temperature from 25°C to 37°C (for Gd-DtNP(1) @ 60 MHz: $r_1@25^\circ\text{C} = 50.3 \text{ mM}^{-1}\text{s}^{-1}$, $r_1@37^\circ\text{C} = 48.2 \text{ mM}^{-1}\text{s}^{-1}$). A decrease of the rotational correlation time of the complex by increasing the temperature is to a large part compensated by the increase of the water exchange rate for water exchange from the first sphere of the Gd-Dt complexes. This behavior shows that water exchange is too slow for optimum relaxivity. Replacing the DTTA chelating units by another one with $q=2$ and faster water exchange would lead to even higher r_1 values.

IV.4 CONCLUSION

In conclusion, we developed small, water-dispersible, stable gold nanoparticles covalently linked to Gd-DTTA derivative complexes on the surface. Characterizations of these DTTA thiol capped gold nanoparticles (DtNP) using TEM images, dynamic light scattering technique and STEM with EDX analysis indicate a particle size distribution from 2-15 nm, coated by Ln-Dt complexes on the surface.

Molecular modeling shows a rough distance in the range of 1.3 nm between lanthanide(III) ion and gold core surface and the structure that possess Ln-DtNP offers to gadolinium(III) centers a tightly bounding on the surface of particles. Accurate Au, Gd and Y concentrations have been determined with ICP-MS technique.

Bulk magnetic susceptibility of different concentrations of gadolinium Gd-DtNP and yttrium Y-DtNP samples has been established and no significant magnetic contribution can be attributed to the gold core. NMRD profiles of Gd-DtNP systems at 25°C show very high relaxivities and present a broad relaxivity humps indicating a large particle size with slow rotational motion.

The modified Florence approach fits well the experimental points of the NMRD profile of Gd-DtNP, indicating that if there is interaction between gadolinium(III) ions on the surface of the gold core, that would certainly induce a minor change in the relaxation paramagnetic enhancement of water protons. A good fit of experimental relaxivities with the applied theoretical model shows that the particles are very rigid. The fitted parameters of the electronic relaxation are finally in good coherence with what was expected from the Ru-based metallostar values.

IV.5 ACKNOWLEDGEMENTS

I first want to thank Dr. Cédric Mayer and Dr. Caroline Cannizzo for having initiated the gold nanoparticles project, and a special acknowledgement to Cédric for all his helpful advises during the elaboration of the subject.

I strongly acknowledge Dr. Alexey Ulianov for the determination of the metal concentrations by ICP-MS. We established a procedure, which has demanded time and patience.

I acknowledge Dr. Alain Borel for crucial discussions and for his precious accessibility.

I would like to thank Dr. Marco Cantoni and Anas Mouti for the access to TEM spectrometers and for TEM images of my gold nanoparticles.

I would like to thank Dr. Humphrey-Baker and Joel Teuscher for their help with the Dynamic Light Scattering apparatus.

I thank Hugues Jaccard for the synthesis of a part of the Dt compound.

And finally I acknowledge Prof. André E. Merbach for discussions and his continuous interest.

IV.6 REFERENCES

1. I. Brigger, C. Dubernet and P. Couvreur, *Adv. Drug Delivery Rev.*, 2002, **54**, 631-651.
2. C. Vauthier, C. Dubernet, C. Chauvierre, I. Brigger and P. Couvreur, *J. Controlled Release*, 2003, **93**, 151-160.
3. M. Ferrari, *Nat. Rev. Cancer*, 2005, **5**, 161-171.
4. C. J. Sunderland, M. Steiert, J. E. Talmadge, A. M. Derfus and S. E. Barry, *Drug Dev. Res.*, 2006, **67**, 70-93.
5. X. Gao, Y. Cui, R. M. Levenson, L. W. K. Chung and S. Nie, *Nat. Biotechnol.*, 2004, **22**, 969-976.
6. Y. Yamamoto, T. Miura, Y. Nakae, T. Teranishi, M. Miyake and H. Hori, *Physica B*, 2003, **329-333**, 1183-1184.
7. H. Hori, Y. Yamamoto, T. Iwamoto, T. Miura, T. Teranishi and M. Miyake, *Phys. Rev. B: Condens. Matter Mater. Phys.*, 2004, **69**.
8. J. De La Venta, A. Pucci, E. F. Pinel, M. A. García, C. De Julián Fernandez, P. Crespo, P. Mazzoldi, G. Ruggeri and A. Hernando, *Adv. Mater.*, 2007, **19**, 875-877.
9. M. Kanehara, H. Takahashi and T. Teranishi, *Angew. Chem., Int. Ed.*, 2008, **47**, 307-310.
10. T. Teranishi, I. Kiyokawa and M. Miyake, *Adv. Mater.*, 1998, **10**, 596-599.
11. M. Kanehara, E. Kodzuka and T. Teranishi, *J. Am. Chem. Soc.*, 2006, **128**, 13084-13094.
12. C. Alric, J. Taleb, G. Le Duc, C. Mandon, C. Billotey, A. Le Meur-Herland, T. Brochard, F. Vocanson, M. Janier, P. Perriat, S. Roux and O. Tillement, *J. Am. Chem. Soc.*, 2008, **130**, 5908-5915.
13. R. L. Whetten, J. T. Khoury, M. M. Alvarez, S. Murthy, I. Vezmar, Z. L. Wang, P. W. Stephens, C. L. Cleveland, W. D. Luedtke and U. Landman, *Adv. Mater.*, 1996, **8**, 428-433.
14. H. Hori, T. Teranishi, Y. Nakae, Y. Seino, M. Miyake and S. Yamada, *Physics Letters, Section A: General, Atomic and Solid State Physics*, 1999, **263**, 406-410.
15. I. Carmeli, G. Leituss, R. Naaman, S. Reich and Z. Vager, *Isr. J. Chem.*, 2003, **43**, 399-405.
16. A. Hernando, P. Crespo and M. A. García, *Phys. Rev. Lett.*, 2006, **96**.
17. E. Guerrero, T. C. Rojas, M. Multigner, P. Crespo, M. A. Munoz-Marquez, M. A. Garcia, A. Hernando and A. Fernandez, *Acta Mater.*, 2007, **55**, 1723-1730.
18. J. M. De La Fuente, D. Alcántara, P. Eaton, P. Crespo, T. C. Rojas, A. Fernández, A. Hernando and S. Penadés, *J. Phys. Chem. B*, 2006, **110**, 13021-13028.
19. P. Crespo, M. A. Garcia, E. Fernandez Pinel, M. Multigner, D. Alcantara, J. M. De La Fuente, S. Penades and A. Hernando, *Phys. Rev. Lett.*, 2006, **97**.

20. J. S. Garitaonandia, M. Insausti, E. Goikolea, M. Suzuki, J. D. Cashion, N. Kawamura, H. Ohsawa, I. G. De Muro, K. Suzuki, F. Plazaola and T. Rojo, *Nano Lett.*, 2008, **8**, 661-667.
21. L. Moriggi, C. Cannizzo, C. Prestinari, F. Berrière and L. Helm, *Inorg. Chem.*, 2008, **47**, 8357-8366.
22. S. Laus, R. Ruloff, É. Tóth and A. E. Merbach, *Chem. Eur. J.*, 2003, **9**, 3555-3566.
23. W. S. Rasband, *ImageJ*, U.S. National Institutes of Health, Bethesda, Maryland, USA, <http://rsb.info.nih.gov/ij/>, 1997-2008
24. S. Kubo, A. Diaz, Y. Tang, T. S. Mayer, I. C. Khoo and T. E. Mallouk, *Nano Lett.*, 2007, **7**, 3418-3423.
25. I. Bertini, J. Kowalewski, C. Luchinat, T. Nilsson and G. Parigi, *J. Chem. Phys.*, 1999, **111**, 5795-5807.
26. D. Kruk, T. Nilsson and J. Kowalewski, *Phys. Chem. Chem. Phys.*, 2001, **3**, 4907-4917.
27. J. Kowalewski, D. Kruk and G. Parigi, *Adv. Inorg. Chem.*, 2006, **57**, 41-104.
28. , *CAChe Worksystem Pro 6.1*, Fujitsu, 2000-2003
29. R. Xu, in *Particuology*, Editon edn., 2008, vol. 6, pp. 112-115.
30. C. L. Cleveland, U. Landman, T. G. Schaaff, M. N. Shafiqullin, P. W. Stephens and R. L. Whetten, *Phys. Rev. Lett.*, 1997, **79**, 1873-1876.
31. R. N. Barnett, C. L. Cleveland, H. Häkkinen, W. D. Luedtke, C. Yannouleas and U. Landman, *European Physical Journal D*, 1999, **9**, 95-104.
32. C. L. Cleveland and U. Landman, *J. Chem. Phys.*, 1991, **94**, 7376-7396.
33. A. S. Barnard and L. A. Curtiss, *ChemPhysChem*, 2006, **7**, 1544-1553.
34. B. K. Teo and N. J. A. Sloane, *Inorg. Chem.*, 1985, **24**, 4545-4558.
35. D. F. Evans, *Journal of the Chemical Society*, 1959, 2003-2005.
36. D. F. Evans, G. V. Fazakerley and R. F. Phillips, *Journal of the Chemical Society A: Inorganic, Physical, and Theoretical Chemistry*, 1971, 1931-1934.
37. D. Corsi, C. Platas-Iglesias, H. van Bekkum and J. Peters, *Magn. Reson. Chem.*, 2001, **39**, 723-726.
38. S. C. K. Chu, Y. Xu, J. A. Balschi and C. S. Springer Jr., *Magnetic Resonance in Medicine*, 1990, **13**, 239-262.
39. J. Peters, J. Huskens and D. J. Raber, *Prog. Nucl. Magn. Reson. Spectrosc.*, 1996, **28**, 283-350.
40. Y. Yamamoto, T. Miura, T. Teranishi, H. Hori, M. Suzuki, N. Kawamura, H. Miyagawa, T. Nakamura and K. Kobayashi, in *Phys. Rev. Lett.*, Editon edn., 2006, vol. 96, p. 139902.
41. J. B. Livramento, E. Tóth, A. Sour, A. Borel, A. E. Merbach and R. Ruloff, *Angew. Chem.*, 2005, **44**, 1480-1484.

CHAPTER V.
CONCLUSIONS AND
PERSPECTIVES

V.1 CONCLUSIONS

During the last two decades, great efforts have been spent to develop new paramagnetic gadolinium chelates as contrast agents for medical magnetic resonance imaging (MRI) giving better contrast and decreasing acquisition time.¹⁻³ The parameters that can be tuned in order to obtain more efficient agents, meaning to increase water proton relaxivity, are the rotational tumbling time of the complex, the exchange rate of water molecules in the first coordination sphere of Gd^{3+} and the number of water molecules in the first coordination sphere.

The relaxivity values are strongly magnetic-field-dependent and at fields of 3T and above, relaxivity usually drops rapidly. In contrast to that field-dependence, raising the number of inner-sphere water molecules leads to an increase in relaxivity, which is proportional to the number of water molecules independent on the magnetic field. Therefore, several research groups devoted their efforts to the synthesis of chelates allowing the presence of more than one water molecule in the first coordination sphere of the metal.⁴⁻⁷

Our group developed small to medium sized molecules binding two to six Gd^{3+} ions with heptadentate acyclic chelate devoted to a potential MRI contrast agent: the heptadentate acyclic DTTA chelating groups (H_4DTTA = diethylenetriaminetetraacetic acid = N,N' -[iminobis(ethane-2,1-diyl)]bis[N -(carboxymethyl)glycine]).⁸⁻¹² In these complexes, each Gd^{3+} binds two water molecules that exchange relatively rapidly with the bulk, leading to moderately high relaxivities.

A stringent condition for all chelating ligands is that the complex formed with the gadolinium ion is thermodynamically and kinetically very stable and therefore all commercial MRI contrast agents have only one water molecule in the first coordination sphere. The safety of gadolinium based contrast agents became an important issue since it has become the leading suspect for Nephrogenic Systemic Fibrosis (NSF), a disease with high morbidity and mortality.¹³⁻¹⁶ Besides the application in medical diagnostics, MRI contrast agents are also used in medical research and pharmacological studies. These studies in general performed *in vitro* or in animals, depend on the development of new agents delivering good contrast at high magnetic fields. Restrictions concerning high complex stability are however often less severe than in case of clinical use.

The research focuses on the elaboration of platforms that can be used to create a diverse set of multifunctional devices capable of detecting starting diseases and delivering a therapy.

In this thesis, three compounds have been studied, all of them containing the DTTA chelate unit ($H_4DTTA = \text{diethylenetriaminetetraacetic acid} = N,N'\text{-[iminobis(ethane-2,1-diyl)]bis[}N\text{-(carboxymethyl)glycine]}$), a derived from the parent TTAHA⁶⁻.

The first compound studied, the methylated derivative $H_4DTTA\text{-Me}$ ($N,N'\text{-[(methylimino)bis(ethane-2,1-diyl)]bis[}N\text{-(carboxymethyl)glycine]}$), mimics the DTTA chelating unit linked by a methylene group to organic backbones and allowed to study its physicochemical properties. We report the synthesis and physicochemical characterization of the ligand $DTTA\text{-Me}^{4-}$ and its gadolinium complex. The complex shows thermodynamic protonation and stability constants similar to DTTA bound to bpy or a xylene via a CH_2 group. From 1H NMR it was concluded that the first protonation of the ligand $DTTA\text{-Me}^{4-}$ occurs on the central nitrogen, followed by protonation of the two terminal nitrogen atoms and deprotonation of the central one. The next protonation steps are a repeated protonation of the central nitrogen followed by the protonation of carboxylic acids. The pGd value, which is indicative for the stability at physiological conditions, is very close to that of $[Gd(DTPA\text{-BMA})(H_2O)]$.

To measure the conditional relative stability constant for two gadolinium complexes, we propose a method based on relaxivity measurements. This versatile method allows the determination of the relative stability for any couple of ligands, provided its 1H NMR relaxivities are sufficiently different at an appropriate magnetic field. Using this method, we found that in a slightly basic environment (pH 8.3) the $[Gd(DTTA\text{-Me})(H_2O)_2]^-$ complex has a higher stability in respect to $[Gd(DTPA\text{-BMA})(H_2O)]$ as has been shown by the direct competition experiment using relaxivities as the indicator. Transmetalation with Zn^{2+} is however, less favorable for the heptadentate $DTTA\text{-Me}^{4-}$ compared to the octadentate $DTPA\text{-BMA}^{3-}$. Whereas the long time behavior of both complexes is similar, showing relatively strong transmetalation, the metal exchange from Gd^{3+} to Zn^{2+} is about twice as fast for $DTTA\text{-Me}^{4-}$ due to the higher stability of the zinc complex. In contrast to DO3A-based ligands with two water molecules in the first coordination sphere, the formation of ternary complexes with the bidentate lactose anion is very weak. Even at a 10-fold excess of the anion, the measured relaxivity decreases only very slightly.

From the results, it can be concluded that the Gd^{3+} complex of heptadentate DTTA-Me⁴⁻ behaves similarly as that of the commercial octadentate DTPA-BMA³⁻. Considering recent suspicions against $[\text{Gd}(\text{DTPA-BMA})(\text{H}_2\text{O})]$ for being involved in Nephrogenic Systemic Fibrosis (NSF) disease, DTTA-type chelates will not be admitted as contrast agents in clinical MRI. However, their use *in vitro* and in animal studies is absolutely conceivable, mainly at high magnetic fields, where the increase of inner-sphere-coordination water actually seems to be the only promising way to increase the relaxivity.

The second compound is a close derivative to the iron-based metallostar $\{\text{Fe}[\text{Gd}_2\text{bpy-DTTA}_2(\text{H}_2\text{O})_4]_3\}^{4+}$, where the iron(II) central ion is replaced by a ruthenium(II) ion. We describe first the synthesis of self-assembly of the d/f heptametallic edifices $\{\text{Ru}[\text{Ln}_2\text{bpy-DTTA}_2(\text{H}_2\text{O})_4]_3\}^{4+}$ with $\text{Ln} = \text{Y}^{3+}, \text{Gd}^{3+}, \text{Eu}^{3+}$. Besides the higher stability of the $[\text{Ru}(\text{bpy})_3]^{2+}$ unit compared to its iron(II) analogue, the ruthenium-based metallostar shows interesting photophysical properties in addition to its capacity to act as MRI contrast agent. Structural characterization in solution was achieved by ¹H NMR on the diamagnetic yttrium complex by analyzing the aromatic protons of the bipyridyl unit. The gadolinium complex gives rise to NMRD profiles in accordance with those of the iron-based metallostar.² NMRD profiles of both Ru^{2+} and Fe^{2+} based metallostars have been analysed using SBM theory including a Lipary-Szabo treatment of internal motion and using the modified Florence approach developed for slowly rotating, rigid complexes. Data-analysis showed the incapability of SBM theory to reproduce correctly NMRD profiles with long τ_R . Parameters of static ZFS as obtained from the modified Florence method are in reasonable agreement with low temperature EPR results.¹⁷ Comparison of both methods shows that inclusion of internal motion is necessary to have a correct description of high-frequency relaxivity.

The photophysical data determined for $\text{Na}_4\{\text{Ru}[\text{Eu}_2\text{bpy-DTTA}_2(\text{H}_2\text{O})_4]_3\}$ demonstrate the feasibility of d→f visible-sensitized europium ⁵D₀→⁷F_J luminescence in aqueous solution. This opens the way for the development of smart bimodal biological probes.

The third compound represents a common approach achieving high relaxivity with loading a rigid macromolecule with many chelate units binding Gd^{3+} .¹⁸⁻²¹ This compound is represented by Gd-DTTA thiol derivative capped gold nanoparticles (Gd-DtNP). We developed small, water-dispersible, stable nanoparticles covalently linked by mercapto bond to Gd-DTTA derivative complex on the surface. Characterization of Ln-DtNP was performed using TEM

images, dynamic light scattering technique and STEM with EDX analysis, indicating 2-15 nm particle diameters, having close compact gadolinium complexes on the surface.

Molecular modeling shows a rough distance of 1.3 nm between gadolinium(III) ion and gold core surface and the Gd-DtNP structure offers to gadolinium(III) centers a tightly bounding on the surface of particles. Accurate Au, Gd and Y concentrations have been determined with ICP-MS technique.

Bulk magnetic susceptibility of different gadolinium concentration samples has been established following the Evans method and no significant magnetic contribution can be attributed to the gold core. NMRD profiles of Gd-DtNP at 25°C show very high relaxivities and present broad relaxivity humps indicating very large systems with slow rotational motion.

The modified Florence approach fits correctly the NMRD profil of Gd-DtNP, and the electronic relaxation fit parameters are in good coherence with what was expected from the Ru-based metallostar values and confirms that our Gd-DtNP systems are very rigid nano-object.

V.2 PERSPECTIVES

The synthesis of the d/f heptametallc self-assembly edifices $\{\text{Ru}[\text{Ln}_2\text{bpy-DTTA}_2(\text{H}_2\text{O})_4]_3\}^{4-}$ with $\text{Ln} = \text{Y}^{3+}, \text{Gd}^{3+}, \text{Eu}^{3+}$ opens a door to similar but more complex self-assembly structures. We present here two very interesting multimetallic edifices that have promising potential for fundamental studies in relaxivity and luminescence studies (Figure V.2-1 and Figure V.2-2).

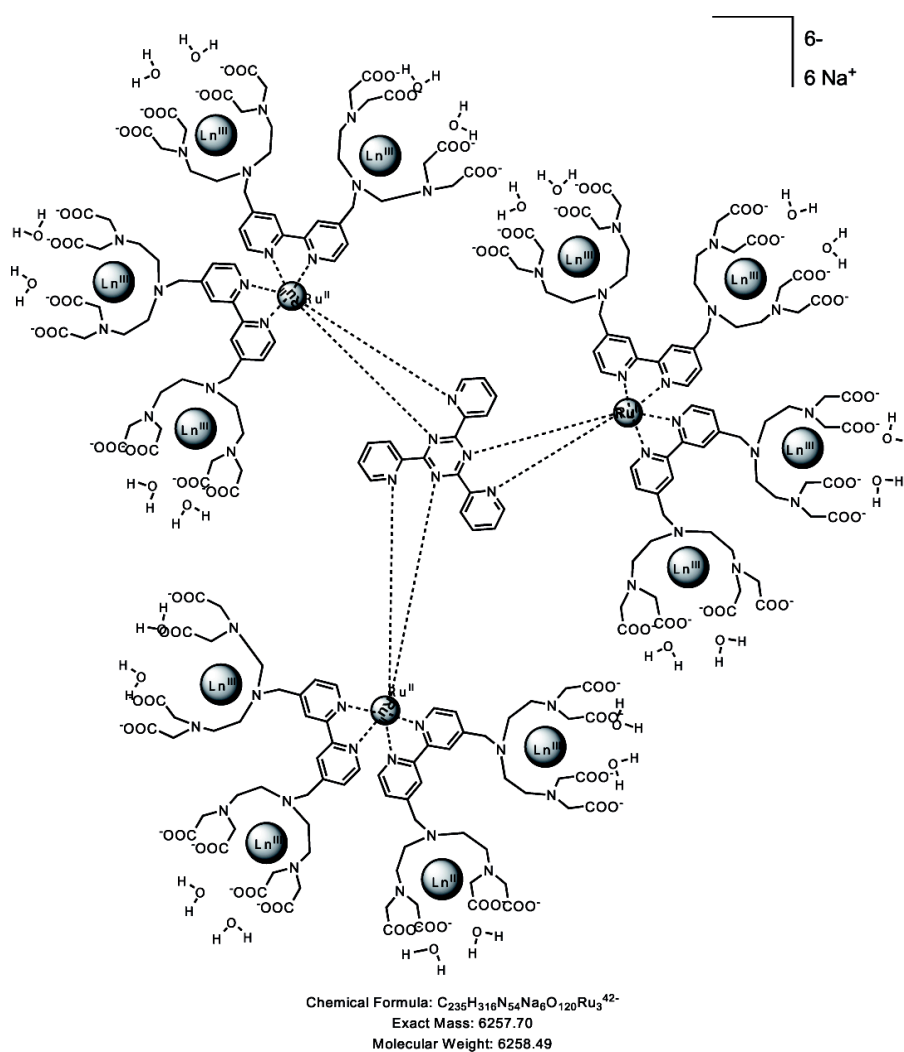


Figure V.2-1: Self-assembled multimetallic edifice $\{\text{TPTz}\{\text{Ru}[\text{Ln}_2\text{bpy-DTTA}_2(\text{H}_2\text{O})_4]_2\}_3\}^{6-}$.

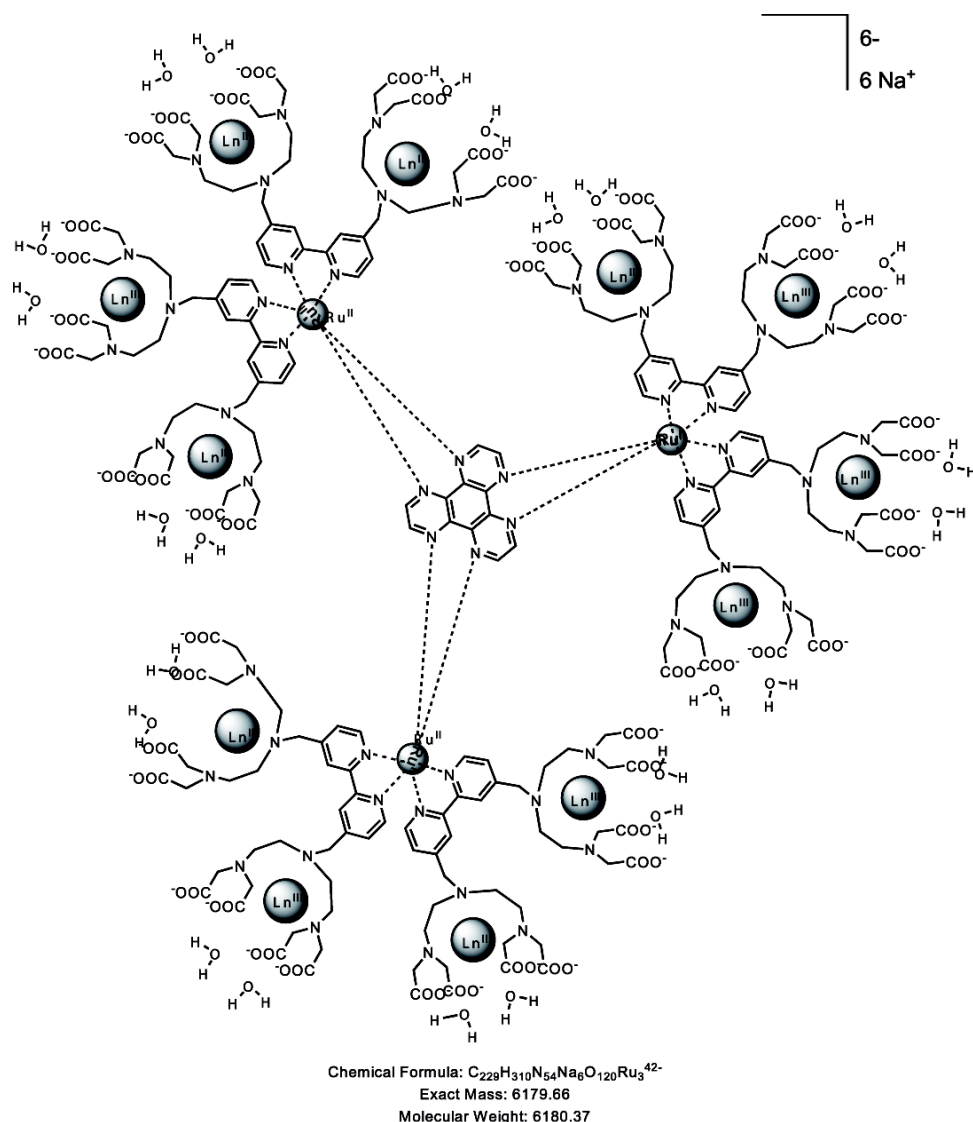


Figure V.2-2: Self-assembled multimetallic edifice $\{HAT\{Ru[Ln_2bpy-DTTA_2(H_2O)_4]_2\}_3\}^{6-}$.

DTTA thiol capped gold nanoparticles Ln-DtNP introduced in chapter IV have strong potential to bring fundamental insights on very rigid structures used as MRI contrast agent. Several variations of these nano-objects can be imagined. For instance, increasing the length of the carbon chains linking the central nitrogen of the DTTA chelate to the benzene will bring more flexibility. One has thus to think about Gd-DtNP structures containing short and long DTTA thiol derivatives for bringing relaxivity efficiency at middle and high fields.

However, conventional gadolinium-based MRI contrast agents have sensitivity in the micromolar range, which with certain exceptions is usually inadequate for molecular MRI. This first generation of extracellular gadolinium chelates also have extremely short

intravascular half-lives and rapid renal excretion, which further limits their utility for most molecular imaging applications.

The next step towards powerful imaging involves specific recognition between the Gd^{III} complex and a target of interest. The sensitivity of targeted magnetic nanoparticles is currently in the nanomolar range and will likely be improved through the use of agents with higher relaxivities than the present constructs. The ability to image nanoparticles with T_1 , T_2 and off-resonance techniques provides multiple possibility to ensure probe specificity. Future nanoparticles will further enhance specificity by allowing multi-modality imaging (MRI, fluorescence, PET) of the contrast agent to be performed.²² First generation polymer-coated nanoparticles are currently approved for clinical use and subsequent generations of nanoparticles (Combinex, Advanced Magnetix, Cambridge MA)²³ have already completed phase 3 clinical trials. MRI of nanoparticles in the cardiovascular system thus has the potential to become a powerful technology in both the basic science as well as the clinical settings.

V.3 REFERENCES

1. P. Caravan, J. J. Ellison, T. J. McMurry and R. B. Lauffer, *Chem. Rev.*, 1999, **99**, 2293-2352.
2. A. E. Merbach and É. Tóth, eds., *The Chemistry of Contrast Agents in Medical Magnetic Resonance Imaging*, 1st edn., John Wiley & Sons, Chichester, 2001.
3. P. Caravan, *Chem. Soc. Rev.*, 2006, **35**, 512-523.
4. S. Aime, E. Gianolio, D. Corpillo, C. Cavalotti, G. Palmisano, M. Sisti, G. B. Giovenzana and R. Pagliarin, *Helv. Chim. Acta*, 2003, **86**, 615-632.
5. A. R. Johnson, B. O'Sullivan and K. N. Raymond, *Inorg. Chem.*, 2000, **39**, 2652-2660.
6. E. J. Werner, S. Avedano, M. Botta, B. P. Hay, E. G. Moore, S. Aime and K. N. Raymond, *J. Am. Chem. Soc.*, 2007, **129**, 1870-1871.
7. S. Aime, L. Calabi, C. Cavallotti, E. Gianolio, G. B. Giovenzana, P. Losi, A. Maiocchi, G. Palmisano and M. Sisti, *Inorg. Chem.*, 2004, **43**, 7588-7590.
8. J. Costa, R. Ruloff, L. Burai, L. Helm and A. E. Merbach, *J. Am. Chem. Soc.*, 2005, **127**, 5147-5157.
9. J. Costa, E. Tóth, L. Helm and A. E. Merbach, *Inorg. Chem.*, 2005, **44**, 4747-4755.
10. J. B. Livramento, A. Sour, A. Borel, A. E. Merbach and É. Tóth, *Chem. Eur. J.*, 2006, **12**, 989-1003.
11. J. B. Livramento, C. Weidensteiner, M. I. M. Prata, P. R. Allegrini, C. F. G. C. Geraldes, L. Helm, R. Kneuer, A. E. Merbach, A. C. Santos, P. Schmidt and É. Tóth, *Contrast Med. Mol. Imaging*, 2006, **1**, 30-39.
12. J. B. Livramento, L. Helm, A. Sour, C. O'Neil, A. E. Merbach and E. Toth, *Dalton Trans.*, 2008, 1195-1202.
13. Z. H. Endre, *Int. Med. J.*, 2007, **37**, 429-431.
14. T. Grobner and F. C. Prischl, *Kidney International*, 2007, **72**, 260-264.
15. M. A. Perazella, *Clin. J. Am. Soc. Nephrol.*, 2007, **2**, 200-202.
16. H. Ersoy and F. J. Rybicki, *J. Magn. Reson. Imag.*, 2007, **26**, 1190-1197.
17. M. Benmelouka, J. Van Tol, A. Borel, M. Port, L. Helm, L. C. Brunel and A. E. Merbach, *J. Am. Chem. Soc.*, 2006, **128**, 7807-7816.
18. Z. Jaszberenyi, L. Moriggi, P. Schmidt, C. Weidensteiner, R. Kneuer, A. E. Merbach, L. Helm and É. Tóth, *J. Biol. Inorg. Chem.*, 2007, **12**, 406-420.
19. H. Kobayashi and M. W. Brechbiel, *Adv. Drug Deliv. Rev.*, 2005, **57**, 2271-2286.
20. S. Langereis, A. Dirksen, T. M. Hackeng, M. H. P. Van Genderen and E. W. Meijer, *New J. Chem.*, 2007, **31**, 1152-1160.
21. S. Laus, A. Sour, R. Ruloff, É. Tóth and A. E. Merbach, *Chem. Eur. J.*, 2005, **11**, 3064-3076.

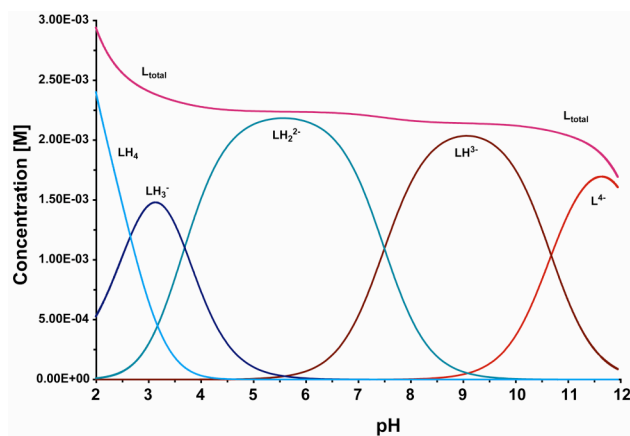
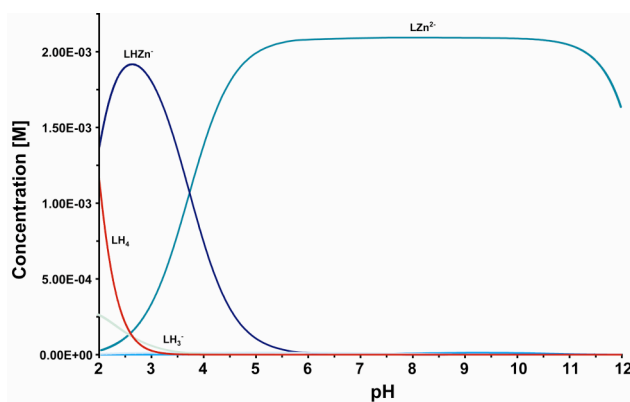
22. D. E. Sosnovik, M. Nahrendorf and R. Weissleder, *Basic Research in Cardiology*, 2008, **103**, 122-130.
23. M. G. Harisinghani, J. Barentsz, P. F. Hahn, W. M. Deserno, S. Tabatabaei, C. H. Van de Kaa, J. De la Rosette and R. Weissleder, *N. Engl. J. Med.*, 2003, **348**, 2491-2499.

CHAPTER VI.

APPENDIX

TABLE OF CONTENTS OF CHAPTER VI

<u>VI.1</u>	<u>APPENDIX TO CHAPTER II:</u>	<u>157</u>
VI.1.1	PROTONATION AND STABILITY CONSTANTS BY POTENTIOMETRIC MEASUREMENTS	157
VI.1.2	¹H-NMR IN D₂O	159
VI.1.3	CONDITIONAL RELATIVE STABILITY CONSTANT $K_{L1/L2}^{*}$ OF [Gd(DTTA-ME)(H₂O)₂]⁻ RELATIVE TO [Gd(DTPA-BMA)(H₂O)]	160
	SINGLE RELAXIVITY TO OBTAIN THE CONDITIONAL RELATIVE STABILITY CONSTANT	162
VI.1.4	TRANSMETALLATION OF [Gd(DTTA-ME)(H₂O)₂]⁻ WITH ZN²⁺	165
VI.1.5	SEARCH FOR ADDUCT FORMATION BETWEEN [Gd(DTTA-ME)(H₂O)₂]⁻ AND L-LACTATE	166
<u>VI.2</u>	<u>APPENDIX TO CHAPTER III: EXPERIMENTAL DATA</u>	<u>167</u>
VI.2.1	SUIVI THEORIQUE PAR RMN DE LA FORMATION DE RU^{II}[Y₂BIPY(DTTA)₂]₃·NA₄	175
	SUIVI RMN DE LA REACTION : RU^{II}(TOS)⁻²₂(H₂O)₆ + 3 [BIPYDTTA₂Y₂]⁻ → [RU^{II}(BIPYDTTA₂Y₂)₃]⁻⁴	176
VI.2.2	SUIVI PRATIQUE PAR RMN DE LA FORMATION DE RU^{II}[Y₂BIPY(DTTA)₂]₃·NA₄	176
	ETAPE 1 : SOLUTION DE YCl₃:	176
	ETAPE 2 : SOLUTION DE BIPYDTTA₂	176
	ETAPE 3 : SOLUTION DE BIPYDTTA₂Y₂	177
	ETAPE 4 : SPECTRE ¹H DU RU(TOS)₂(H₂O)₆:	178
	ETAPE 5 : SYNTHÈSE DU RU^{II}[(BIPYDTTA₂Y₂)₃]⁻⁴ :	178
	ETAPE 6 : SYNTHÈSE DU RU^{II}[(BIPYDTTA₂Y₂)₃]⁻⁴ :	179
VI.2.3	{RU[Gd₂BPY-DTTA₂(H₂O)₄]₃]⁻⁴ AND {FE[Gd₂BPY-DTTA₂(H₂O)₄]₃]⁻⁴ RELAXIVITIES (NMRD)}	180
<u>VI.3</u>	<u>APPENDIX TO CHAPTER IV</u>	<u>181</u>
VI.3.1	GD-DTNP(1), GD-DTNP(2) ANB GD-DTNP(3) RELAXIVITIES (NMRD)	181

VI.1 APPENDIX TO CHAPTER II:**VI.1.1 Protonation and Stability Constants by Potentiometric Measurements****Figure VI.1-1.** Distribution diagram for DTTA-Me ligand.**Figure VI.1-2.** Distribution diagram of Zn-DTTA-Me.

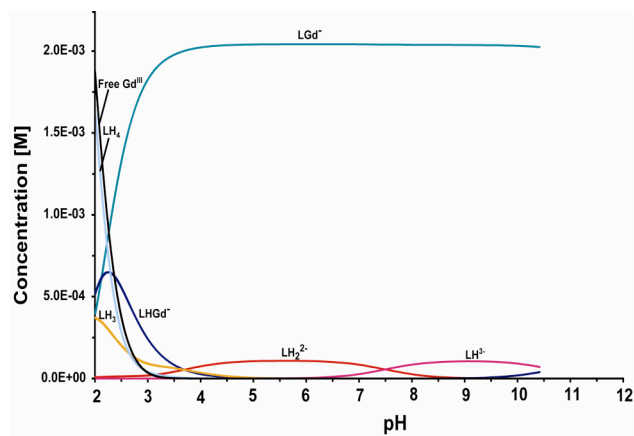


Figure VI.1-3. Distribution diagram of Gd-DTTA-Me.

VI.1.2 ^1H -NMR in D_2O

Table VI.1-1. ^1H NMR (400 MHz) DTTA-Me⁴⁻ chemical shifts vs pD in D_2O at room temperature and I=0.1 M KCl.

pD	δ [ppm] s2	δ [ppm] d1	δ [ppm] d2	δ [ppm] s1
2.096	2.990	3.837	3.456	3.504
2.439	2.987	3.829	3.479	3.513
2.466	2.986	3.828	3.483	3.514
2.934	2.971	3.830	3.526	3.526
2.947	2.968	3.830	3.527	3.527
3.050	2.959	3.831	3.531	3.531
3.442	2.902	3.832	3.559	3.474
3.446	2.884	3.833	3.561	3.457
3.940	2.733	3.828	3.532	3.295
3.949	2.741	3.828	3.533	3.304
4.426	2.582	3.819	3.484	3.125
4.440	2.560	3.817	3.475	3.100
4.935	2.472	3.811	3.442	2.999
5.449	2.429	3.807	3.425	2.949
5.454	2.429	3.807	3.425	2.950
5.943	2.421	3.802	3.417	2.938
5.969	2.421	3.799	3.414	2.937
6.456	2.424	3.794	3.410	2.938
6.460	2.427	3.791	3.406	2.940
6.967	2.445	3.768	3.388	2.950
7.038	2.452	3.761	3.383	2.956
7.430	2.494	3.716	3.347	2.984
7.457	2.517	3.703	3.336	2.999
7.952	2.613	3.601	3.248	3.056
8.460	2.732	3.451	3.137	3.137
8.938	2.826	3.351	3.052	3.194
8.945	2.814	3.358	3.060	3.184
9.440	2.848	3.320	3.025	3.207
9.463	2.846	3.316	3.023	3.206
9.906	2.844	3.301	3.003	3.197
9.953	2.847	3.299	3.004	3.201
10.436	2.816	3.288	2.983	3.168
10.450	2.815	3.290	2.984	3.167
10.923	2.732	3.274	2.942	3.083
11.442	2.474	3.235	2.821	2.821
11.986	2.309	3.210	2.750	2.667
12.481	2.234	3.197	2.715	2.573

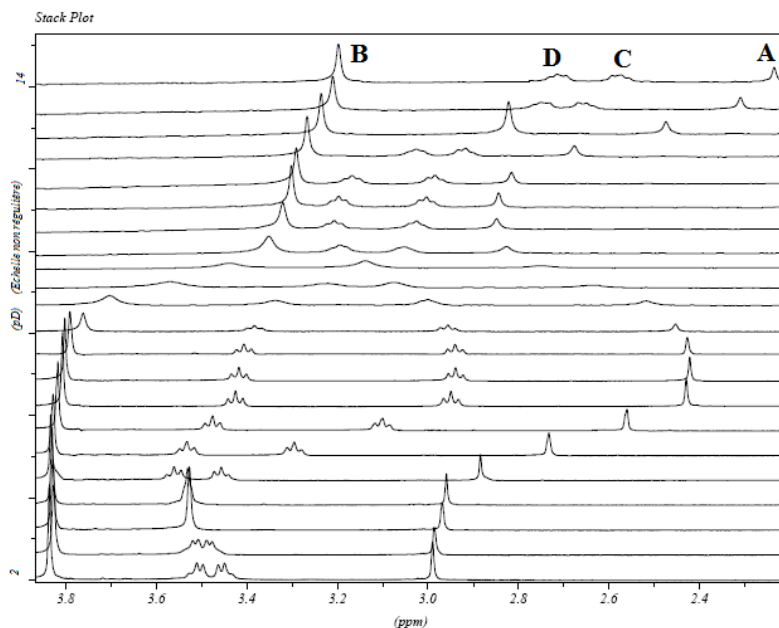


Figure VI.1-4. ^1H NMR (400 MHz) spectra describing DTTA-Me $^{4-}$ chemical shifts vs pD in D_2O at room temperature and $I=0.1$ M KCl.

VI.1.3 Conditional Relative Stability Constant $K_{L1/L2}^*$ of $[\text{Gd}(\text{DTTA-Me})(\text{H}_2\text{O})_2]^-$ Relative to $[\text{Gd}(\text{DTPA-BMA})(\text{H}_2\text{O})]$

All relaxivities r_1^m measured on samples of different mixtures of *sol* L_1 and *sol* L_2 can be fitted together or treated alone to obtain the conditional relative stability constant $^*K_{L1/L2}$.

Fit to obtain the conditional relative stability constant

All relaxivities r_1^m measured on samples of different mixtures of *sol* L_1 and *sol* L_2 can be fitted together to obtain the conditional relative stability constant $^*K_{L1/L2}$. If C_m^{Gd} , $C_m^{L_1}$ and $C_m^{L_2}$ are the total concentrations of Gd^{3+} , L_1 and L_2 , in the mixture m , the concentration of complex GdL_2 is given by

$$\text{From } K_{L_1/L_2}^* = \frac{[GdL_1][L_2]}{[GdL_2][L_1]}$$

$$\text{and } [GdL_1] = C_m^{Gd} - [GdL_2], \quad [L_1] = C_m^{L_1} - [GdL_1], \quad [L_2] = C_m^{L_2} - [GdL_2]$$

$$(5) \quad [GdL_2] = \frac{-B + \sqrt{B^2 - 2A(C_m^{Gd} \cdot C_m^{L_2})}}{A} \quad \text{with } A = 2(1 - K_{L_1/L_2}^*)$$

$$\text{and } B = -(C_m^{Gd}(K_{L_1/L_2}^* - 1) - K_{L_1/L_2}^* \cdot C_m^{L_1} - C_m^{L_2})$$

The mixtures are prepared from stock solutions *sol* L_1 and *sol* L_2 with total ligand concentrations $C_0^{L_1}$, $C_0^{L_2}$ and total gadolinium concentrations C_0^{Gd1} , C_0^{Gd2} , respectively.

Furthermore, a constant dilution by a factor $f = 0.71$ was used. The concentrations of the samples can be expressed as a function of mole fraction of ligand L_2 , χ_{L_2} , as

$$(6) \quad C_m^{Gd} = f(C_0^{Gd1}(1 - \chi_{L_2}) + C_0^{Gd2}\chi_{L_2})$$

$$(7) \quad C_m^{L_1} = f C_0^{L_1}(1 - \chi_{L_2})$$

$$(8) \quad C_m^{L_2} = f C_0^{L_2}\chi_{L_2}$$

The relaxivity r_1^m as a function of χ_{L_2} is given by

$$r_1^m = r_1^{GdL_1} \left(1 - \frac{[GdL_2]}{C_m^{Gd}} \right) + r_1^{GdL_2} \left(\frac{[GdL_2]}{C_m^{Gd}} \right)$$

where $[GdL_2]$ is obtained from (5) – (8).

The only fitted parameters are $K_{L1/L2}^*$, $r_1^{GdL_1}$ and $r_1^{GdL_2}$.

Table VI.1-2. Concentrations and measured relaxation times as a function of sample composition for [Gd(DTTA-Me)(H₂O)₂]/[Gd(DTPA-BMA)(H₂O)] mixtures.

	C_0^{L1}	C_0^{L2}	C_0^{Gd1}	C_0^{Gd2}			
	[mM]	[mM]	[mM]	[mM]			
sol L ₁	12.76	/	4.27	/			
sol L ₂	/	12.81	/	4.29			

χ_{L2}	C_m^{L1}	C_m^{L2}	C_m^{Gd}	T_1	f_{L1}^a	f_{L2}^b
	[mM]	[mM]	[mM]	[ms]	[mM]	[mM]
0	9.38	-	3.14	50.7	0.74	-
0.16	7.61	1.45	3.03	53.2	0.71	0.71
0.33	6.08	2.99	3.04	54.4	0.71	0.71
0.50	4.58	4.58	3.06	56.3	0.72	0.72
0.67	3.00	6.10	3.05	60.4	0.71	0.71
0.84	1.46	7.69	3.06	67.1	0.72	0.71
1	-	9.32	3.12	79.7	-	0.73

^a dilution factor $f_{L1} = C_m^{L1}/(C_0^{L2} \cdot (1 - \chi_{L2}))$

^b dilution factor $f_{L2} = C_m^{L2}/(C_0^{L2} \cdot \chi_{L2})$

Single relaxivity to obtain the conditional relative stability constant

If we consider a single relaxivity r_1^m , where C_m^{Gd} , C_m^{L1} and C_m^{L2} are the total concentrations of Gd³⁺, L₁ and L₂, in the mixture m :

$$(1) \quad r_1^m = r_1^{GdL_1} \cdot \frac{[GdL_1]}{C_m^{Gd}} + r_1^{GdL_2} \cdot \frac{[GdL_2]}{C_m^{Gd}}$$

$$(2) \quad K_{L1/L2}^* = \frac{[GdL_1]}{[GdL_2]} \cdot \frac{[L_1]}{[L_2]}$$

Substitution in (1):

$$[GdL_2] = C_m^{Gd} - [GdL_1] \quad \text{thus (3) } [GdL_1] = \left(\frac{r_1^m - r_1^{GdL_2}}{r_1^{GdL_1} - r_1^{GdL_2}} \right) \cdot C_m^{Gd}$$

Substitutions in (2):

$$L_1 = C_m^{L_1} - [GdL_1]$$

$$L_2 = C_m^{L_2} - C_m^{Gd} + [GdL_1] \quad \text{thus (4) } K_{L1/L2}^* = \frac{[GdL_1] (C_m^{L_2} - C_m^{Gd} + [GdL_1])}{(C_m^{Gd} - [GdL_1]) (C_m^{L_1} - [GdL_1])}$$

$$\text{Combining (3)+(4):} \quad K_{L1/L2}^* = \frac{\left(\frac{r_1^m - r_1^{GdL_2}}{r_1^{GdL_1} - r_1^{GdL_2}} \right) \left(\frac{C_m^{L_2}}{C_m^{Gd}} - 1 + \left(\frac{r_1^m - r_1^{GdL_2}}{r_1^{GdL_1} - r_1^{GdL_2}} \right) \right)}{\left(1 - \left(\frac{r_1^m - r_1^{GdL_2}}{r_1^{GdL_1} - r_1^{GdL_2}} \right) \right) \left(\frac{C_m^{L_1}}{C_m^{Gd}} - \left(\frac{r_1^m - r_1^{GdL_2}}{r_1^{GdL_1} - r_1^{GdL_2}} \right) \right)}$$

Figure VI.1-5: Demonstration of the equation for calculating the conditional relative stability constant $K_{L1/L2}^*$

We resume parameters for single relaxivity approach and for the fit in the next table:

Table VI.1-3. Conditional, $K_{L1/L2}^*$, and thermodynamic, $K_{L1/L2}$, relative stability constants between Gd^{3+} complexes with DTTA- Me^{4-} (L_1) and DTPA-BMA₃ (L_2) from relaxivity experiments (25°C, 60 MHz, I=0.1 M NaCl).

%L ₂	pH ^a	r_1^m	$K_{L1/L2}^*$ (pH 8.3)	α_{L1}	α_{L2}	$K_{L1/L2}^b$
[s ⁻¹ mM ⁻¹]						
0	8.30	6.18	/	334.1	/	/
16	8.29	6.10	7.01	343.1	13.0	185
33	8.33	5.94	6.27	308.7	12.0	162
50	8.33	5.70	6.16	308.7	12.0	159
67	8.29	5.32	6.37	343.1	13.0	168
84	8.27	4.76	7.35	361.9	13.6	196
100	8.30	4.02	/	/	12.8	/
Fit	8.30c	d	6.4	332.4	12.7	168

^a pH values at the end of the competition. ^b From eq II.3-10. ^c average over pHs of solutions 16, 33, 50, 67 and 84 % L₂. ^d $r_1^{GdL_1}$ (fitted) = 6.18 (0.01) , $r_1^{GdL_2}$ (fitted) = 4.03 (0.01).

```

function [y]=DTTAm_DTPABMA(x,p) %\FWD=0; \DEFFAR(R_DTTAm,R_DTPABMA,Co_GdDTTAm,Co_GdDTPABMA,Co_DTTAm,
Co_DTPABMA,K)\NARGOUT=1;
% *****
% Six paramètres:
% R_DTTAm:relxivité du complexe Gd_DTTAm (mM-ls-1)
% R_DTPABMA:relxivité du complexe Gd_DTPABMA (mM-ls-1)-
% Cm_Gd: concentration en Gd3+ de la solution mélange
% Co_DTTAm: concentration en DTTAm de la solution mère 1, solution contenant 1:3 de Gd3+:DTTAm
% Co_DTPABMA: concentration en DTPABMA de la solution mère 2, solution contenant 1:3 de Gd3+:DTPABMA
% K: KGd_DTTAm/KGd_DTPABMA, rapport des constantes de stabilités des deux complexes
% INITIAL DATA CONTENTS:
% x(:,1) = pourcentage représentant le volume de solution mère 2 par volume total de la solution mélange
% y(:,1) = Relaxivité totale de la solution mélange (mM-ls-1)
% CONDITIONS ON VISUALISEUR:
% - Nombre de variables indépendantes = 7
% L.MORIGGI - LCIB - EPFL - 2007
% *****
% ----- PARAMETERS -----
R_DTTAm = p(1);
R_DTPABMA = p(2);
Co_GdDTTAm = p(3);
Co_GdDTPABMA= p(4);
Co_DTTAm = p(5);
Co_DTPABMA = p(6);
K = p(7);
% ----- VARIABLES DEPENDANTES -----
pc_vol2 = x(:,1); % pourcentage représentant le volume de solution mère 2 par volume total
de la solution mélange
% ----- DEBUT DU CALCUL -----
% *** INIT RESULTS (1 columns)
y = NaN * ones(size(x,1),1);

Cm_Gd = (1-pc_vol2/100).*Co_GdDTTAm + (pc_vol2/100).* Co_GdDTPABMA ;

Cm_GdDTPABMA = ((K.*Co_DTTAm.*(1-pc_vol2./100)-K.*Cm_Gd+Cm_Gd+Co_DTPABMA.*pc_vol2./100)-
((K.*Co_DTTAm.*(1-pc_vol2./100)-K.*Cm_Gd+Cm_Gd+Co_DTPABMA.*pc_vol2/100).^2 - 4.*(1-
K).*(Cm_Gd.*Co_DTPABMA.*pc_vol2./100)).^(1/2))./(2.*(1-K))

R_total = R_DTTAm.*(Cm_Gd-Cm_GdDTPABMA)./Cm_Gd + R_DTPABMA.*(Cm_GdDTPABMA./Cm_Gd)

% *** OUTPUT ***
y(:,1) = R_total ; % relxivité de la solution mélange (mM-ls-1)

return;

```

```

function [y]=Ki_parRMN(x,p) %\FWD=0; \DEFPAR(K1,K2,K3,K4,K5,deltaA0,deltaA1,deltaA2,deltaA3,deltaA4,
deltaA5,deltaB0,deltaB1,deltaB2,deltaB3,deltaB4,deltaB5,deltaC0,deltaC1,deltaC2,deltaC3,deltaC4,deltaC5,
deltaD0,deltaD1,deltaD2,deltaD3,deltaD4,deltaD5)\NARGOUT=4;
% *****
% Pour ligand du type H4L
% vingt quatre paramètres:
% K1,K2,K3,K4, K5: constantes cumulatives betaHL/L, betaH2L/L,
% betaH3L/L et betaH4L/L
% deltaA0,deltaA1,deltaA2,deltaA3,deltaA4,deltaA5: déplacement chimique du CH3 pour les cinq espèces L4-
,HL3-,H2L2-,H3L-,H4L
% deltaB0,deltaB1,deltaB2,deltaB3,deltaB4,deltaB5: déplacement chimique des ethylènes liés aux acétates
pour les cinq espèces L4-,HL3-,H2L2-,H3L-,H4
% deltaC0,deltaC1,deltaC2,deltaC3,deltaC4,deltaC5: déplacement chimique des ethylènes-amines
extérieures pour les cinq espèces L4-,HL3-,H2L2-,H3L-,H4
% deltaD0,deltaD1,deltaD2,deltaD3,deltaD4,deltaD5: déplacement chimique des ethylènes-amine centrale
pour les cinq espèces L4-,HL3-,H2L2-,H3L-,H4
% INITIAL DATA CONTENTS:
% x(:,1) = pH de la solution
% y(:,4) = (DELTA) : déplacement chimique d'un proton d'une espèce (exemple,déplacement des protons CH3
de l'espèce H4L
% CONDITIONS ON VISUALISEUR:
% - Nombre de variables indépendantes = 29
% L.MORIGGI - LOCIB - EPFL - 2007
% *****
% ----- PARAMETERS -----
K1 = p(1);
K2 = p(2);
K3 = p(3);
K4 = p(4);
K5 = p(5);
deltaA0 = p(6);
deltaA1 = p(7);
deltaA2 = p(8);
deltaA3 = p(9);
deltaA4 = p(10);
deltaA5 = p(11);
deltaB0 = p(12);
deltaB1 = p(13);
deltaB2 = p(14);
deltaB3 = p(15);
deltaB4 = p(16);
deltaB5 = p(17);
deltaC0 = p(18);
deltaC1 = p(19);
deltaC2 = p(20);
deltaC3 = p(21);
deltaC4 = p(22);
deltaC5 = p(23);
deltaD0 = p(24);
deltaD1 = p(25);
deltaD2 = p(26);
deltaD3 = p(27);
deltaD4 = p(28);
deltaD5 = p(29);
% ----- VARIABLES DEPENDANTES -----
IT = x(:,1); % pH
% ----- DEBUT DU CALCUL -----
% *** INIT RESULTS (2 columns)
y = NaN * ones(size(x,1),4);
aH = 10.^(-(IT)) ;
beta1 = K1 ;
beta2 = K1*K2 ;
beta3 = K1*K2*K3 ;
beta4 = K1*K2*K3*K4 ;
beta5 = K1*K2*K3*K4*K5 ;
p0 = 1./(1 + beta1*aH + beta2*aH.^2 + beta3*aH.^3 + beta4*aH.^4 + beta5*aH.^5);
deltaA = p0.*deltaA0 + beta1*p0.*aH.*deltaA1 + beta2*p0.*aH.^2*deltaA2 + beta3*p0.*aH.^3*deltaA3 +
beta4*p0.*aH.^4*deltaA4 + beta5*p0.*aH.^5*deltaA5;
deltaB = p0.*deltaB0 + beta1*p0.*aH.*deltaB1 + beta2*p0.*aH.^2*deltaB2 + beta3*p0.*aH.^3*deltaB3 +
beta4*p0.*aH.^4*deltaB4 + beta5*p0.*aH.^5*deltaB5;
deltaC = p0.*deltaC0 + beta1*p0.*aH.*deltaC1 + beta2*p0.*aH.^2*deltaC2 + beta3*p0.*aH.^3*deltaC3 +
beta4*p0.*aH.^4*deltaC4 + beta5*p0.*aH.^5*deltaC5;
deltaD = p0.*deltaD0 + beta1*p0.*aH.*deltaD1 + beta2*p0.*aH.^2*deltaD2 + beta3*p0.*aH.^3*deltaD3 +
beta4*p0.*aH.^4*deltaD4 + beta5*p0.*aH.^5*deltaD5;

% *** OUTPUT ***
y(:,1) = deltaA ; % déplacement chimique observé pour le methyl
y(:,2) = deltaB ; % déplacement chimique observé pour les ethylènes liés aux acétates
y(:,3) = deltaC ; % déplacement chimique observé pour les ethylènes-amines extérieures
y(:,4) = deltaD ; % déplacement chimique observé pour les ethylènes-amine centrale

return;

```

VI.1.4 Transmetallation of $[\text{Gd}(\text{DTTA-Me})(\text{H}_2\text{O})_2]^-$ with Zn^{2+}

Table VI.1-4: Evolution of $R_1^m/R_{1,0}$ ($T= 310 \text{ K}$; $B = 1.41 \text{ T}$, 60 MHz ; $\text{pH } 7.0$) versus time for $[\text{Gd}(\text{DTTA-Me})(\text{H}_2\text{O})_2]^-$ and $[\text{Gd}(\text{DTPA-BMA})(\text{H}_2\text{O})]$ complexes in presence of equimolar amounts of Zn^{2+} ions in phosphate buffer solution. Evolution of $[\text{Gd}(\text{DTTA-Me})(\text{H}_2\text{O})_2]^-$ in phosphate buffer solution without Zn^{2+} ions.

$[\text{Gd}(\text{DTTA-Me})(\text{H}_2\text{O})_2]^-$				$[\text{Gd}(\text{DTPA-BMA})(\text{H}_2\text{O})]$				$[\text{Gd}(\text{DTTA-Me})(\text{H}_2\text{O})_2]^-$ without Zn^{2+} ions			
Time	T_1	$1/T_1^m$	$R_1^m/R_{1,0}$	Time	T_1	$1/T_1^m$	$R_1^m/R_{1,0}$	Time	T_1	$1/T_1^m$	$R_1^m/R_{1,0}$
min	ms	$\text{s}^{-1} \text{ mM}^{-1}$		min	ms	$\text{s}^{-1} \text{ mM}^{-1}$		min	ms	$\text{s}^{-1} \text{ mM}^{-1}$	
0	73.1	13.435	1.19	0	105	9.279	0.96	0	86.5	11.316	1
13	80.6	12.162	1.07	20	95.2	10.259	1.06	12	85.6	11.437	1.01
23	90	10.866	0.96	40	98.2	9.938	1.03	20	85.9	11.396	1.01
27	94	10.393	0.92	61	108	9.014	0.93	27	86.1	11.369	1
36	102	9.559	0.84	80	117	8.302	0.86	79	85.7	11.424	1.01
44	107	9.101	0.8	100	121	8.019	0.83	131	85.5	11.451	1.01
58	114	8.527	0.75	132	130	7.447	0.77	184	85.4	11.465	1.01
71	119	8.158	0.72	166	135	7.162	0.74	236	85.2	11.492	1.02
74	125	7.755	0.69	222	142	6.797	0.7	289	85.1	11.506	1.02
87	130	7.447	0.66	277	148	6.512	0.67	341	85.1	11.506	1.02
103	134	7.218	0.64	332	154	6.249	0.65	393	85.4	11.465	1.01
118	138	7.001	0.62	387	159	6.044	0.63	446	85.4	11.465	1.01
141	147	6.558	0.58	443	162	5.928	0.61	498	84.9	11.534	1.02
153	151	6.378	0.56	498	167	5.743	0.59	550	85.1	11.506	1.02
190	160	6.005	0.53	553	172	5.569	0.58	603	85	11.52	1.02
227	169	5.672	0.5	609	178	5.373	0.56	655	84.9	11.534	1.02
263	178	5.373	0.47	664	184	5.19	0.54	708	85	11.52	1.02
299	185	5.16	0.46	719	189	5.046	0.52	760	85	11.52	1.02
336	193	4.936	0.44	774	195	4.883	0.51	812	85.1	11.506	1.02
372	199	4.78	0.42	830	201	4.73	0.49	865	84.9	11.534	1.02
408	205	4.633	0.41	885	207	4.586	0.47	917	84.9	11.534	1.02
444	212	4.472	0.4	940	214	4.428	0.46	969	84.7	11.561	1.02
480	221	4.28	0.38	995	220	4.3	0.45	1022	84.8	11.547	1.02
516	230	4.103	0.36	1051	226	4.18	0.43	1074	84.6	11.575	1.02
553	239	3.939	0.35	1106	233	4.047	0.42	1127	84.7	11.561	1.02
589	248	3.787	0.33	1161	240	3.922	0.41	1179	84.4	11.603	1.03
981	362	2.517	0.22	1222	256	3.661	0.38	1231	84.4	11.603	1.03
1013	372	2.443	0.22	1270	263	3.557	0.37	1284	84.5	11.589	1.02
1078	390	2.319	0.2	1367	275	3.391	0.35	1336	84.6	11.575	1.02
1142	408	2.206	0.19	1464	288	3.227	0.33	1388	84.5	11.589	1.02
1206	426	2.102	0.19	1560	301	3.077	0.32	1441	84.2	11.631	1.03
1271	443	2.012	0.18	1657	315	2.93	0.3	1493	84.3	11.617	1.03
1335	459	1.934	0.17	1754	329	2.795	0.29	1545	84.2	11.631	1.03
1357	475	1.86	0.16	1850	343	2.67	0.28	1598	84.2	11.631	1.03
1425	493	1.783	0.16	1947	357	2.556	0.26	1650	84.1	11.646	1.03
1494	511	1.712	0.15	2044	371	2.45	0.25	1703	84.3	11.617	1.03
1563	529	1.645	0.15	2140	386	2.346	0.24	1755	84	11.66	1.03
1632	547	1.583	0.14	2237	401	2.249	0.23	1807	84.1	11.646	1.03
1700	564	1.528	0.14	2334	416	2.159	0.22	1860	84.3	11.617	1.03
1769	581	1.476	0.13	2431	430	2.081	0.22	1912	84.3	11.617	1.03

1838	597	1.43	0.13	2527	450	1.977	0.2	1964	84	11.66	1.03
1907	613	1.386	0.12	2624	460	1.929	0.2	2017	84	11.66	1.03
1975	630	1.342	0.12	2721	480	1.838	0.19	2069	84.1	11.646	1.03
2044	646	1.303	0.12	2817	490	1.796	0.19	2121	83.8	11.688	1.03
2113	661	1.268	0.11	2914	510	1.716	0.18	2174	84.1	11.646	1.03
2182	676	1.234	0.11	3011	530	1.642	0.17	2226	84.1	11.646	1.03
2250	691	1.202	0.11	3107	540	1.607	0.17	2279	84	11.66	1.03
2319	706	1.171	0.1	3204	560	1.541	0.16	2331	84.2	11.631	1.03
2388	719	1.146	0.1	3301	580	1.479	0.15	2383	84.2	11.631	1.03
2456	732	1.121	0.1	3398	590	1.45	0.15	2436	84.1	11.646	1.03
2525	745	1.097	0.1	3494	610	1.394	0.14	2488	83.7	11.702	1.03
2594	757	1.076	0.1	3591	630	1.342	0.14	2540	83.6	11.717	1.04
2663	770	1.054	0.09	3688	650	1.293	0.13	2593	84	11.66	1.03
2731	780	1.037	0.09	3784	660	1.27	0.13	2645	83.2	11.774	1.04
2800	790	1.021	0.09	3833	670	1.248	0.13	2698	83.7	11.702	1.03
2869	800	1.005	0.09	3929	690	1.204	0.12	2750	83.7	11.702	1.03
2938	810	0.99	0.09	4026	710	1.163	0.12	2802	83.7	11.702	1.03
3006	820	0.975	0.09	4123	730	1.125	0.12	2855	83.5	11.731	1.04
3075	830	0.96	0.08	4220	740	1.106	0.11	2907	83.8	11.688	1.03
3144	840	0.945	0.08	4316	760	1.071	0.11	2959	83.7	11.702	1.03
3213	840	0.945	0.08	4413	780	1.037	0.11	3012	83.6	11.717	1.04
3281	850	0.931	0.08	4510	800	1.005	0.1	3064	83.7	11.702	1.03
3350	860	0.918	0.08	4606	820	0.975	0.1	3068	83.5	11.731	1.04
3419	860	0.918	0.08	4703	840	0.945	0.1	3121	83.3	11.76	1.04
3487	870	0.904	0.08	4800	860	0.918	0.1	3173	83.8	11.688	1.03
3556	880	0.891	0.08	4896	870	0.904	0.09	3225	83.5	11.731	1.04
3625	880	0.891	0.08	4993	900	0.866	0.09	3278	83.5	11.731	1.04

VI.1.5 Search for Adduct Formation between $[\text{Gd}(\text{DTTA-Me})(\text{H}_2\text{O})_2]^-$ and L-lactate

Table VI.1-5. Relaxivity r_1^m (T = 298 K; B = 0.235 T, 10 MHz; pH 7.0) versus L-lactate equivalents for 1 mM solutions of $[\text{Gd}(\text{DTTA-Me})(\text{H}_2\text{O})_2]^-$, and $[\text{Gd}(\text{DO3A})(\text{H}_2\text{O})_2]$, $[\text{Gd}(\text{MBzDO3AM})(\text{H}_2\text{O})_2]^{3-}$.

L-lactate equivalent	$[\text{Gd}(\text{DO3A})(\text{H}_2\text{O})_2]$	$[\text{Gd}(\text{DTTA-Me})(\text{H}_2\text{O})_2]^-$	$[\text{Gd}(\text{MBzDO3AM})(\text{H}_2\text{O})_2]^{3-}$
	r_1^m $\text{s}^{-1} \text{mM}^{-1}$	r_1^m $\text{s}^{-1} \text{mM}^{-1}$	r_1^m $\text{s}^{-1} \text{mM}^{-1}$
0.00	7	7.11	9.38
0.24	-	7.02	-
0.97	-	7.01	5.8
1.49	-	7.04	-
1.95	-	6.97	4.6
5.00	5.7	-	4.28
7.57	-	6.71	-
10.00	5	-	4.25
12.20	-	6.56	-
20.00	4.4	-	4.2
20.07	-	6.13	-
30.33	-	5.60	-
40.00	3.9	-	4.12
40.08	-	5.47	-
50.01	-	5.15	-

VI.2 APPENDIX TO CHAPTER III: EXPERIMENTAL DATA

This chapter will be in french .

La mise en place de la synthèse du composé $\{\text{Ru}[\text{Ln}_2\text{bpy}-\text{DTTA}_2(\text{H}_2\text{O})_4]_3\}^{4-}$ a demandé différentes expériences préliminaires. Elles sont résumées ci-dessous en deux tableaux.

Le premier tableau (Table VI.1-1) indique les expériences effectuées sur le ligand dimethyl bipy.

Le deuxième tableau (Table VI.2-2) indique les expériences effectuées sur le ligand bipyDTTA₂H₈.

Table VI.2-1: Bilan des manipes effectuées sur le dimethylbipy.

TEST AVEC ET SANS SEL SUR DIMETHYLBIPY				
Métal	Ligand L	Conditions	Observations	Conclusions
Ru(DMSO) ₄ (Cl) ₂	dimethylbipy	2/3 H ₂ O-1/3DMF	- Après 3 min, légère coloration.	
		Une nuit à 75°C et 5h à 100°C	- Après une nuit, coloration orangée. - Après 4h à 100°C, coloration orangée.	
			- Présence de RuL ₃ et de RuL ₂ majoritairement, un sous produit non identifié. (spectre de masse)	
Ru(DMSO) ₄ (Cl) ₂	dimethylbipy	2/3 H ₂ O	- Après 3 min, légère coloration.	- Présence de 10 équ. NaCl ne semble pas importuner la complexation du Ru(DMSO) ₄ (Cl) ₂
		1/3DMF	- Après une nuit, coloration orangée.	
		Une nuit à 75°C	- Après 4h à 100°C, coloration orangée.	
		4 h à 100°C	- Présence de RuL ₃ et de RuL ₂ majoritairement, un sous produit non identifier (spectre de masse).	
	10 équ. NaCl			
- Ru ^{II} (TOS) ₂ (H ₂ O) ₆	dimethylbipy	2/3 H ₂ O	- Quasi instantanément, devient rouge sang.	- Le métal Ru ^{II} (TOS) ₂ (H ₂ O) ₆ a une cinétique d'échange

		1/3DMF	- Après 20 min, solution rouge-noir.	plus rapide que celle du $\text{Ru}(\text{DMSO})_4(\text{Cl})_2$.
		Une nuit à 75°C 4 h à 100°C	- Présence de RuL_3 et de RuL_2Cl majoritairement (spectre de masse).	
- $\text{Ru}^{\text{II}}(\text{TOS})_2(\text{H}_2\text{O})_6$	dimethylbipy	2/3 H_2O	- Quasi instantanément, devient rouge sang.	Les réactions avec $\text{Ru}^{\text{II}}(\text{TOS})_2(\text{H}_2\text{O})_6$ sont sensibles à la présence des 10 équ. de NaCl. Se limiter à utiliser NaOH ou KOH pour remonter le pH lors de la complexation des DTTA.
		1/3DMF	- Après 20 min, solution rouge très foncé.	
		Une nuit à 75°C 4 h à 100°C	- Présence de RuL_3 et de RuL_2 , et d'une demi-douzaine d'autre sous produits.(spectre de masse).	
		10 équ. NaCl		

Table VI.2-2: Bilan des manip effectuées pour établir la voie de synthèse du composé ruthenium(II) $\{Ru[Ln_2bpy\text{-}DTTA_2(H_2O)_4]_3\}^{4-}$.

Métal	Ligand L	Conditions	Observations	Remarques	Conclusions
$Fe(NH_4)_2(SO_4)$ $X 6 H_2O$	$Gd@BipyDTTA$ acide	H_2O	OK	<i>Publication Bruno Livramento [Chemistry-A European Journal (2006) vol. 12 (4) pp. 989-1003]</i>	
<i>Travail 2006</i>					
Métal	Ligand L	Conditions	Observations	Remarques	Conclusions
- $GdCl_3$	$Gd@BipyDTTA$ acide	MeOH/ H_2O	Pas de produit final.	Manip pas poussée a fond ?	
- $Ru(DMSO)_4(Cl)_2$				Effectué par Angélique Sour et Bruno Livramento.	
- $Ru(DMSO)_4(Cl)_2$	BipyDTTA ester	DMSO 100 °C NaOH/HCL NaBF ₄ et NaCF ₃ SO ₃	- Présence de RuL ₃ , RuL ₂ et autre sous produits (spectre de masse) - Suivi par RMN	- Ru catalyse la coupure CH ₂ -N entre la pyridine et l'azote central du BipyDTTA ester. - A cette température, Ru ^{II} se fait facilement réduire par résidu protique pour former du Ru ⁰ ou peut former des oligomers Ru-O-Ru.	Complexé avec le DTTA acide avec un Ln avant l'ajout de Ru ^{II} .
- $Ru^{II}(TOS)_2(H_2O)_6$	Dimethylbipy	H ₂ O - 50°C	Rouge foncé.	-Milieu de solvation adéquat.	-Refaire avec

		2:30 h sous argon	Présence de RuL_3 majoritairement.	- $Ru^{II}TOS_2(H_2O)_6$ réagit très rapidement avec les dimethylbipy.	Gd@BipyDTTA acide.
- $GdCl_3$ - $Ru^{II}(TOS)_2(H_2O)_6$	Gd@BipyDTTA acide	H_2O (50°C) - 6h sous argon	- Après 15 minutes à 50°C, le Rouge foncé apparaît.	- Problème à obtenir le spectre de masse (Na^+ , charges du composé,...). - Petit accident: excès de ruthénium. - Le metal $Ru^{II}(TOS)_2(H_2O)_6$ est nettement plus réactif que $Ru(DMSO)_4(Cl)_2$.	-Le Ru^{II} aqua est très prometteur. -Eviter le sodium pour faciliter la masse (résine d'échangeuse d'ion (Dowex50W), tampon $(Et)_3H_2CO_3$).
- $GdCl_3$ - $Ru^{II}(TOS)_2(H_2O)_6$	Gd@BipyDTTA acide	H_2O - sous argon une nuit à T ambiant + 2 h à 60°C $N(Et)_3$ HCl	- Après 5 min à T ambiant. Solution rose. - Après une nuit, légèrement plus rosé. -Après chauffage, rose plus intense.	- pH ajusté avec $N(Et)_3$ pour la complexation du bipy(DTTA) ₂ par Gd. -Triethylamine a coordonné le Ru^{II} ? - Problème de coordination dû aux Cl^- ? -Aucun signal en electrospray, ni en malditoff différentes matrices (DHB, SA, CHCA, HPA, THAP).	- Ne pas utiliser de $N(Et)_3$.
- $Gd(TOS)_3$	Gd@BipyDTTA acide	2/3 H_2O - 1/3DMF	- Après 10 min, sol. rouge claire.	- Après adjonction du métal à la solution de ligand, une opacité apparaît (référence trouvée	- Ne pas utiliser le $Gd(TOS)_3$ -

- Ru ^{II} (TOS) ₂ (H ₂ O) ₆	(70°C) NaOH+KOH 3h sous Argon	- Après 20 min, rouge foncé.	sur l'efficacité des Ln(TOS) à catalyser les réactions d'acetylations... - Les différents spectres de masse n'indiquent toujours rien... - Gd(TOS) ₃ obtenu en faisant réagir un excès d'oxyde de gadolinium GdO ₃ à de l'acide tosylique à 100°C pendant 1h30. Filtration de l'excès de GdO ₃ .	catalysateur de réaction d'acetylation.
---	-------------------------------------	------------------------------	---	---

Après avoir trouvé les conditions adéquates de synthèse du composé $\{\text{Ru}[\text{Ln}_2\text{bpy-DTTA}_2(\text{H}_2\text{O})_4]_3\}^{4+}$, une procédure a été établie et optimisée à l'aide du composé yttrium(III) pour la synthèse des composés lanthanides $\{\text{Ru}[\text{Gd}_2\text{bpy-DTTA}_2(\text{H}_2\text{O})_4]_3\}^{4+}$ et $\{\text{Ru}[\text{Eu}_2\text{bpy-DTTA}_2(\text{H}_2\text{O})_4]_3\}^{4+}$. Les deux sous-chapitres suivant (VI.2.1 et VI.2.2) sont la procédure théorique en prévision de la synthèse et pratique, lors de la synthèse.

VI.2.1 Suivi théorique par RMN de la formation de $\text{Ru}^{\text{II}}[\text{Y}_2\text{bipy}(\text{DTTA})_2]_3\cdot\text{Na}_4$

Solution YCl_3 : Solubiliser 780 mg $\text{YCl}_3\cdot 7\text{H}_2\text{O}$ ($\text{MM}_{\text{YCl}_3\cdot 7\text{H}_2\text{O}}=195.27 + 126.1 = 321.4\text{g/mol}$, $n_{\text{YCl}_3} = 2.42$ mmol) dans 2 g D_2O . Obtention d'une solution YCl_3 de concentration $870 \mu\text{mol}_{\text{Y}^{3+}}/\text{g}_{\text{solYCl}_3}$.

Peser 100 mg de solution YCl_3 ($870 \mu\text{mol}_{\text{Y}^{3+}}/\text{g}_{\text{solYCl}_3}$, $n_{\text{YCl}_3} = 87.05 \mu\text{mol}$) et titrer avec ~ 17.4 ml EDTA 5 mM ($n_{\text{EDTA}} = 87.05 \mu\text{mol}$)

Solution bipyDTTA₂: solubiliser 200 mg bipyDTTA₂ acide ($\text{MM}_{\text{bipyDTTA}_2\text{acide}} = 850.83$ g/mol, $n_{\text{bipyDTTA}_2\text{acide}} = 235.1 \mu\text{mol}$) dans 373.1 mg D_2O . Obtention d'une solution de bipyDTTA₂ de concentration $410 \mu\text{mol}_{\text{bipyDTTA}_2\text{acid}}/\text{g}_{\text{solbipy}}$.

Peser 20 mg de solution bipyDTTA₂ acide ($410 \mu\text{mol}_{\text{bipyDTTA}_2\text{acid}}/\text{g}_{\text{solbipy}}$, $n_{\text{bipyDTTA}_2\text{acide}} = 8.2 \mu\text{mol}$) et 25 mg de solution YCl_3 ($870.5 \mu\text{mol}_{\text{Y}^{3+}}/\text{g}_{\text{solYCl}_3}$, $n_{\text{YCl}_3} = 21.76 \mu\text{mol}$) et titrer avec 1.073 ml EDTA 5 mM ($n_{\text{EDTA}} = 5.36 \mu\text{mol}$).

Solution bipyDTTA₂Y₂: Additionner 452.2 – 461.2 mg de la solution YCl_3 ($870.5 \mu\text{mol}_{\text{Y}^{3+}}/\text{g}_{\text{solYCl}_3}$, $n_{\text{YCl}_3} = 393.6\text{--}401.5 \mu\text{mol}$, 0-2% excès) à 480 mg de solution bipyDTTA₂ acide ($410 \mu\text{mol}_{\text{bipyDTTA}_2\text{acid}}/\text{g}_{\text{solbipy}}$, $n_{\text{bipyDTTA}_2\text{acide}} = 196.8 \mu\text{mol}$). Peser le ballon. Remonter le pH ($n_{\text{H}^+} = 2.165$ mmol, ~ 11 équivalents bipyDTTA₂) avec NaOD 13.6M ($\sim 158 \mu\text{l}$, $n_{\text{NaOD}} = 2.14$ mmol) et NaOD 0.5M ($\sim 50 \mu\text{l}$, $25 \mu\text{mol}$) jusqu'à pH 5.5. Peser le ballon. Obtention d'une solution de bipyDTTA₂Y₂ de masse = ~ 1140.2 mg et de concentrations $172.6 \mu\text{mol}_{\text{bipyDTTA}_2\text{acid}}/\text{g}_{\text{sol}}$ et $345.2 \mu\text{mol}_{\text{Y}^{3+}}/\text{g}_{\text{sol}}$.

Suivi RMN de la réaction : $\text{Ru}^{\text{II}}(\text{TOS})_2(\text{H}_2\text{O})_6 + 3 [\text{bipyDTTA}_2\text{Y}_2]^- \rightarrow [\text{Ru}^{\text{II}}(\text{bipyDTTA}_2\text{Y}_2)_3]^{4-}$

Solution $\text{Ru}^{\text{II}}(\text{TOS})_2(\text{H}_2\text{O})_6$: Peser 27.6 mg $\text{Ru}^{\text{II}}(\text{TOS})_2(\text{H}_2\text{O})_6$ (MM= 551.56 g/mol, $n_{\text{RuII}} = 50.0 \mu\text{mol}$), fermé par un septum. Remplacer air par Argon. Injecter 300 mg D_2O dégazés – obtention d’une solution de 327.6 mg de concentration $152.6 \mu\text{mol}_{\text{RuII}}/\text{g}_{\text{solRuII}}$.

Solution $[\text{Ru}(\text{bipyDTTA}_2\text{Y}_2)_3]^{4-}$: Mélanger 300 mg de solution de $\text{bipyDTTA}_2\text{Y}_2$, ($172.6 \mu\text{mol}_{\text{bipyDTTA2acid}}/\text{g}_{\text{sol}}$, $n_{\text{bipyDTTA2Y2}} = 51.78 \mu\text{mol}$) sous argon avec 111.99 – 113.1 mg de la solution de $\text{Ru}(\text{tos})_2(\text{H}_2\text{O})_6$ ($152.6 \mu\text{mol}_{\text{RuII}}/\text{g}_{\text{solRuII}}$, $n_{\text{RuII}} = 17.09 - 17.26 \mu\text{mol}$, 1 – 0% déficit molaire de Ru^{II} par rapport à $\text{bipyDTTA}_2\text{Y}_2$).

Tube RMN: Faire le vide à -20°C et sceller le tube RMN 3 contenant ~ 420 mg de milieu réactionnel ($40.7 \mu\text{mol}_{\text{RuII}}/\text{g}_{\text{sol}}$, $123.3 \mu\text{mol}_{\text{bipyDTTA2acid}}/\text{g}_{\text{sol}}$). Suivi RMN ^1H - 400 MHz à 298.15 K.

VI.2.2 Suivi pratique par RMN de la formation de $\text{Ru}^{\text{II}}[\text{Y}_2\text{bipy}(\text{DTTA})_2]_3 \cdot \text{Na}_4$

ETAPE 1 : Solution de YCl_3 :

Snapcup (10 ML, monocol) : g YCl_3 (MM $_{\text{YCl}_3}$ =195.27 g/mol, $n_{\text{YCl}_3} =$ mmol) sont solubiliser dans g D_2O . Obtention d’une solution YCl_3 de concentration \sim $\mu\text{molY}^{3+}/\text{g}_{\text{solYCl}_3}$.

Titration :- **1** - Titré mg de solution YCl_3 avec ml EDTA 5 mM ($n_{\text{EDTA}} =$ μmol). Concentration obtenue : $\mu\text{molY}^{3+}/\text{g}_{\text{solYCl}_3}$. - **2** - Titré mg de solution YCl_3 avec ml EDTA 5 mM ($n_{\text{EDTA}} =$ μmol). Concentration obtenue : $\mu\text{molY}^{3+}/\text{g}_{\text{solYCl}_3}$. Concentration solution YCl_3 : $\mu\text{molY}^{3+}/\text{g}_{\text{solYCl}_3}$

ETAPE 2 : Solution de bipyDTTA_2

Ballon 1 (10 ML, monocol, masse à sec sans bouchon = G) : On mélange mg de bipyDTTA_2 (poudre rose) (MM $_{\text{bipyDTTA2acid}} = 850.83$ g/mol ; $n_{\text{bipyDTTA2acid}}$

= ~..... μmole , $n_{\text{DTTA}} = \sim\text{..... } \mu\text{mole}$) à g de D_2O \rightarrow conc.
 $\text{DTTA} \approx \text{..... } \mu\text{mol}_{\text{DTTA}}/\text{g}_{\text{solbipy}}$

Titration : - **1** - On prélève mg de solution bipyDTTA₂ acide (conc. DTTA :
 $\mu\text{mol}_{\text{DTTA}}/\text{g}_{\text{solbipy}}$, $n_{\text{DTTA}} = \sim\text{..... } \mu\text{mole}$) et on ajoute 1.2 fois de
 solution d'YCl₃ (..... $\mu\text{molY}^{3+}/\text{g}_{\text{solYCl}_3}$, $n_{\text{YCl}_3} = \text{..... } \mu\text{mol}$), donc
 mg de solution d'YCl₃. On titre avec ml EDTA 5 mM ($n_{\text{EDTA}} =$
 μmol). Obtention d'une sol. bipyDTTA acide de
 $\mu\text{mol}_{\text{bipyDTTA}_2\text{acid}}/\text{g}_{\text{solbipy}}$. - **2** - On prélève mg de solution bipyDTTA₂ acide
 (conc. DTTA : $\mu\text{mol}_{\text{DTTA}}/\text{g}_{\text{solbipy}}$, $n_{\text{DTTA}} = \sim\text{..... } \mu\text{mole}$) et on ajoute 1.2
 fois de solution d'YCl₃ (..... $\mu\text{molY}^{3+}/\text{g}_{\text{solYCl}_3}$, $n_{\text{YCl}_3} = \text{..... } \mu\text{mol}$), donc
 mg de solution d'YCl₃. On titre avec ml EDTA 5 mM ($n_{\text{EDTA}} =$
 μmol). Obtention d'une sol. bipyDTTA acide de
 $\mu\text{mol}_{\text{bipyDTTA}_2\text{acid}}/\text{g}_{\text{solbipy}}$. - **3** - On prélève mg de solution bipyDTTA₂ acide (conc.
 DTTA : $\mu\text{mol}_{\text{DTTA}}/\text{g}_{\text{solbipy}}$, $n_{\text{DTTA}} = \sim\text{..... } \mu\text{mole}$) et on ajoute 1.2 fois de
 solution d'YCl₃ (..... $\mu\text{molY}^{3+}/\text{g}_{\text{solYCl}_3}$, $n_{\text{YCl}_3} = \text{..... } \mu\text{mol}$), donc
 mg de solution d'YCl₃. On titre avec ml EDTA 5 mM ($n_{\text{EDTA}} =$
 μmol). Concentration solution DTTA : $\mu\text{mol}_{\text{DTTA}}/\text{g}_{\text{solbipy}}$. Masse
 actuel du ballon 1 moins masse du ballon sec : g de solution. Nombre de mole
 de DTTA contenu dans le ballon : $\mu\text{mol DTTA}$

ETAPE 3 : Solution de bipyDTTA₂Y₂

Ballon 1 (10 ML, monocol) : Ajouter au g de solution de bipy contenu dans le
 ballon 1 ($n_{\text{DTTA}} = \text{..... } \mu\text{mol}$) 1-2% d'excès d'Yttrium ($n_{\text{YCl}_3} = \text{..... } \mu\text{mol}$,
 $\mu\text{molY}^{3+}/\text{g}_{\text{solYCl}_3}$) \approx g de solution deutérée YCl₃. Remonter le pH
 ($n_{\text{H}^+} = \text{..... } \text{mmol}$, ~ 6 équivalents DTTA) avec **NaOD** 13.6M ($n_{\text{NaOD}} = \text{..... } \text{mmol}$,
 $\sim \text{..... } \mu\text{l}$) et **NaOD** 0.5M (..... μmol , $\sim \text{..... } \mu\text{l}$) jusqu'à pH
 5.5. Masse actuel du ballon moins masse du ballon sec : g de solution. Nombre
 de mole de DTTA contenu dans le ballon : $\mu\text{mol DTTA}$. Nombre de mole de

bipyDTTA₂ contenu dans le ballon : μmole bipyDTTA₂. Concentration solution bipyDTTA₂ : $\mu\text{mol}_{\text{bipyDTTA2acid}}/\text{g}_{\text{solbipy}}$

Tube RMN (PP, 5MM) : Injecter 400 μl de la solution de bipyDTTA₂Y₂. Fermeture du tube avec capuchon plastique. Spectre RMN ¹H - 400 MHz à 298.15 K – nom du fichier : Masse actuel du ballon 1 moins masse du ballon sec : g de solution. Nombre de mole de bipyDTTA₂ contenu dans le ballon : μmole bipyDTTA₂.

ETAPE 4 : Spectre ¹H du Ru(TOS)₂(H₂O)₆:

BALLON 2 (5 ML, monocol) : Dégazer 1 ml D₂O

TUBE RMN 2 (PP, 5MM) : Solubiliser dans un tube RMN 5mm ~10 mg Ru^{II}(TOS)₂(H₂O)₆ (MM= 551.56 g/mol, $n_{\text{RuII}} = 9.1 \mu\text{mol}$) dans 400 μl D₂O dégazé. Concentration en Ru^{II}= ~22.7 mM. Faire le vide et sceller le tube RMN 2. Spectre RMN ¹H - 400 MHz à 298.15 K – nom du fichier :

ETAPE 5 : Synthèse du Ru^{II}[(bipyDTTA₂Y₂)₃]⁴⁺ :

Dégazé 10 ml D₂O

BALLON 1: Dégazé la solution de bipyDTTA₂Y₂ (nombre de mole de **bipyDTTA₂Y₂** : μmole).

BALLON 3 (20 ML, monocol, masse à sec + septum = G) : On pèse du Ru^{II} pour avoir 1% déficit molaire de 1/3 bipyDTTA₂ ($n_{\text{RuII}} = \dots \mu\text{mol}$, MM= 551.56 g/mol) = mg Ru^{II}(TOS)₂(H₂O)₆, dans un ballon fermé par un septum. Remplacé air par Argon. On injecte ~ 2 g D₂O dégazés sur le Ru^{II}. On transfère par canule toute la solution de bipyDTTA₂Y₂. Masse actuel du ballon moins masse du ballon sec : g de solution. Nombre de mole de DTTA contenu dans le ballon : μmol DTTA. Nombre de mole de bipyDTTA₂ contenu dans le ballon : μmole bipyDTTA₂. Concentration solution bipyDTTA₂ : $\mu\text{mol}_{\text{bipyDTTA2acid}}/\text{g}_{\text{solbipy}}$

TUBE RMN (PP, 5MM) : On transfère par canule sous Argon ~ 500 mg de la solution de bipyDTTA₂Y₂Ru^{II} dans le tube RMN contenu dans un schlenk mis sous argon et on scelle le

tube RMN. Spectre RMN ^1H - 400 MHz à 298.15 K en chauffant périodiquement par bain marie à 100°C.

BALLON 3 (5 ML, monocol, G) : On met le reste de la solution aussi sous 100°C toujours sous pression d'argon. Masse actuel du ballon 3 moins masse du ballon sec +septum : g de solution. Nombre de mole de **bipyDTTA₂** contenu dans le ballon : μmole **bipyDTTA₂**.

ETAPE 6 : Synthèse du $\text{Ru}^{\text{II}}[(\text{bipyDTTA}_2\text{Y}_2)]_3^{4-}$:

BALLON 4 (10 ML, monocol) : Faire une solution contenant 2 équivalents $\text{bipyDTTA}_2\text{Y}_2$ (..... μmole bipyDTTA_2) de triéthylamine (..... μmole triéthylamine, $\text{MM}=101.19$ g/mol, mg triéthylamine) et 2 ml de D₂O. Dégazé la la solution.

BALLON 3 (20 ML, monocol, masse à sec + septum = G) : Après ~2 heures de réaction, ajouter par canule la solution du ballon 4 (2 équivalents $\text{bipyDTTA}_2\text{Y}_2$ de triéthylamine dégazée) à la solution du ballon 3.

TUBE RMN (PP, 5MM) : On transfère par canule sous Argon ~ 500 mg de la solution de $\text{bipyDTTA}_2\text{Y}_2\text{Ru}^{\text{II}}$ dans le tube RMN contenu dans un schlenk mis sous argon et on scelle le tube RMN. Spectre RMN ^1H - 400 MHz à 298.15 K en chauffant périodiquement par bain marie à 100°C.

VI.2.3 $\{\text{Ru}[\text{Gd}_2\text{bpy}-\text{DTTA}_2(\text{H}_2\text{O})_4]_3\}^{4-}$ and $\{\text{Fe}[\text{Gd}_2\text{bpy}-\text{DTTA}_2(\text{H}_2\text{O})_4]_3\}^{4-}$ relaxivities (NMRDs)

Table VI.2-3: Variable temperature proton relaxivity ($r_1/\text{mM}^{-1}\text{s}^{-1}$) of $\{\text{Ru}[\text{Gd}_2\text{bpy}-\text{DTTA}_2(\text{H}_2\text{O})_4]_3\}^{4-}$ ($c_{\text{Gd(III)}}: 8.31 \text{ mM}$). Results for $\{\text{Fe}[\text{Gd}_2\text{bpy}-\text{DTTA}_2(\text{H}_2\text{O})_4]_3\}^{4-}$ come from Joao Bruno Figueiredo Livramento thesis.

$\nu (^1\text{H}) / \text{MHz}$	Proton relaxivities $r_1 / \text{mM}^{-1}\text{s}^{-1}$			
	$\{\text{Ru}[\text{Gd}_2\text{bpy}-\text{DTTA}_2(\text{H}_2\text{O})_4]_3\}^{4-}$		$\{\text{Fe}[\text{Gd}_2\text{bpy}-\text{DTTA}_2(\text{H}_2\text{O})_4]_3\}^{4-}$	
	25°C	37°C	25°C	37°C
0.01	31.15	26.70	29.53	23.43
0.01	31.10	26.50	29.57	23.48
0.02	31.03	26.39	29.59	23.50
0.03	31.16	26.52	29.62	23.49
0.04	31.14	26.59	29.60	23.41
0.06	31.11	26.50	29.61	23.39
0.09	31.11	26.69	29.70	23.45
0.13	31.19	26.70	29.60	23.35
0.18	31.13	26.61	29.62	23.32
0.26	31.08	26.48	29.45	23.31
0.38	30.95	26.26	29.28	23.10
0.55	30.70	26.17	28.80	22.93
0.78	29.99	25.77	28.16	22.39
1.13	29.26	25.09	27.19	21.77
1.62	28.31	24.05	26.02	20.87
2.34	26.76	22.49	24.56	19.77
3.36	25.10	20.78	23.07	18.56
4.83	23.83	19.42	22.16	17.35
6.95	23.50	19.08	21.96	16.64
8.0	23.91		22.38	16.86
10.0	25.84	20.01	23.35	17.34
12	27.66	21.02	24.51	17.89
14	29.50	21.95	25.04	18.29
16	31.12	22.68	26.04	19.13
18	32.20	23.41	27.03	20.17
20	33.11	24.22	33.01	26.01
30	34.90	28.77	33.62	26.49
40	37.44	30.34	32.02	26.00
60	34.64	28.88	33.16	26.83
100	29.76	26.32	27.09	23.80
200	16.17	16.40	16.37	15.85
400	7.59	7.88	9.32	8.53
800	4.25	4.05	5.96	5.82

VI.3 APPENDIX TO CHAPTER IV

VI.3.1 Gd-DtNP(1), Gd-DtNP(2) and Gd-DtNP(3) relaxivities (NMRD)

Table VI.3-1: Variable temperature proton relaxivity ($r_1/\text{mM}^{-1}\text{s}^{-1}$) of system Gd-DtNP(1) ($c_{\text{Gd(III)}}: 0.378 \text{ mM}$), Gd-DTNP(2) ($c_{\text{Gd(III)}}: 0.015 \text{ mM}$) and Gd-DtNP(3) ($c_{\text{Gd(III)}}: 0.201 \text{ mM}$).

$\nu (^1\text{H}) / \text{MHz}$	Proton relaxivities $r_1 / \text{mM}^{-1}\text{s}^{-1}$			
	Gd-DTNP(1)		Gd-DTNP(2)	Gd-DTNP(3)
	25°C	37°C	25°C	25°C
0.01	45.81	44.28	-	43.73
0.01	45.76	44.31	-	43.55
0.02	45.56	44.16	-	43.70
0.03	45.77	44.11	-	43.69
0.04	45.74	44.19	-	43.62
0.06	45.80	44.25	-	43.68
0.09	45.49	44.16	-	43.57
0.13	45.56	43.85	-	43.59
0.18	45.36	43.87	-	43.29
0.26	45.06	43.56	-	43.16
0.38	44.68	43.00	-	42.11
0.55	43.58	41.98	--	41.32
0.78	42.20	40.42	-	40.19
1.13	39.77	38.85	-	38.56
1.62	38.35	36.64	-	36.81
2.34	36.01	34.67	-	34.90
3.36	34.16	32.76	-	33.30
4.83	32.99	31.00	-	32.81
6.95	35.27	31.99	-	34.93
10.0	41.13	36.38	-	40.54
12	44.22	-	-	44.79
14	48.90	-	-	47.78
18	-	-	-	53.17
20	54.61	-	48.94	55.94
30	61.13	54.38	54.53	58.51
40	59.16	53.35	52.15	54.76
60	50.30	48.20	40.51	41.04
100	32.75	-	-	-
200	14.11	-	-	-
	6.65	-	-	-

Loïck Moriggi

Rue du Midi 16
1003 Lausanne
+41 78 897 28 58
loick.moriggi@gmail.com

16 May 1979
Single
Swiss / Italian

Formation

- **PhD in analytical and inorganic chemistry** (18.12.2008) at the Ecole Polytechnique Fédérale de Lausanne (EPFL) 2005 - 2008
- **Master in chemistry and chemical engineering** at EPFL 1999 - 2004
- **Maturité Fédérale type C** 1996 - 1999

Professional experiences

- **PhD** in the field of magnetic resonance imaging (MRI) contrast agents (group directors Merbach/Helm) (Title: “Highly efficient MRI contrast agents: from monomers to nanoparticles “): 2005 - 2008
 - Collaboration with Novartis on the development of dendrimeric structures for high magnetic field MRI contrast agents.
 - Development of a project on heavy metal complexes based on inductively coupled plasma–mass spectrometry (ICP-MS) and gold nanoparticles.
 - Development of an analytical method using nuclear magnetic resonance (NMR) to determine in a direct way the conditional stability constant of gadolinium(III) complex.
 - Development of a synthesis route for a ruthenium(II) complex for high magnetic field MRI contrast agents.
- **Master work at Purdue University – IN – U.S.A.** in the field of laser spectroscopy and computational chemistry. (Title: “Spectroscopic and computational studies of flexible biomolecules “) 2003 - 2004
- Coordination of marketing events under mandate of General Motors c/o Nyou AG (Biel) 2003 - 2007
- Co-founder of the family business of olive oil and food importation Moriggi & Frères Olive Oil Import 1996 - 2006

Skills

- Techniques NMR – potentiometry – ICP-MS – DLS
- Languages
 - French: mother tongue
 - English: fluent (written and spoken)
 - Italian: intermediate knowledge (spoken)
 - German: basic knowledge (written and spoken)
- IT Sciences (CAChE– Chemdraw – Matlab – Gaussian – Hyperquad)
Standard office software – Graphism (Illustrator, Photoshop)
- Teaching
 - Assistant in charge of bachelor and master projects
 - Assistant in advanced analytical and inorganic chemistry

Publications

1. J.R. Clarkson, B.C. Dian, L. Moriggi, A. Defusco, V. McCarthy, K.D. Jordan, and T.S. Zwier, *J. Chem. Phys.*, 2005. **122**: p. 214311.
2. Z. Jaszberenyi, L. Moriggi, P. Schmidt, C. Weidensteiner, R. Kneuer, A.E. Merbach, L. Helm, and E. Toth, *J. Biol. Inorg. Chem.*, 2007. **12**: p. 406-420.
3. M. Benmelouka, A. Borel, L. Moriggi, L. Helm, and A.E. Merbach, *J. Phys. Chem. A*, 2007. **111**: p. 832-840.
4. L. Moriggi, C. Cannizzo, C. Prestinari, F. Beyrière, and L. Helm, *Inorg. Chem.*, 2008. **47**(18): p. 8357-66.
5. A. Borel, J.F. Bean, R.B. Clarkson, L. Helm, L. Moriggi, A.D. Sherry, and M. Woods, *Chem. Eur. J.*, 2008. **14**: p. 2658-2667.
6. L. Moriggi, A. Aebischer, C. Cannizzo, A. Sour, A. Borel, J.C.G. Bünzli, and L. Helm, *Dalton Trans.*, 2009. (accepted)
7. L. Moriggi, C. Mayer, C. Cannizzo, and L. Helm, *Angew. Chem.*, 2009. (submitted)

References

Prof. Lothar Helm, EPFL-ISIC-LCIB (lothar.helm@epfl.ch, +41 (21) 693 98 76)
Prof. Hon. André Merbach, EPFL-ISIC-LCIB (andre.merbach@epfl.ch, +41 (21) 693 98 71)
Prof. Timothy Zwier, Purdue University, Department of Chemistry (zwier@purdue.edu, +1 (765) 494-5278)

PUBLICATIONS

-1- Clarkson, J. R., Dian, B. C., Moriggi, L., Defusco, A., McCarthy, V., Jordan, K. D. and Zwier, T. S. (2005). Direct measurement of the energy thresholds to conformational isomerization in Tryptamine: Experiment and theory. *Journal of Chemical Physics*. **122**: 214311.

-2- Jaszberenyi, Z., Moriggi, L., Schmidt, P., Weidensteiner, C., Kneuer, R., Merbach, A. E., Helm, L. and Toth, E. (2007). "Physicochemical and MRI characterization of Gd³⁺-loaded polyamidoamine and hyperbranched dendrimers." *Journal of Biological Inorganic Chemistry* **12**: 406-420.

-3- Benmelouka, M., Borel, A., Moriggi, L., Helm, L. and Merbach, A. E. (2007). Design of Gd(III)-based magnetic resonance imaging contrast agents: Static and transient zero-field splitting contributions to the electronic relaxation and their impact on relaxivity. *Journal of Physical Chemistry B*. **111**: 832-840.

-4- Borel, A., Bean, J. F., Clarkson, R. B., Helm, L., Moriggi, L., Sherry, A. D. and Woods, M. (2008). "Towards the rational design of MRI contrast agents: Electron spin relaxation is largely unaffected by the coordination geometry of Gadolinium(III)-DOTA-Type complexes." *Chemistry-A European Journal* **14**: 2658-2667.

-5- Moriggi, L., Cannizzo, C., Prestinari, C., Beyrière, F. and Helm, L. (2008). "Physicochemical Properties of the High-Field MRI-Relevant [Gd(DTTA-Me)(H₂O)₂]⁺ Complex." *Inorganic Chemistry* **47**(18): 8357-66.

-6- Moriggi, L., Aebischer, A., Cannizzo, C., Sour, A., Borel, A., Bünzli, J. C. G. and Helm, L. (2009). "A ruthenium-based metallostar: synthesis, magnetic relaxivity and sensitized luminescence." *Journal of the Chemical Society-Dalton Transactions*. – Accepted

-7- Moriggi, L., Cannizzo, C., Ulianov, A., Mayer, C. and Helm, L. (2009). "DTTA thiol capped gold nanoparticles: characterization, magnetism and relaxivity." *Angewandte Chemie*.
- Submitted.

-8- Ananta, J. S., Moriggi, L., Juneja, V., Hartman, K. B., Helm, L. and Wilson, L. J. (2009). "Dextran coated gadonanotubes: water-soluble biocompatible High-performance MRI contrast agents." – Submitted

PRESENTATIONS

Conferences

Loïck Moriggi, Sabrina Laus, Eva Tóth, Balaji Sitharaman, Keith Hartman, Lon Wilson, **Lothar Helm**. TOPIM 2008, Les Houches, France, Feb. 4-8, 2008. "Fullerenes and Carbon Nanotubes Loaded with Gd as High Relaxivity MRI Agents"

Loïck Moriggi, Caroline Cannizzo, Cora Prestinari, Florent Beyrière, Lothar Helm. COST Working Group Meeting, Orléans, France, February 29 – March 1st 2008. "A Potentiometric and NMR Relaxometric Study of [Gd(DTTA-Me)(H₂O)₂]- as a Model for the Gd-DTTA Chelating Unit"

Posters

Loïck Moriggi, Caroline Cannizzo, Angélique Sour, Lothar Helm. COST D38 Action meeting, Eindhoven (Netherlands), May 4 – 6, 2007. "A Ruthenium-based Metallostar: synthesis, characterization and relaxivity"

Loïck Moriggi, Caroline Cannizzo, Florent Beyrière, Cora Prestinari, Lothar Helm. COST D38 Action meeting, Eindhoven (Netherlands), May 4 – 6, 2007. "Physico-chemical study of the ligand DTTA-Me and its Gd complex."

Caroline Cannizzo, Emmanuel Allard, Loïck Moriggi, Angélique Sour, Chantal Larpent, Lothar Helm. COST D38 Action meeting, Eindhoven (Netherlands), May 4 – 6, 2007. "Polymeric nanoparticles as T₁ Contrast Agents."

Caroline Cannizzo, Emmanuel Allard, Loïck Moriggi, Angélique Sour, André E. Merbach, Chantal Larpent, Lothar Helm. 2nd International conference of the European Society of Molecular Imaging, Naples (Italy), June 14-15 2007. "Grafting of a gadolinium complex on polymeric nanoparticles: a macromoleculuar T₁ contrast agent for MRI."

Caroline Cannizzo, Emmanuel Allard, Loïck Moriggi, Angélique Sour, André E. Merbach, Chantal Larpent, Lothar Helm. Swiss Chemical Society Fall Meeting 2007, Lausanne, Sept.

12, 2007. "Magnetic Resonance Imaging contrast agent: grafting of a gadolinium complex on polymer nanoparticles."

Loïck Moriggi, Caroline Cannizzo, Florent Beyrière, Cora Prestinari, André E. Merbach, Chantal Larpent, Lothar Helm. Swiss Chemical Society Fall Meeting 2007, Lausanne, Sept. 12, 2007. "Physico-chemical and relaxometric studies of the ligand DTTA-Me and its Gd^{3+} complex."

Loïck Moriggi, Caroline Cannizzo, Angélique Sour, André E. Merbach, Lothar Helm. Swiss Chemical Society Fall Meeting 2007, Lausanne, Sept. 12, 2007. "A Ruthenium-based Metallostar: a multi imaging system?"

Hugues Jaccard, Caroline Cannizzo, Cédric R. Mayer, Loïck Moriggi, Lothar Helm. COST D38 action "European Conference on Metal-Based Systems for Molecular Imaging Applications", Lisbon (Portugal), April 27-29 2008. "Surprisingly high relaxivities of the $[Ph_4\{Gd(DTTA)(H_2O)_2\}_3]^{3-}$ complex"

Loïck Moriggi, A. Aebischer, C. Cannizzo, J.-C. Bünzli, L. Helm. COST D38 action "European Conference on Metal-Based Systems for Molecular Imaging Applications", Lisbon (Portugal), April 27-29 2008. "Characterization, Relaxivity and Luminescence of Lanthanide/Ruthenium-based Metallostar"

Loïck Moriggi, A. Aebischer, C. Cannizzo, A. Sour, J.-C. Bünzli, L. Helm. Swiss Chemical Society Fall Meeting 2008, Zürich, Sept. 11, 2008. "Lanthanide/ruthenium-based metallostar: characterization, relaxivity and luminescence"

Hugues Jaccard, Caroline Cannizzo, Cédric R. Mayer, Loïck Moriggi, Lothar Helm. Swiss Chemical Society Fall Meeting 2008, Zürich, Sept. 11, 2008. "Remarkably high T_1 relaxivities of the complex $[Ph_4\{Gd(DTTA)(H_2O)_2\}_3]^{3-}$ "